Design and Atomic Scale Characterization of Complex Oxide Interfaces

TECHNISCHE UNIVERSITÄT DARMSTADT

Dissertation

by Nicolas Bonmassar

Date of Birth: 26.02.1996

Submitted to the

Department of Materials- and Geosciences
at the
Technical University of Darmstadt

in Fulfillment of the Requirements for the Degree of

Doctor rerum naturalium (Dr. rer. nat.)

Referee:

Prof. Dr. Christian Kübel

Co-referee:

Prof. Dr. Peter Antonie van Aken

Darmstadt 2024

This work was conducted at the

Max Planck Institute for Solid State Research

Contents

Affirmation

I, Nicolas Bonmassar, affirm that I conducted the independent research presented in the thesis titled "Design and Atomic Scale Characterization of Complex Oxide Interfaces" at the Max Planck Institute for Solid State Research. This work satisfies the requirements for the Doctor of Natural Science (Dr. rer. nat.) degree in the Department of Materials- and Geosciences at the Technical University of Darmstadt. I declare that the work presented is, to the best of my knowledge and belief, original and does not include any material previously published or written by another person, except where appropriate reference and permission have been obtained.

_____   _____
Date, Place   Signature

Abstract

The framework of my thesis includes four main categories: i) An introduction about the physics, materials, and methods used in this work. ii) The characterization of interfacial physical properties resulting in the deduction of structure-property relationships at the atomic scale. iii) The control of interface sharpness at the atomic scale, which is crucial for the realization of complex oxide technologies in spintronics and electronics. iv) The development and design of new types of interfaces with completely new functionalities.

More specifically, the overarching objective of this thesis was to design certain types of interfaces and employ advanced scanning transmission electron microscopy characterization techniques on oxide superlattices.

In the first part, the focus lies on Sr-La intermixing-induced superconductivity and probing the evolution of the electronic states from an antiferromagnetic insulator to a superconductor and a metal at the atomic scale. The outcome of the first part includes a novel way to differentiate distinct quantum states, such as insulating materials, metallic-, and superconducting materials, at the subnanometer scale based on the combined detection and interpretation of hole doping, Sr-content, and oxygen vacancies.

In the following part, I aimed to enhance the interface sharpness by strategically utilizing materials that exhibit both structural and chemical coherence. The primary aim was to minimize the chemical potential gradient at the interface to achieve unprecedented control over oxide interfaces at the atomic level.

The third part of this thesis is about a novel interface paradigm, denoted as the step edge interface, which enables the simultaneous growth of thin films in two distinct directions, denoted as the **bi-directional growth** of thin films.

In the last part of my thesis, I address a key limitation of this innovative approach; while it offers an additional dimension of control, it necessitates careful consideration of the a-, b-, and c-axes of the substrate and the materials of choice. Particularly, while one of these crystallographic parameters may align suitably, the other parameters assume critical significance when growing thin films on offcut substrates, thereby enabling the formation of planar defects such as antiphase boundaries. Hence, while the newly developed bi-directional growth utilizing offcut substrates opens up an additional degree of freedom for the design of exotic quantum phenomena, I show what problems are there to overcome and how to solve these problems for the future integration of this novel technique into electronics and spintronics.

Zusammenfassung

Diese Doktorarbeit kann im Grunde in vier Hauptkategorien unterteilt werden: i) Eine Einleitung, die sowohl einen Überblick über die physikalischen und materialspezifischen Grundlagen als auch über die angewandte Methodik dieser Arbeit verschafft. ii) Die Charakterisierung der physikalischen Eigenschaften an Grenzflächen, die es ermöglicht Struktur-Eigenschafts- beziehungen herzuleiten. iii) Die Kontrolle über die atomare Schärfe von Grenzflächen, welche unabdingbar für die Realisierung von Komplexoxidtechnologien für Bereiche der Spintronik und der Elektronik sind. iiii) Das Design und die Entwicklung einer neuen Art von Grenzfläche, die komplett neue Eigenschaften der Materialien nach sich zieht.

Die zugrunde liegende Idee dieser Doktorarbeit war es, die Grenzflächen von Oxidüber-gitter mittels fortgeschrittener Rastertransmissionselektronenmikroskopie mit atomarer Genauigkeit zu analysieren.

Im ersten Teil dieser Arbeit liegt der Fokus auf der Vermischung von La und Sr Atomen, die zu Supraleitung an der Grenzfläche von zwei nicht supraleitenden Materialien führt. Weiterhin wurde die Entwicklung der elektronischen Struktur von einem antiferromag-netischen Isolator über einen Supraleiter bis hin zu einem Metall mit atomarer Auflösung untersucht. Das Ergebnis dieses Kapitels stellt eine neue Methode zur Unterscheidung von spezifischen Quantenzuständen wie isolatorische, metallische und supraleitende Materialien da. Für diese Unterscheidung ist es notwendig die Verteilung von Löchern, Sr-Atomen und Sauerstofffehlstellen zeitgleich im Subnanometerbereich zu detektieren.

Im zweiten Teil der Arbeit wird auf die Kontrolle der Schärfe von Grenzflächen eingegangen, indem zwei Materialien verwendet wurden, die sowohl strukturelle als auch chemische Kohärenz aufweisen. Das Hauptaugenmerk liegt hier auf der Reduzierung der Unterschiede im chemischen Potential, um eine atomare Kontrolle über Oxidgrenzflächen zu ereichen.

Der dritte Teil dieser Doktorarbeit handelt über die Entdeckung einer neuen Grenzfläche, die ich als Stufenkantengrenzfläche definiert habe und die es mir ermöglicht, Dünnfilme in zwei Richtungen gleichzeitig zu wachsen. Diese Art von Wachstum wurde als **bidirektionales Wachstum** von Dünnfilmen definiert.

Im letzten Teil dieser Arbeit verweise ich auf eine Limitierung dieses bidirektionalen Wachstums bezüglich der Defektbildung; denn die Stufenkanten ermöglichen zwar die Kontrolle einer zusätzlichen Dimension für das Wachstum von Dünnfilme, aber man muss auf die kristallographischen a-, b- und c-Achsen der verschiedenen Substrate und Materialien achten. Insbesondere werden beim Wachstum von Dünnfilmen auf ordinären Substraten nur die Achsen in eine Richtung berücksichtigt, währenddessen bei der Benutzung von off-cut Substraten darauf geachtet werden muss, dass a-, b- und c-Achsen zueinanderpassen. Sind die Gitterabstände zu unterschiedlich, kommt es zur Formierung von planaren Defekten wie Antiphasengrenzen. Daher wird in diesem Abschnitt darauf eingegangen, wie und wo diese Defekte auftauchen und wie man die Formierung von diesen Antiphasengrenzen verhindern kann.

Acknowledgements

First, I want to thank **Prof. Peter A. van Aken** sincerely for enabling me to have this outstanding experience at the Max Planck Institute for Solid State Research and for making this whole work possible in the first place. I also want to sincerely thank **Dr. Gennady Logvenov**, who allowed me to work in his laboratory on a daily basis and opened the wonderful world of complex oxide thin films for me. At this point, I would like to emphasize the help of my daily supervisor **Dr. Eren Suyolcu** and I would like to thank him specifically for the fruitful discussions that we had on numerous topics regarding publications and research in general. Of course, I would like to thank **Georg Christiani** for his enormous help during my Ph.D. including his answers to all of my questions regarding the MBE and PLD systems and the countless and still not ending teaching lessons. I want to thank **Gideok Kim** for his invaluable help during the first and last steps of my studies here at MPI.

I want to address my greatest gratitude to my friends **Thomas Schraivogel**, whom I have known since the first semester of studying chemistry in Innsbruck, **Jan W. Gärtner**, and **Maximilian Hödl**, who I met here in Stuttgart outside of the institute just before the start of the pandemic. You three made the pandemic bearable for me.

Many thanks go out to **Ute Salzberger** for providing me with more than 80 tripod samples (til now) and her assistance in overcoming diverse obstacles, as well as to **Kersten Hahn** and **Peter Kopold** for showing me the fundamental microscopy skills, and also to **Peter Specht** for maintaining the MBE system.

I want to thank **Lukas Debbeler**, the leader of the "Party Theorists", for the countless situations, where he proved that he is not only an excellent scientist but also a great friend with an outstanding and motivating attitude. **Maximilian Brucker** was not only a great scientific support for my Ph.D. but also a close friend of mine outside the institute.

I would like to thank **Anna Scheid** for the numerous after-work activities with the good Stuttgarter Hofbräu outside the canteen in the wooden circle. My great office mate **Xuejiao Zhang** made life a lot easier for me here at the institute, welcoming me to the office with a lot of delicious snacks. My other great office mate **Pablo Sosa** is not only a cheerful motivator but also a good friend of mine outside of the institute. **Vesna Srot's** impressive knowledge of the two microscopes I used during my Ph.D. was of utmost importance for my final results. She is a great scientist and an even greater friend, who supported me in numerous situations during my time here in Stuttgart. Thanks a lot to **Caroline Heer** for the administration and guidance through the countless obstacles installed by the German bureaucracy. I would like to thank **Julia Deuschle** for instructing me on specimen preparation with FIB and for the nice and motivating chats during the many coffee breaks after lunch. In addition, I would like to thank **Tobias Heil** for his contribution regarding data analysis and for providing me with his useful codes during my Ph.D., **Yu-Mi Wu** for a wonderful time in Portland and numerous situations here at the institute at after-work activities, **Wilfried Sigle** for reading and reviewing all of my manuscripts in advance, **Yi Wang** for showing me many different tricks at the microscope and data evaluation, and **Xu Chen** for the countless after-work activities and his helpful comments on the microscope.

I want to sincerely thank and emphasize my wonderful girlfriend, **Nina Juppe**, who supported me at all times no matter my condition. It is not only a great help but also a pleasure to have you on my side.

An dieser Stelle will ich meiner gesamten Familie danken, die mich immer aufgefangen hat während der letzten Jahre und mich stets unterstützt hat.

1 Introduction

1.1 Motivation

The fundamental mechanisms behind quantum phenomena in complex oxides, such as giant or colossal magnetoresistance,[1–3] high-temperature superconductivity,[4,5] or Josephson junctions,[6,7] are key for the prospective application of these phenomena. Quantum materials hold great promise for various technological applications, including next-generation electronics,[8,9] spintronics,[10,11] and energy conversion devices.[12,13] However, exploiting the full potential of complex oxides requires precise control over their composition, crystalline structure, and interface quality.[14–18] Nevertheless, quantum materials are not only interesting from a practical point of view but also for fundamental research, where solid theories are developed to describe and understand the world around us.[19–22] The intricate interplay between the atomic structure and emergent properties of complex oxide materials has positioned them at the forefront of modern materials science. Therefore, a deep understanding of the structure-property relationships governing these materials is essential. Especially, local distortions, lattice modulations, and domain boundaries provide crucial insights into how structural variations influence the material's properties at different length scales.[23–25]

Among the various characterization techniques available, scanning transmission electron microscopy (STEM)[26–28] has emerged as a pivotal tool in unraveling the intricate atomic arrangements that underpin the remarkable functionalities of complex oxide materials. With the ability to image materials at the atomic scale, STEM provides a direct observation into the arrangement of atoms within complex oxide structures.[29] This level of resolution is indispensable for identifying crystal defects, interfaces, and nanoscale variations in composition – all of which play pivotal roles in dictating the material's properties.[14–18] Moreover, spectroscopic techniques, such as electron energy-loss spectroscopy (EELS), enable the identification of elemental composition and electronic states with remarkable precision.[30,31] This, in turn, allows for the correlation of specific atomic arrangements with the electronic and magnetic behaviors observed in complex oxide materials.[30,32] Another compelling feature of STEM is its versatility in imaging both crystalline and non-crystalline regions of materials.[33,34] In complex oxide materials, where the emergence of novel properties is often intertwined with local structural deviations, this capability becomes paramount.

The growth of quantum materials as ultra-thin films with molecular beam epitaxy (MBE) enables the study of unprecedented pure materials and allows for the deduction of structure-property relationships.[35–38] Unlike other growth methods, MBE offers the unique advantage of producing single crystalline layers with atomic-scale accuracy. This level of control is crucial for tailoring the properties of complex oxide structures, as even slight variations in the composition or the arrangement of atoms can lead to dramatic changes in their physical properties.[39,40] Furthermore, MBE enables the growth of heterostructures and artificially layered architectures, allowing for the engineering of interfaces between different oxide materials.[41] These interfaces can exhibit emergent properties, such as interfacial SC,[42] or interfacial ferromagnetism (FM),[43,44] which are not present in the individual materials, leading to novel phenomena and functionalities. By carefully selecting the deposition conditions and monitoring the growth process in real-time utilizing reflection high-energy electron diffraction (RHEED), it is possible to fine-tune the structural and electronic properties of each atomic layer, creating intricate oxide structures with tailored properties.[37,40,45] In addition, heterostructures with different physical properties can

be used to investigate the structural and electronic interplay between different quantum states.[37,46,47]

1.2 High-T_C Cuprates

Superconductivity displays one of the most captivating and transformative discoveries in condensed matter physics.[48–50] Among the myriad of materials explored for superconducting applications, cuprates have emerged as paramount contenders, captivating the scientific community with their high superconducting transition temperatures and the ongoing debate about the origin and mechanism of the latter.[37,42,46] Cuprates exhibit a diverse range of properties, encompassing antiferromagnetic insulators,[51,52] pseudogap phases,[52,53] superconductivity,[42,54] and metallicity,[37,52] making them a versatile and interesting class of materials in physics and materials science, c.f. Fig.1. The intricate interplay of charge, spin, and lattice degrees of freedom within cuprates not only challenges the theoretical understanding but also offers a tantalizing playground for investigating novel quantum phases and emergent phenomena.[52,55]
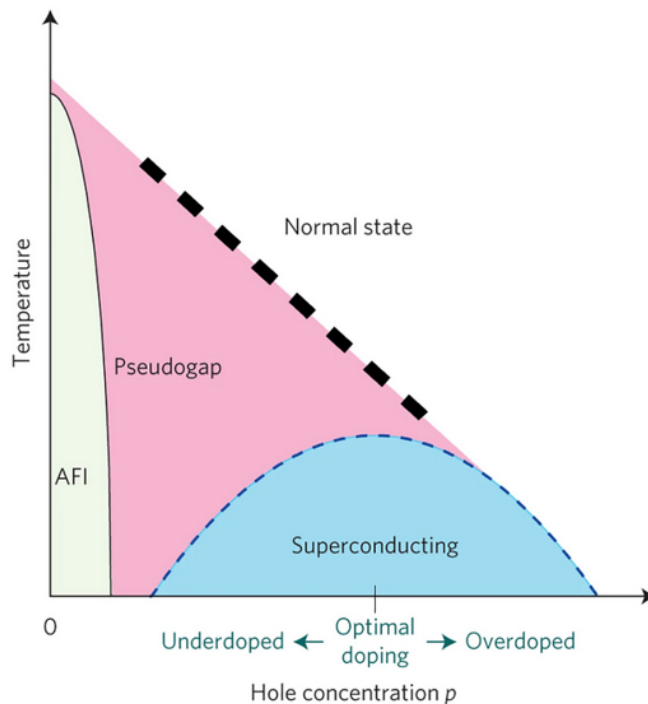

Figure 1: Phase diagram illustrating the rich and complex interplay between antiferromagnetic insulating, superconducting, pseudogap, and metallic phases in cuprate materials as a function of temperature and hole doping p. Figure has been reproduced with permission from Ref.[53]

The enduring significance of cuprates in superconductivity is underscored by their potential to revolutionize practical applications.[56] The prospect of achieving superconductivity at relatively higher temperatures opens avenues for efficient and cost-effective energy transmission and storage. Furthermore, cuprates' distinctive electronic and magnetic properties engender opportunities for developing novel electronic devices,[39,57,58] quantum computing elements,[56,59–61] and advanced sensors.[62–64] Despite decades of investigation, the underlying mechanism behind high-temperature superconductivity in cuprates remains a subject of fervent debate, pushing forward the frontiers of condensed matter physics and materials science.[65,66]

Crystallographic and Electronic Structure of La$_{2-x}$Sr$_x$CuO$_4$. The parent compound La$_2$CuO$_4$ exhibits a K$_2$NiF$_4$-type crystal structure, characterized by alternating layers of corner-sharing CuO$_2$ square-planar units and La$_2$O$_2$ rock-salt-like layers, and an I 4/m m m symmetry.[67] A more comprehensive understanding of the inherent electronic properties can be attained by directing attention to the fundamental CuO$_6$ octahedral units constituting the crystal structure. The CuO$_6$ octahedral units undergo octahedral crystal-field splitting, where the degeneracy of the Cu 3d orbitals is lifted due to the crystal field created by the surrounding oxygen ligands, resulting in distinct energy levels and the splitting of e$_g$ and t$_{2g}$ orbitals. In the next step, a hole occupies the 3d$x^2 - y^2$ orbital lowering the energy of the double-occupied 3dz^2 orbital in the Cu^{2+} ion, leading to an elongation of the CuO$_6$ octahedral unit due to a strong Jahn-Teller distortion as indicated in Fig. 2.[68]
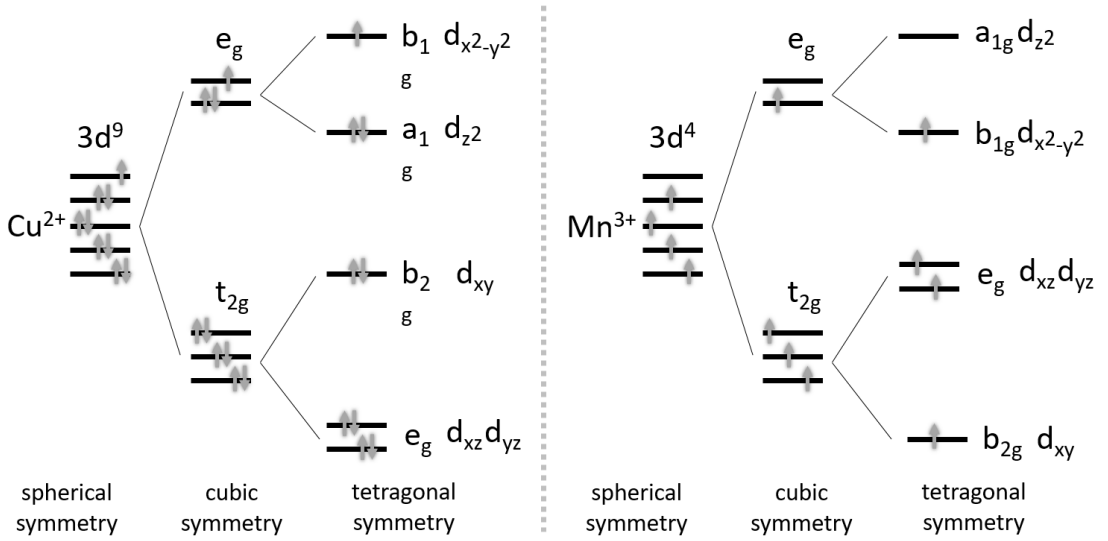

Figure 2: Jahn Teller elongation (left) and compression (right). Left: Crystal field splitting of La$_2$CuO$_4$ in a spherical, cubic, and tetragonal symmetry of the oxygen ligands around the central Cu^{2+} ion.[68] Right: Crystal field splitting of LaMnO$_3$ in a spherical, cubic, and tetragonal symmetry of the oxygen ligands around the central Mn^{3+} ion.

The Jahn-Teller distortion in undoped La$_2$CuO$_4$ is partially alleviated upon Sr doping, resulting in an anti-Jahn-Teller distortion attributed to the Sr-induced lattice deformation as indicated in Fig. 3.[68,70] These deformations can be visualized through annular bright field imaging of the apical oxygen distances, providing insight into the structural deformations in the material.[71–73]

As indicated in Fig. 4, the introduced dopant holes have two different possibilities to couple with the itinerant Cu 3d^9 hole: i) In Fig. 4a the dopant hole occupies an antibonding a$^*_{1g}$ molecular orbital, which consists of six oxygen p$_\sigma$ orbitals and one Cu 3d$_z{}^2$ orbital, resulting in a parallel coupling with the itinerant hole and the formation of a spin-triplet that is called "Hund's coupling triplet".[68] ii) In Fig. 4b the dopant hole occupies a bonding b$_{1g}$ molecular orbital, which consists of four oxygen p$_\sigma$ orbitals and a part of the Cu 3d$x^2 - y^2$ orbital, resulting in an antiparallel coupling with the itinerant hole and the formation of a spin-singlet, which is called "Zhang-Rice singlet".[74]

First-principles calculations have shown that both scenarios are energetically nearly degenerated through the anti-Jahn-Teller effect and a coexistence of these states is important for the formation of the superconducting and metallic quantum states in La$_{2-x}$Sr$_x$CuO$_4$.[68]
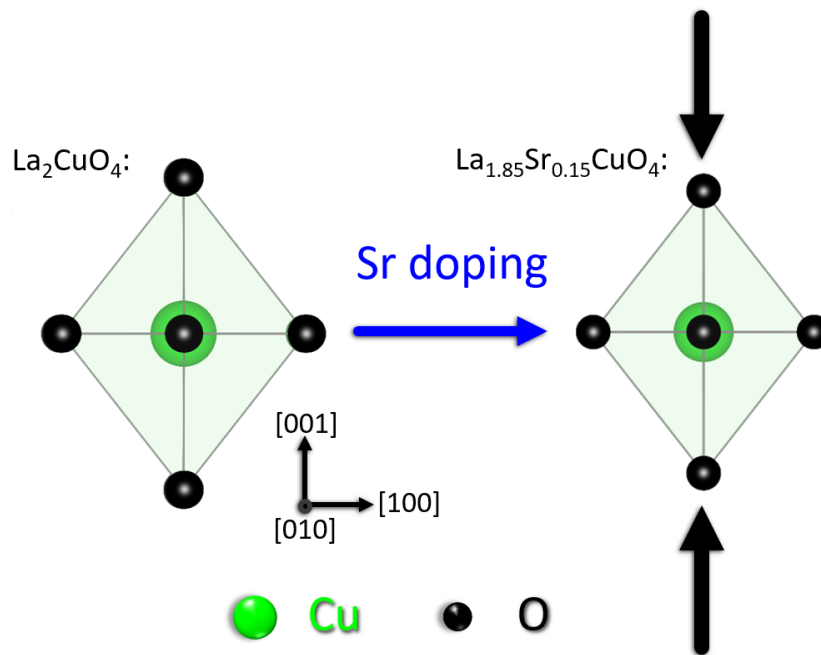
Figure 3: Comparison of the CuO_6 octahedral units between La_2CuO_4 (left) and Sr-doped $La_{1.85}Sr_{0.15}CuO_4$ (right), where the contraction induced by Sr substitution is visualized using black arrows. The figure has been produced by the software VESTA.[69]
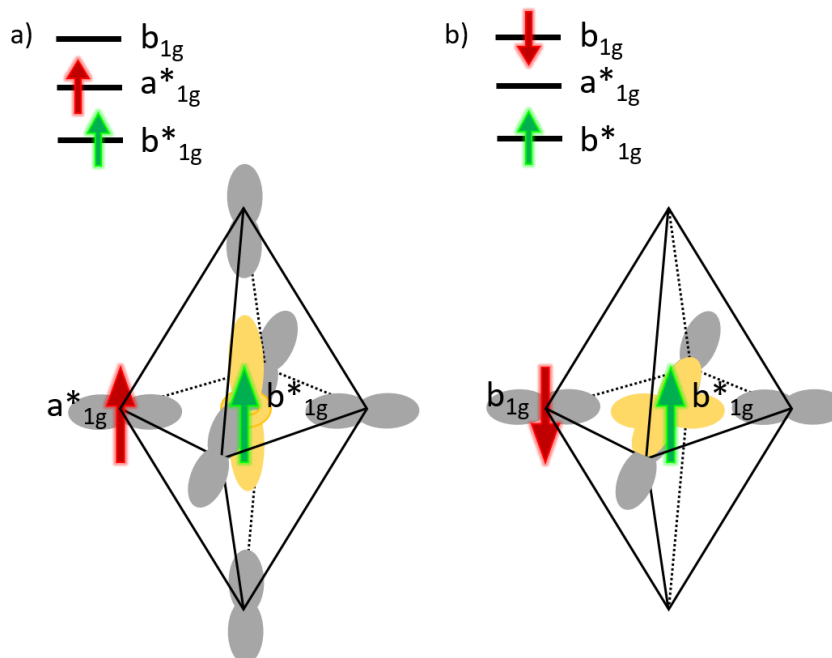

Figure 4: Comparison of the parallel coupling forming a Hund's triplet (a) and the antiparallel coupling forming a Zhang-Rice singlet (b). The red arrows denote the dopant hole and the green arrows denote the Cu $3d^9$ hole. The grey orbitals highlight the O $2p_\sigma$ orbitals and the yellow orbitals in panels a and b highlight the Cu $3dz^2$ and Cu $3dx^2\text{-}y^2$ orbitals, respectively.[68]

La$_{2-x}$Sr$_x$CuO$_4$ with x = 0 is a prototypical example of a charge-transfer insulator, characterized by the suppression of electronic conductivity despite the presence of partially filled electronic bands.[75] To understand the band gap in cuprates one usually starts within the simplified framework of the Hubbard model, describing the division of Cu 3d orbitals into the upper and lower Hubbard bands (UHB and LHB).[20] Based on this sub-band splitting, the Hubbard parameter U plays a pivotal role in establishing the band gap between the LHB and the UHB. The Hubbard parameter U competes with mobile charge carriers inside the material, which is described by the Hubbard Hamiltonian:

$$\hat{H} = -t \sum_{\langle i,j \rangle, \sigma} (\hat{c}^{\dagger}_{i,\sigma} \hat{c}_{j,\sigma} + \hat{c}^{\dagger}_{j,\sigma} \hat{c}_{i,\sigma}) + U \sum_i \hat{n}_{i,\uparrow} \hat{n}_{i,\downarrow}$$

In this expression, $\hat{c}^{\dagger}_{i,\sigma}$ ($\hat{c}_{i,\sigma}$) is the creation (annihilation) operator for an electron with spin σ on site i. These operators add or remove an electron from the specified site and spin state. The sum $\sum_{\langle i,j \rangle, \sigma}$ runs over pairs of neighboring sites $\langle i, j \rangle$ and spin states σ, reflecting the hopping of electrons between sites. Additionally, $\hat{n}_{i,\sigma}$ is the number operator that counts the occupancy of site i with an electron of spin σ. The term $\hat{n}_{i,\uparrow} \hat{n}_{i,\downarrow}$ in the Hamiltonian represents the Coulomb interaction between electrons with opposite spins on the same site i, with U as the associated energy cost for double occupancy. The first term, involving hopping, promotes electron delocalization, while the second term, involving Coulomb repulsion, favors charge localization and electron correlations, leading to a comprehensive description of the interplay between these effects in the electronic behavior of oxide materials such as cuprates.
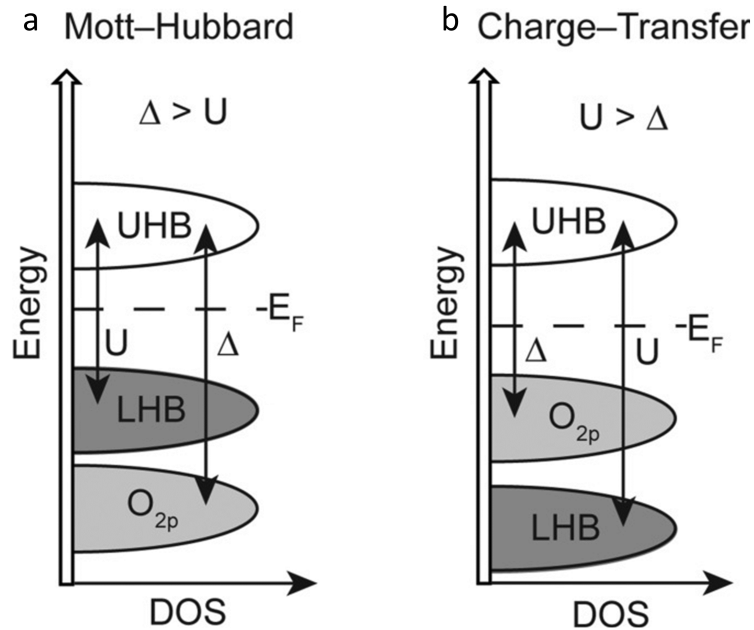

Figure 5: Classification of (**a**) Mott-Hubbard and (**b**) Charge-Transfer insulators. The figure has been reproduced with permission from Ref.[76]

However, to further understand the band gap in cuprates, it is essential to account for the oxygen 2p orbitals. La$_2$CuO$_4$ manifests its insulating behavior due to a pronounced charge transfer process involving the formation of Δ, which can be attributed to the energetic disparity between the occupied oxygen 2p band and the unoccupied UHB.[75] This

electronic behavior is described by the Zaanen-Sawatzky-Allen scheme, resulting in the classification of two main categories: i) Materials with $\Delta > U$ exhibit an energy gap at the Fermi level originating from a Mott-Hubbard-type splitting of the transition metal d-band, c.f. Fig. 5.[21] ii) Materials with $\Delta < U$ displaying a gap that separates transition metal d states from ligand p states, known as the charge transfer gap.[21] Note that the Δ/U ratio is a crucial parameter for the distinction between a Mott-insulator and a charge transfer insulator. Therefore, changes in the crystal symmetry or the chemistry of the crystal, i.e., the change of the A-site cation, can lead to drastic changes in the electronic band structure of materials. Doping of the charge-transfer insulator La_2CuO_4 with Sr induces a transformation in its electronic properties, due to hole doping on the ligand site.[17] This is in stark contrast to Mott insulators, where holes are introduced into the transition metals' orbitals.[75] As a result, the $La_{2-x}Sr_xCuO_4$ system evolves from an antiferromagnetic charge-transfer insulator for x = 0 to a metallic state upon Sr doping, characterized by the emergence of a finite density of states around the Fermi level. This fermionic quasiparticle holds significant importance for spectroscopic analyses, as its presence becomes directly discernible as a distinct characteristic within the pre-edge region of the O-K edge.[77]

1.3 Manganites

Manganites have garnered immense importance in modern physics owing to their remarkable colossal magnetoresistance.[78] This exceptional property refers to the drastic change in electrical resistance exhibited by these materials in response to an external magnetic field. The discovery of colossal magnetoresistance has not only unveiled fascinating insights into the intricate interplay between charge, spin, and lattice degrees of freedom in strongly correlated electron systems,[9] but it has also ignited extensive research efforts toward harnessing this effect for potential technological applications in electronic devices, such as magnetic sensors and memory elements.[79,80] Besides their intriguing colossal magnetoresistance behavior, manganites stand as compelling platforms for investigating emergent electronic phases and pushing the boundaries of our understanding of condensed matter physics.[78,81] In addition, manganites encompass various configurations, including perovskites and distinctive Ruddlesden-Popper phases as indicated in Fig. 6.

In the simplest case, the cubic perovskite phase can be described by the formula ABO_3. A-site ions encompass a range of large species, including rare-earth, alkaline-earth, alkali, or notable entities like La^{3+} or Sr^{2+}, forming coordination with 12 oxygen atoms. In this case, the B-site ions comprise the 3d transition metal Mn. The Goldschmidt tolerance factor (t) provides insight into the stability of perovskite structures by evaluating the balance between the ionic radii of A-site and B-site cations, aiding in predicting whether a given combination of cations will form a stable perovskite lattice as shown in Eq. 1.[82]

$$t = \frac{r_A + r_O}{\sqrt{2}(r_B + r_O)} \tag{1}$$

Here, r_A represents the ionic radius of the A-site cation, r_B denotes the ionic radius of the B-site cation, and r_O signifies the radius of an oxygen anion. The dimensionless Goldschmidt tolerance factor provides a criterion for stable crystal structures in the range $0.8 \leq t \leq 1.0$, indicating a balanced match between the sizes of A-site and B-site cations and the surrounding oxygen atoms.
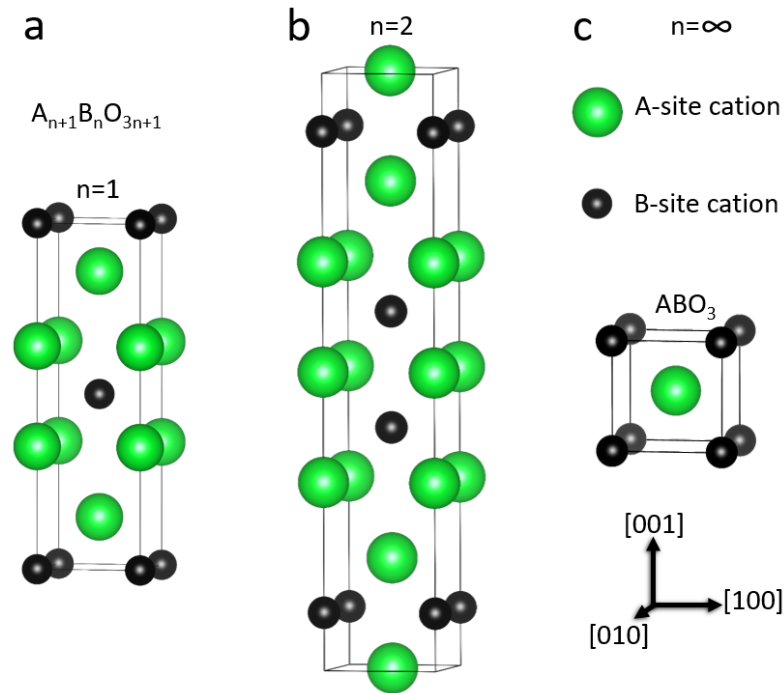
Figure 6: Ruddlesden-Popper family with the n=1 (**a**) A_2BO_4 phase, the n=2 (**b**) $A_3B_2O_7$ phase, and the perovskite-type phase (**c**) ABO_3 with n=∞. The figure has been produced with the software VESTA.[83–85]

Outside this range, deviations may lead to structural distortions or phase transitions. Related to the perovskite structure, Ruddlesden-Popper phases are hosting a broad spectrum of electronic states, ranging from insulating to metallic, showcasing a fertile ground for investigating emergent phenomena and intricate phase transitions. The Ruddlesden-Popper phases are essentially composed of alternating layers of rock-salt and perovskite structures, and their general formula is given by $A_{n+1}B_nO_{3n+1}$. Magnetism, crystallography, and electronic behavior in Ruddlesden-Popper phases present a captivating platform for advancing the general comprehension of condensed matter physics and applications in materials science.[36,86–88]

SrMnO$_3$ and LaMnO$_3$. The phase diagram of the ABO_3-type perovskite $La_{1-x}Sr_xMnO_3$ exhibits a broad array of electronic and magnetic phases, ranging from antiferromagnetic insulators to ferromagnetic metals, as a function of Sr doping (x) as it is highlighted in Fig. 7.[89] Interestingly, the ferromagnetic dome observed in manganite materials coincides precisely with a hole concentration that is twice that of the superconducting dome observed in cuprate materials. This intriguing correlation between cuprate and manganite domes has not been understood so far and is the subject of our ongoing research and investigations.
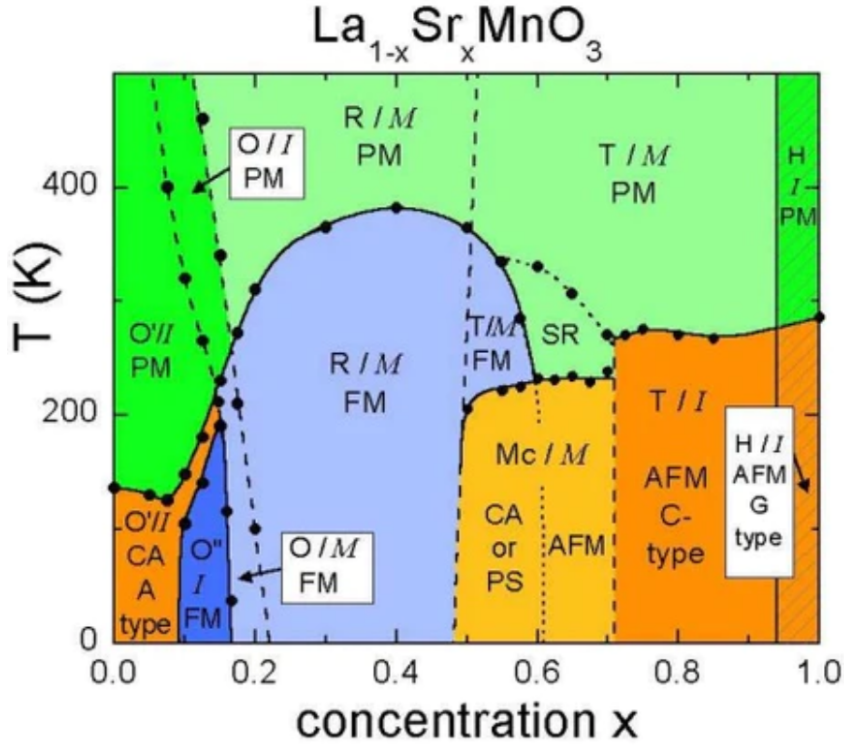
Figure 7: $La_{1-x}Sr_xMnO_3$ displays a broad variety of different crystal structures, including Jahn-Teller distorted orthorhombic (O'), orthorhombic (O), orbital-ordered orthorhombic (O"), rhombohedral (R), tetragonal (T), monoclinic (Mc), and hexagonal (H), alongside distinctive magnetic configurations: paramagnetic (PM, green), short-range order (SR), canted (CA), A-type antiferromagnetic (AFM, depicted in yellow), ferromagnetic (FM, blue), phase-separated (PS), and AFM C-type structures. The electronic states are identified as insulating (I, in dark), and metallic (M, in light). The figure has been reproduced with permission from Ref.[89]

$Sr_{2-x}La_xMnO_4$. Despite the notable significance of A_2BO_4-type oxides as being the parent compound of high-T_C superconducting cuprates and other numerous intriguing properties arising from charge, spin, and orbital interactions,[90] relatively limited attention has been directed towards the charge-transfer, antiferromagnetic insulator $Sr_{2-x}La_xMnO_4$.[91–93] This compound is the n = 1 member of the Ruddlesden-Popper family with a maximum La content of $x = 1$.[93]

In the context of atomic-layer-by-layer growth monitored by *in situ* RHEED, I employ the term monolayer (ML) to delineate individual atomic layers, distinct from the conventional term unit cell (u.c.), see black box in Fig.8. This distinction between ML and u.c. becomes particularly crucial when growing 214-type structures, where the Bragg diffraction spots saturate for each ML instead of each u.c. as compared to 113-type structures.

We have carefully selected $LaSrMnO_4$ because it crystallizes in the same K_2NiF_4-type tetragonal structure *I4/mmm* as optimally doped $La_{1.84}Sr_{0.16}CuO_4$ and due to their perfect epitaxial match (a-axis of $La_{1.84}Sr_{0.16}CuO_4 = 3.774$ Å).[94–96] Furthermore, $SrLaMnO_4$ reaches the solubility maximum of La in the parent compound Sr_2MnO_4, which makes it the perfect candidate for an interface with superconducting $La_{1.84}Sr_{0.16}CuO_4$ since La/Sr intermixing is inherently minimized. On top of that, the Ruddlesden Popper n=2 type has the advantage that there is no direct Mn-O-Cu bond,[97] as compared to the n=∞ perovskite-type $SrMnO_3$. Therefore, $LaSrMnO_4$ as an antiferromagnetic Mott
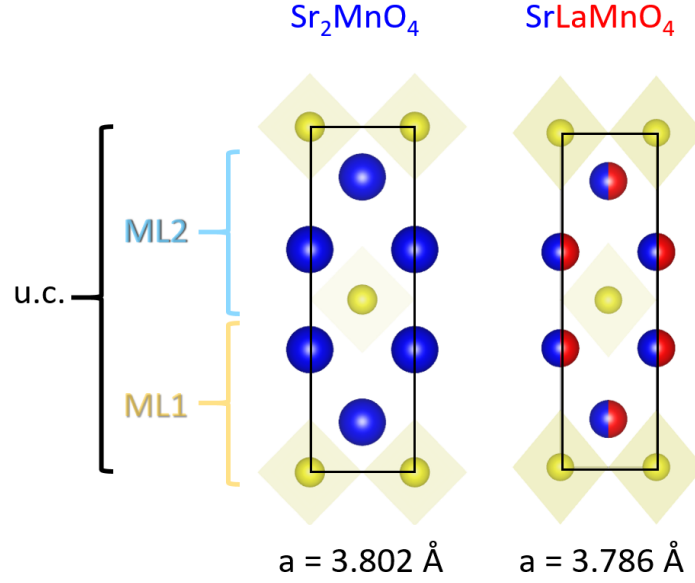
Figure 8: Difference between unit cell (u.c.) and monolayer (ML). On the left side is the undoped Sr_2MnO_4; on the right side is the La-doped $SrLaMnO_4$. The individual a-axis parameters of the two distinct materials are shown below the respective crystal structure. Sr is depicted in blue, La in red, and Mn in yellow. The figure has been produced with the software VESTA.[94,95]

insulator is a promising candidate as a barrier material[94] in $La_{1.84}Sr_{0.16}CuO_4$-$LaSrMnO_4$-$La_{1.84}Sr_{0.16}CuO_4$ high-T_C Josephson junctions.

1.4 Oxide Interfaces

The precise manipulation and control of interfaces in oxide materials have emerged as pivotal aspects of modern semiconductor science and engineering.[18] Interfaces between different oxide materials often dictate the overall functionality and performance of devices,[39,40,98] influencing properties ranging from electronic conductivity[99] and magnetic behavior[100] to catalytic activity.[101] The huge variety of distinct parameters, such as strain,[102] charge,[91] spin,[52] and orbital degree of freedom[55] at oxide interfaces enables the design of novel and exotic materials like multiferroics, non-centrosymmetric superconductors, or magnetic superconductors as indicated in Fig. 9.

Therefore, oxide interfaces hold paramount importance in contemporary research, offering a fertile ground for uncovering novel quantum mechanical phenomena and facilitating groundbreaking advancements in the realms of condensed matter physics and quantum materials. This thesis aims to widen the knowledge about oxide interfaces in chapters 3 and 4 and present the formation of a new type of interface in chapters 5 and 6, namely the step-edge interface, that pushes the boundaries of thin film technology literally toward a new dimension by enabling the controlled growth in two directions instead of just one direction as compared to conventional thin film growths.

Structural and Chemical Coherence of Interfaces. The coherence of oxide interfaces pertains to the degree of crystallographic compatibility regarding their lattice parameters (crystal system and crystal axes values) and the individual chemical potential $\mu_i = \left(\frac{\partial G}{\partial n_i}\right)_{T,p,n_j}$ (change of the Gibbs free energy G regarding the number of changing
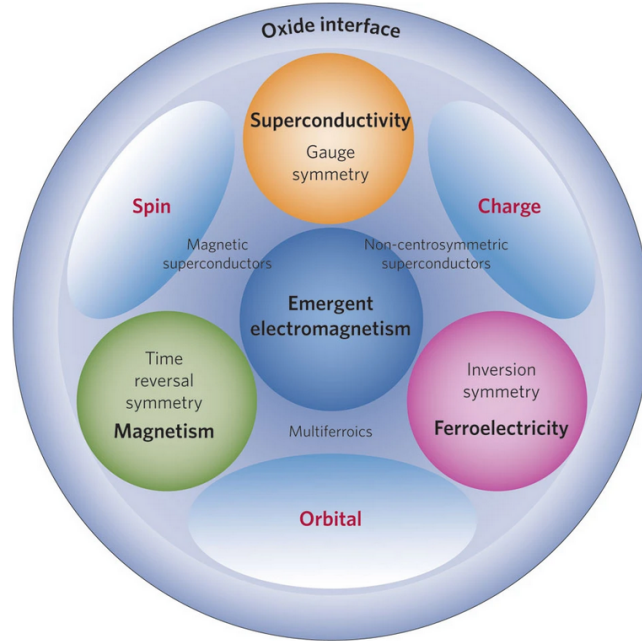
9

Figure 9: Interplays at oxide interfaces. The figure has been reproduced with permission from Ref.[55].

elements n_i, at constant temperature T, constant pressure p, and constant number of element n_j) between the adjoining oxide layers. Coherent oxide interfaces exhibit a seamless continuation of crystallographic orientation, c.f. Fig. 10a, fostering enhanced interactions and emergent phenomena at the interface. For example, a coherent interface between two oxide materials, such as two perovskite oxides with similar lattice parameters can lead to remarkable effects like interface-induced magnetism[103] or superconducting behavior[57] that diverges significantly from the properties of the individual bulk materials.
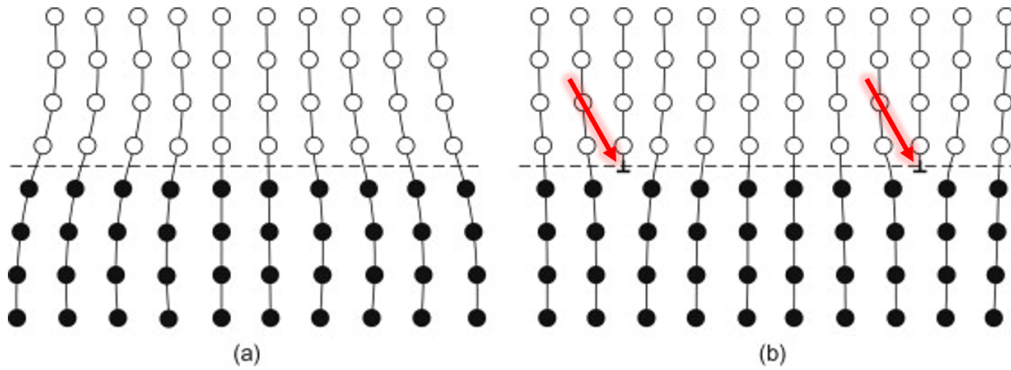
Figure 10: (a) Coherent interfaces and (b) semi-coherent interfaces with local incoherences, here so-called misfit dislocations, pointed out by the red arrows. The figure has been adopted with permission from Ref.[104].

In contrast, an incoherent interface, c.f. Fig. 10b, lacks this seamless structural connectivity, resulting in disrupted electronic and structural alignment between neighboring oxide layers.[104] Factors such as substantial lattice mismatch or the presence of defects are major factors for the occurrence of incoherent interfaces.[104,105]

Incoherent interfaces result in diminished spin and orbital interactions and, hence, reduce the potential for observing novel phenomena.[14–18,39,40,55,105] Therefore, in this thesis, it is pointed out how to avoid the formation of incoherent interfaces and what are the consequences of local incoherences for the subsequently deposited thin films.

Step Edges. In thin film technology, a general objective is to minimize the presence of step-edges, as they can lead to the formation of 2D defects such as antiphase boundaries, change in growth modes from layer-by-layer to step-flow growth, and contribute to elevated levels of interface and surface roughness in thin films.[106] In the framework of this thesis, however, these step-edges serve as the major starting point for the introduction and realization of a novel growth model, namely the bi-directional growth of thin films, allowing for the growth in the in-plane and out-of-plane direction simultaneously. Beyond this unique growth behavior, it is shown in Chapter 5 that step edges also wield the potential to prohibit the formation of antiphase boundaries, adding a layer of complexity and intrigue to the interfacial structure and properties of complex oxide thin films.

The elucidation of atomistic growth mechanisms has predominantly rested upon the terrace-step-kink (TSK) model of a surface structure as depicted in Fig. 11. Apart from delineating terraces, steps, and kinks, Fig. 11 illustrates various elemental components pertinent to film growth: an adsorbed atom (adatom) and a vacant site on the upper terrace, an adsorbed dimer (ad-dimer), as well as a larger island containing four atoms.[106]
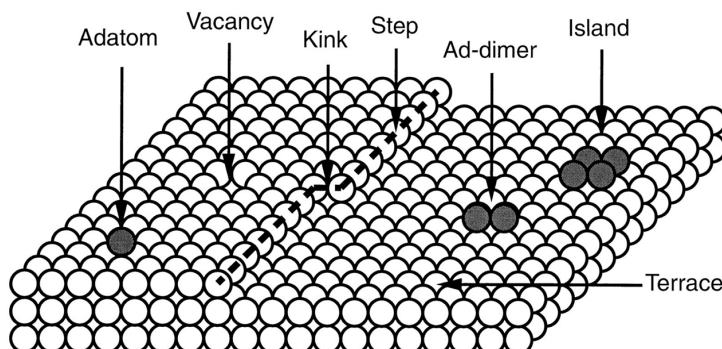
Figure 11: Visualization of a characteristic step-edge occurring at the surface of substrates. The TSK is applied to a simple cubic crystal configuration. Substrate atoms are depicted as white circles, and a dashed line demarcates the position of a step that divides the upper and lower terraces, exhibiting a kink along the step's trajectory. The step descends from left to right. Additionally, black circles denote atoms adsorbed onto the terraces. The figure has been adopted with permission from Ref.[106].

The consequences of kinks and steps on the surface terraces are instabilities that manifest themselves in two different forms: i) meandering, characterized by the transformation of an initially linear step into a wavy configuration, and ii) bunching, characterized by the evolution of a sequence of initially equally spaced steps into regions of high step density, known as step bunches, interspersed with broad flat terraces.[107–109] Point defects such as isolated vacancies, especially oxygen vacancies, have recently attracted much interest because of their effect on the catalytic, electronic, and optical properties of thin films.[110–112] The effects of island formations and deposited atoms on the growth kinetics are discussed in the following section.

1.5 Molecular Beam Epitaxy

Molecular beam epitaxy (MBE) has ushered in a transformative era in thin film technology by enabling exquisite control over the growth of crystalline films with atomic precision.[40] This technique has revolutionized the field through its ability to deposit layers of atoms or molecules onto a substrate surface, in a layer-by-layer manner, facilitating the creation of thin films with highly tailored properties, such as emerging high-T_C superconductivity,[37,42,46] thermoelectricity,[113] ferromagnetism,[44,103] and metallicity.[38,57]

A significant breakthrough emerged when MBE was coupled with an ozone delivery system, allowing for the growth of high-quality complex oxide heterostructures, and an *in situ* controlled RHEED setup.[40,41] This integration unveiled an unprecedented capability to fabricate complex oxide heterostructures with unparalleled purity. The ozone delivery system introduced a novel means of controlling the oxidation of the metals during deposition, that is stabilizing intricate complex oxide compounds. Meanwhile, the *in situ* RHEED enabled real-time monitoring of crystal growth, ensuring precise atomic layer-by-layer assembly. Together, this advanced synergism of MBE, ozone delivery, and *in situ* RHEED has opened new avenues for engineering and exploring the properties of complex oxide thin films, thereby pushing forward the development of cutting-edge electronic, spintronic, and magnetic devices.
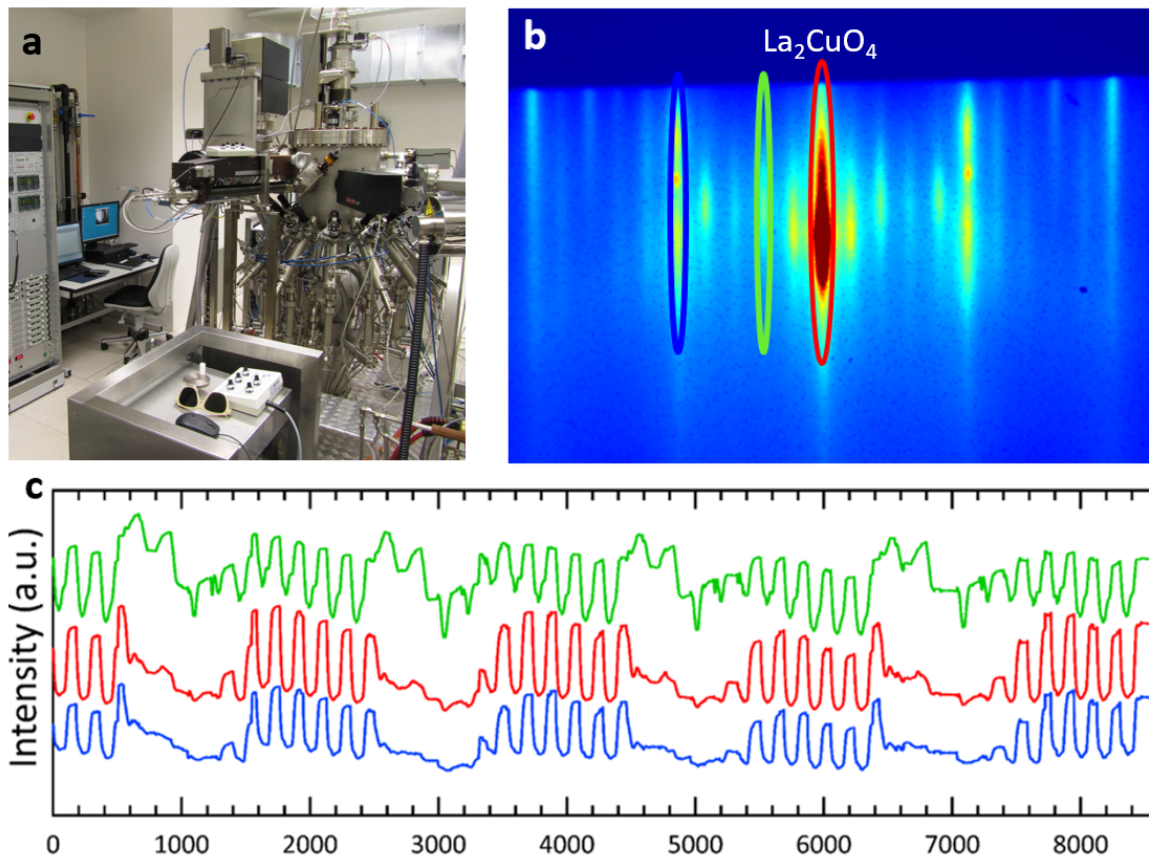
Figure 12: (**a**) MBE system equipped with an ozone generator. (**b**) *In situ* RHEED pattern of La$_2$CuO$_4$ with the main spot (red ellipse), Bragg diffracted spot (blue ellipse), and superstructure spot (green) to control the shutter times of the metal evaporation cells. (**c**) RHEED oscillations of the RHEED spots are depicted in **b**. The figure has been reproduced from Ref.[114]

Growth of Complex Oxide Heterostructures. The fundamental growth of complex oxide heterostructures by MBE is governed by four distinct growth mechanisms: i) Frank-van der Merwe, ii) Volmer-Weber, iii) Stranski-Krastanov, and iv) Step-Flow type growth.[115]
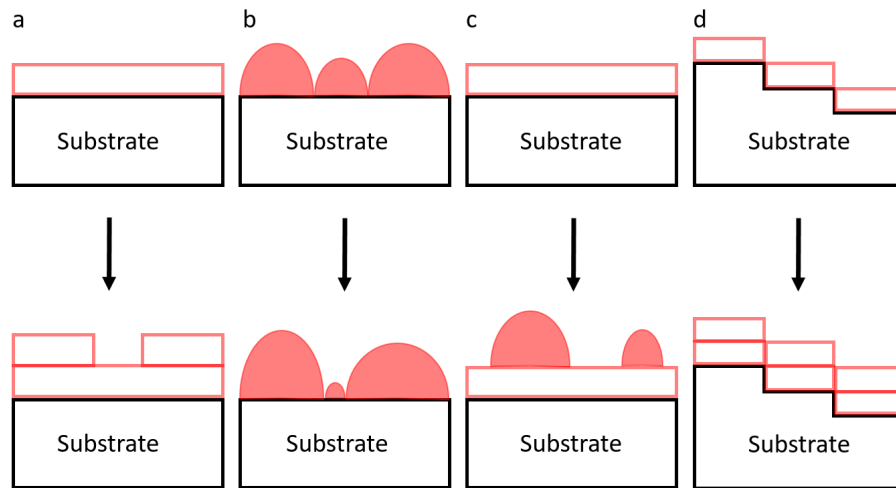
Figure 13: Illustration of four distinct modes of epitaxial growth: (**a**) two-dimensional layer-by-layer growth (Frank-van der Merwe), (**b**) three-dimensional growth of islands (Volmer-Weber), (**c**) layer-by-layer growth succeeded by island growth upon a critical thickness (Stranski-Krastanov), and (**d**) epitaxial growth in a step-flow like pattern. This figure has been inspired by Ref.[115]

In the context of Frank-van der Merwe growth, adatoms exhibit a greater interaction with surface sites compared to other ad-atoms, leading to the creation of atomically smooth layers. This process is also called layer-by-layer growth and occurs in two dimensions, signifying that complete films develop before the growth of successive layers takes place. In general, material scientists strive to achieve this type of growth when growing high-quality thin films. An example of this type of growth would be $BiFeO_3$ grown on $SrTiO_3$ and $LaAlO_3$ as indicated in Fig. 14 panel a and b, respectively. For the $BiFeO_3$ film grown on $SrTiO_3$, the formation of islands with a single unit cell height is observed. On the other hand, in the $BiFeO_3$ film on $LaAlO_3$, indications of step-bunching are apparent.
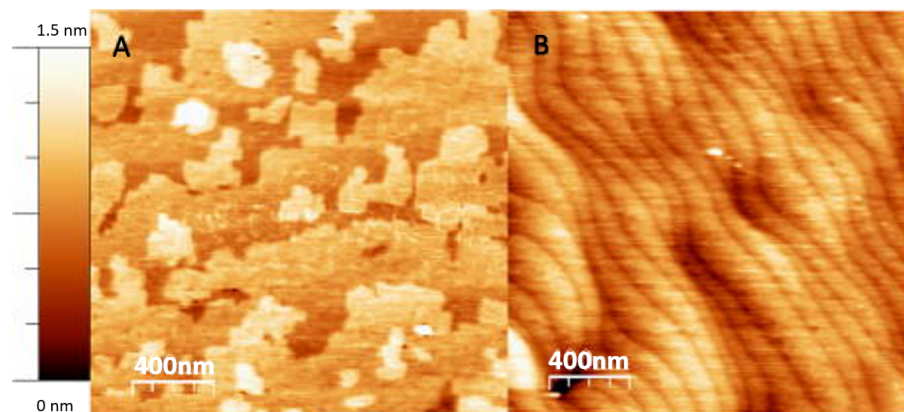
Figure 14: Atomic force microscopy images highlighting the Frank-van der Merwe type of growth. (**A**) $BiFeO_3$ grown on $SrTiO_3$. (**B**) $BiFeO_3$ grown on $LaAlO_3$. This figure has been reproduced with permission from Ref.[116].

In the process known as Volmer-Weber growth, adatom-to-adatom interactions exhibit greater strength compared to the adatom's interaction with the surface. This results in the creation of three-dimensional clusters or islands composed of adatoms. As these clusters develop and consolidate, they contribute to the growth of uneven, multi-layer films on the substrate surface due to Ostwald ripening. An example of Volmer-Weber type growth is the deposition of spinel-type $CoFe_2O_4$ with a lattice parameter of 8.34 Å[117] on $SrTiO_3$ with a lattice parameter of 3.90 Å.[118] Due to their huge lattice mismatch, huge islands are forming as indicated in Fig. 15. By forming islands, the interface between the film and the substrate becomes incoherent, resulting in almost complete relaxation of the strain within the film.
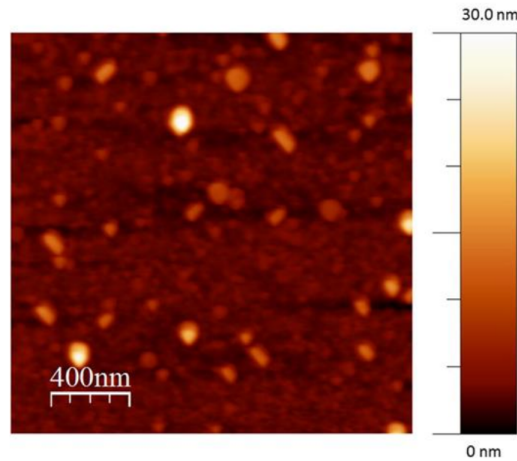
Figure 15: Atomic force microscopy image highlighting the Volmer-Weber type of growth. White dots mark the formation of big islands with a maximum height of around 30 nm. This figure has been reproduced with permission from Ref.[116].

Stranski-Krastanov growth represents an intermediate process marked by a combination of two-dimensional layer growth and three-dimensional island formation. The shift from sequential layer growth to island-centric growth is observed at a critical layer thickness. Various parameters, such as surface energies and lattice parameters of the thin film and the respective substrate greatly influence this critical threshold. An exemplary case of the Stranski-Krastanov type is the growth of $La_{1.78}Sr_{0.22}MnO_3$ on $LaAlO_3$ as shown in Fig. 16.
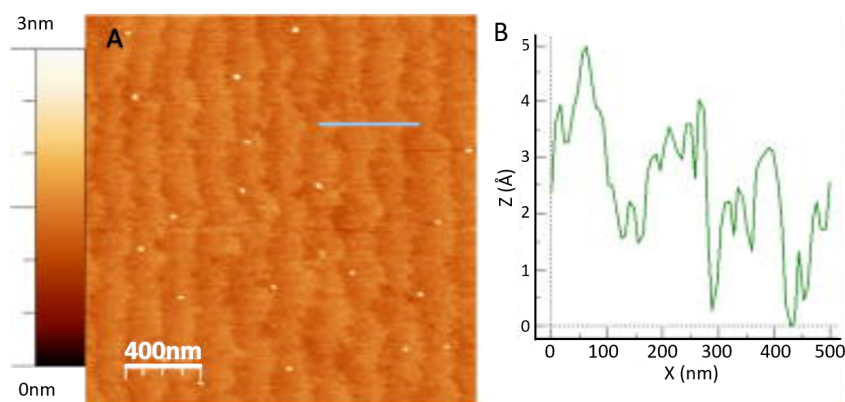
Figure 16: Atomic force microscopy image highlighting the Stranski-Krastanov type of growth. (**A**) White dots mark the formation of small islands with a height of around 3 nm. (**B**) The line profile obtained along the blue line in panel A. This figure has been reproduced with permission from Ref.[116].

Finally, a growth mechanism known as step-flow growth takes place when the distance that mobile particles can traverse across the surface exceeds the width of these terraces. Since no substrate is perfect in terms of surface steps, all surfaces are inherently non-uniform, characterized by a specific degree of tilt or miscut, resulting in terraces possessing finite widths. Upon utilizing vicinal substrates, it is common to cleave the substrate at a vicinal angle, resulting in a surface characterized by an array of atomic height steps.[119] Note that the surface terrace widths play an important role as step bunching can occur for too small angles, c.f. Fig. 17a. Step-flow growth occurs upon growing on vicinal substrates as indicated in Fig. 17b-d.[119]
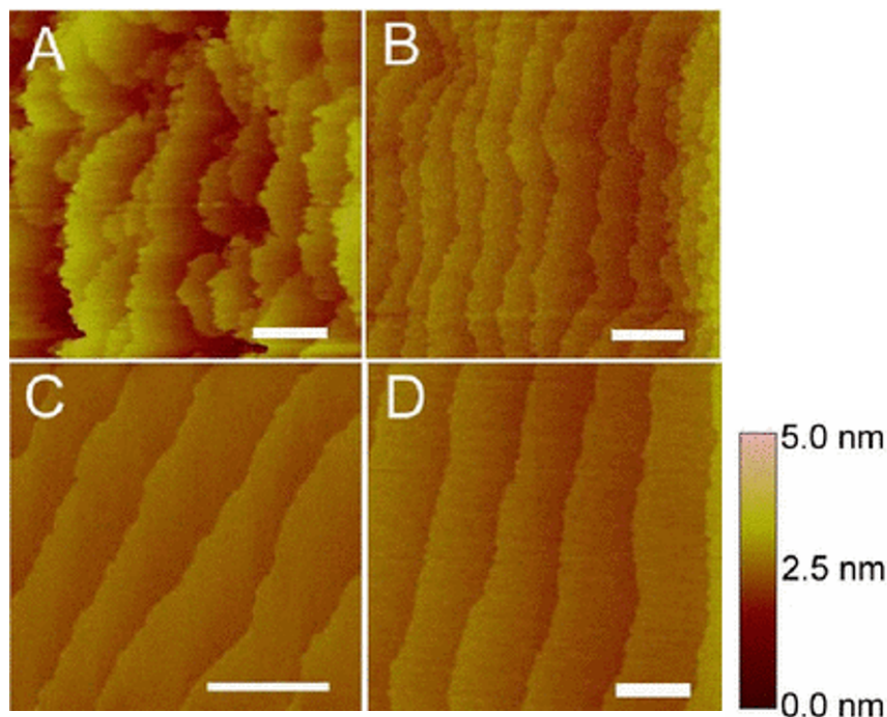
Figure 17: Atomic force microscopy images highlighting the growth on vicinal substrates. $SrRuO_3$ is grown on $SrTiO_3$ with different terrace widths. (**A**) Step bunching manifests on substrates characterized by small terrace width. (**B**),(**C**), (**D**) Smooth surfaces following the steps of the substrates are obtained for intermediate terrace widths. The scale bars represent a length of 10 μm. (**D**) This figure has been reproduced with permission from Ref.[119].

1.6 Scanning Transmission Electron Microscopy

March 9th, 1931, marked the unveiling of the inaugural electron microscope prototype by German physicist Ernst Ruska, who collaborated with his doctoral mentor Max Knoll. This novel and groundbreaking device achieved a magnification of four hundred times and stood as the pioneering embodiment of electron microscopy principles. The discovery of the electron microscope, despite its initial low spatial resolution, which was not better than the best light microscopes they had back then,[120] marked the inception of a journey that ultimately led to the attainment of atomic-scale insights into materials, thereby enabling the current record-holding spatial resolution of less than 20 picometers.[121] After the invention of the first transmission electron microscope (TEM) by Ernst Ruska and his doctoral father Max Knoll, the scanning transmission electron microscope (STEM) was built by Baron Manfred von Ardenne in 1938.[122] However, achieving high resolution in this mode necessitates high current densities and small probe sizes. These requirements

were only fulfilled when Albert Crewe incorporated a cold field-emission current source into the microscope. Finally, the resolution-limiting aberrations in electron microscopes due to the non-prefect electromagnetic lenses have been overcome with the invention of spherical aberration (C_S) correctors paving the way for unraveling the electronic and crystallographic structure of materials at the atomic scale.[123]

In this thesis, the emphasis lies on C_S-corrected STEM, c.f. Fig. 18, particularly when combined with electron energy-loss spectroscopy (EELS). This combination offers an unparalleled level of precision for exploring oxide interfaces, enabling comprehensive insights into their electronic and chemical attributes at the atomic scale.
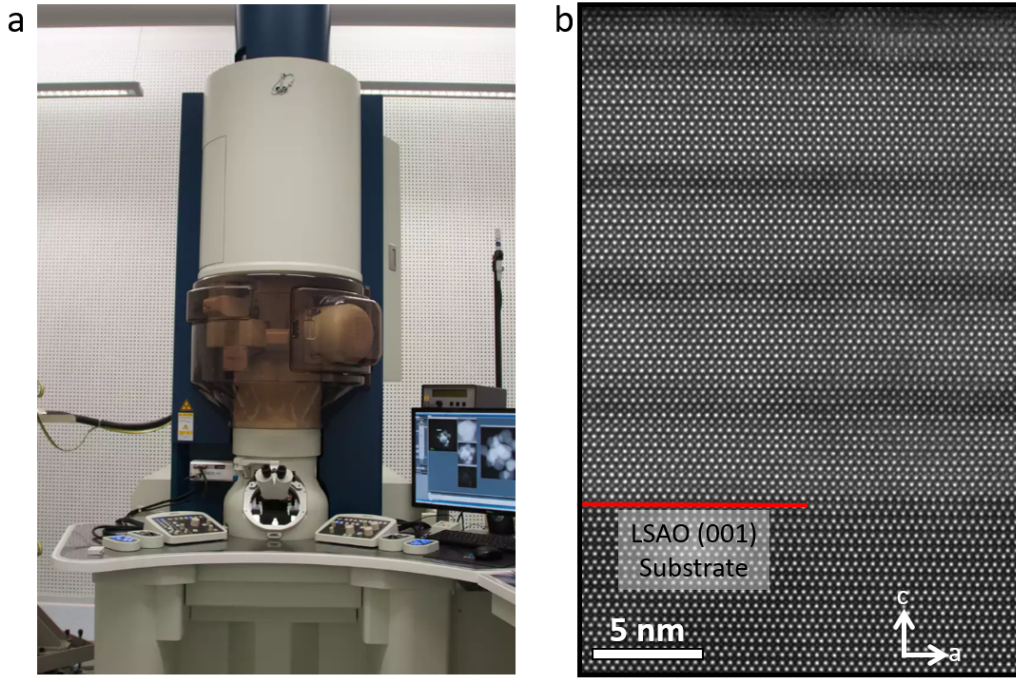
Figure 18: (**a**) The probe-corrected JEOL ARM200F (S)TEM, which was the main instrument used, stands as a cutting-edge instrument renowned for its remarkable stability and ability to generate highly focused probes. Additionally, this microscope is outfitted with sophisticated EELS detectors, facilitating comprehensive chemical analysis. This microscope is equipped with a cold field emission gun and achieves a spatial resolution of 63 pm at 200 kV. (**b**) Atomically resolved annular dark-field image of a superlattice consisting of superconducting $La_{1.84}Sr_{0.16}CuO_4$ and insulating $LaSrMnO_4$ epitaxially grown on $LaSrAlO_4$ (LSAO).

As has been stated in the paragraph above, electron microscopy emerged as a response to the constrained resolution of light microscopes, constrained by the wavelength of visible light ranging between 380-750 nm. Adhering to the conventional Rayleigh criterion for light microscopes, the minimal resolvable distance r_d can be estimated as follows:

$$r_d = 0.61 \cdot \frac{\lambda_{light}}{n \cdot \sin(\alpha)}$$

Here, λ_{light} represents the wavelength of the light, n stands for the refractive index of the intervening medium, and α denotes the collection semi-angle of the magnifying lens. The quantity $n \cdot \sin \alpha$ is often recognized as the numerical aperture, highlighting the extent of angles within which the system can either receive or emit light. This equation

demonstrates that a smaller wavelength leads to an improved resolution. For instance, the resolution limit for a visible light microscope typically remains around 200 nm.

Thanks to the remarkable Ph.D. thesis of Louis de Broglie, we know that electrons can also be described as waves with a certain de Broglie wavelength $\lambda_{deBroglie} = \frac{h}{p}$, where h displays the Planck constant and p marks the momentum of the electron. Derived from this formula, it becomes apparent that the electron's wavelength becomes progressively shorter as its kinetic energy increases, a characteristic directly linked to the microscope's accelerating voltage.

Due to the inherent magnetic field inhomogeneities within magnetic lenses, as elucidated in the preceding paragraph, electron microscopes consistently suffer from spatial resolution-limiting spherical aberrations. Therefore, the probe formed by non-ideal lenses deviates from an ideal Airy disc, which is simply the 2D Fourier transformation of the illuminated aperture in the back focal plane.

Lens Aberrations and Aberration Correction. Aberrations invariably engender different focal lengths across the trajectory of the electron beam. Notably, the pivotal aberrations encompass spherical and chromatic aberrations, alongside astigmatism, which hold paramount significance for inducing image blurring. This deviation of the ideal electron trajectories is caused by a residual phase shift of the electron wave function. In a simplified plane wave approximation $\exp(-i\mathbf{x} \cdot \mathbf{k})$, these aberrations can be easily understood by the so-called probe function Ψ_{Probe}. Here, an inverse 2D Fourier transformation of the aperture function $A(\mathbf{k})$ is applied, which can be further subdivided into an aberration term $\exp(-i\chi(k))$ that defines any change in the phase and another function $H(\mathbf{k})$ defining the shape of the aperture.

$$\psi_{\mathrm{Probe}}(\mathbf{x}) = \int A(\mathbf{k}) \exp(-i\mathbf{x} \cdot \mathbf{k})\, d\mathbf{k} = \int H(\mathbf{k}) \exp(-i\chi(\mathbf{k})) \exp(-i\mathbf{x} \cdot \mathbf{k})\, d\mathbf{k}$$

In this context, $\mathbf{k}$ defines a two-dimensional vector in the back focal plane of the probe-forming lens. Hence, determining the electron beam profile is analogous to propagating an electron wave through a phase plate and assessing the intensity of the resultant wave.[124]

Positive spherical aberration refers to the phenomenon where electrons following trajectories located farther from the center of the electromagnetic lens experience a more pronounced deflection, resulting in a shorter focal length than electrons with trajectories positioned closer to the center of the lenses as depicted in Fig. 19a. Here, the radius of the circle of least confusion $r_{Confusion}$, which is defined as the optimum point of focus, is given by:

$$r_{Confusion} = C_S \cdot \alpha^3$$

where C_S is the sperical aberration coefficient and α denotes the collection semi-angle. The removal of spherical aberrations poses challenges within electron microscopy as with an increasing semi-collection angle, spherical aberrations will get pervasive, prompting the establishment of an entire research domain dedicated to mitigating these types of image blurrings.[125,126] Multipole lenses are used to produce negative spherical aberrations to cancel out the positive spherical aberrations of round lenses.[125–128] These multipole lenses encompass either hexapole configurations or a combined arrangement of quadrupole and

octupole lenses.[125,128] Here, the emphasis is directed toward hexapole lenses, given that a hexapole corrector was implemented within the JEOL ARM200F DCOR microscope, which was used in all STEM investigations. In hexapole correctors, two hexapoles are employed in series, oriented at a 60°rotation from each other, effectively nullifying the first-order effect of the first hexapole through cancellation by the first-order effect of the second hexapole.[125,127,129] This first-order effect is a threefold astigmatic electron beam. To nullify the first-order effect, equivalence in optical planes between the two hexapole lenses must be achieved, which is done by two round transfer lenses between the two hexapole lenses.[127] The second-order effect of the two hexapole lenses introduces a uniform azimuthal distribution and a cubic dependence in the radial direction, effectively producing a round beam with negative spherical aberrations.[127]

The varying focal lengths in the context of chromatic aberrations arise from the differing kinetic energies of electrons, wherein electrons possessing greater kinetic energies exhibit longer focal lengths in comparison to those electrons with lower kinetic energies that scatter stronger and exhibit shorter focal lengths, ultimately creating a circle of least confusion with radius $r_{Confusion}$ at the minimal distance of the converging electron ray paths as depicted in Fig. 19b.

$$r_{Confusion} = \frac{C_C \cdot \alpha \cdot \Delta E}{E_0}$$

Here, C_C is the chromatic aberration coefficient and is approximately equal to the focal length, ΔE is the spread in energy width of the electron beam, and E_0 denotes the accelerating voltage of the microscope. However, when operating the transmission electron microscope at high voltage configurations, the energy spread is as small as 10^{-7} leading to a less pronounced effect of the chromatic aberration as compared to the image blurring due to spherical aberrations. Nevertheless, it is essential to acknowledge that by employing C_S and C_C corrected microscopes, the spatial resolution can be enhanced, as demonstrated by the PICO microscope in Jülich.[130]

Astigmatism occurs for converging electron rays that have different focal lengths depending on the azimuthal angle of the electron beam, i.e., 90°, resulting in horizontal and vertical planes in the electron lens as depicted in Fig. 19c. In this case, $r_{Confusion}$ is defined by the collection semi-angle α and the difference in focal lengths Δf:

$$r_{Confusion} = \alpha \cdot \Delta f$$

Astigmatism correction is achieved through devices known as stigmators, which apply a subtle magnetic (or electric) field to the elliptical beam, resulting in the transformation of the beam into a circular shape.

Axial coma emerges when electron ray trajectories are not parallel to the optical axis, giving rise to distinct focal lengths and focal points that reside off the optical axis. This effect can be reduced upon tilting the electron beam into the coma-free axis.

Besides the aberrations mentioned above, defocus represents the simplest form of aberrations, which can simply be removed by manual focussing of the beam on the sample.
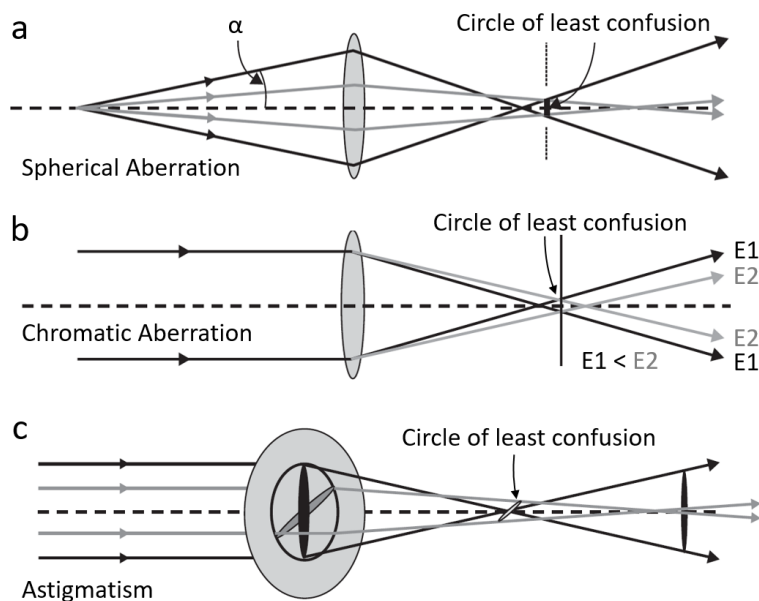
Figure 19: (a) Illustration of positive spherical aberration. (b) Chromatic aberration, where waves with distinct wavelengths and energies (E1<E2) converge at different positions along the optical axis. (c) Astigmatism, where the black plane and the gray plane in the magnetic lens exhibit different focal lengths along the optical axis. α is the collection semi-angle of the lens. The point of minimal aberration effects is represented by the circle of least confusion. Dashed black lines show the optical axes. This figure has been modified with permission from Ref.[131]

STEM Imaging. In STEM, the electron beam is concentrated to form a sub-Å-sized probe and is then raster-scanned across the sample using deflection coils. Owing to the small probe dimensions, cutting-edge STEM imaging enables atomic-scale visualization of the specimen. When a sample is scanned by an electron beam, electrons are scattered at different angles when they transmit the electron-transparent sample, thereby creating a wide variety of different signals that can be used for STEM investigations. In the following discussion, two complementary imaging methodologies with highly different scattering angles are explored, namely annular dark-field (ADF) and annular bright-field (ABF) imaging. Both of these methods display fundamental imaging techniques.

Annular Dark-Field Imaging. Typically, electrons scattered at high angles exceeding the convergence angle of the probe constitute the primary signal source for ADF imaging, subsequently generating a convergent electron beam diffraction pattern at the detector. This technique is categorized depending on the range of the collection semi-angles: high-angle ADF (HAADF) with 90-200 mrad, medium-angle ADF (MAADF) with 50-100 mrad, and low-angle ADF (LAADF) with 25-60 mrad scattering angles. The numerical values representing the angle magnitude are determined by the dimensions of the detector's inner and outer radii, each corresponding to specific inner and outer semi-angles.

HAADF imaging detects diffusively scattered electrons at large angles, meaning they no longer adhere to coherent Bragg conditions but instead undergo incoherent Rutherford scattering.[132,133] Given that Rutherford scattering is roughly proportional to $Z^{1.7}$, where Z is the atomic mass of elements.[134] Since its sensitivity to the atomic mass of the specimen, this imaging technique facilitates the differentiation of individual atomic columns composed of specific elements to give insights into the chemical composition of the crystal.
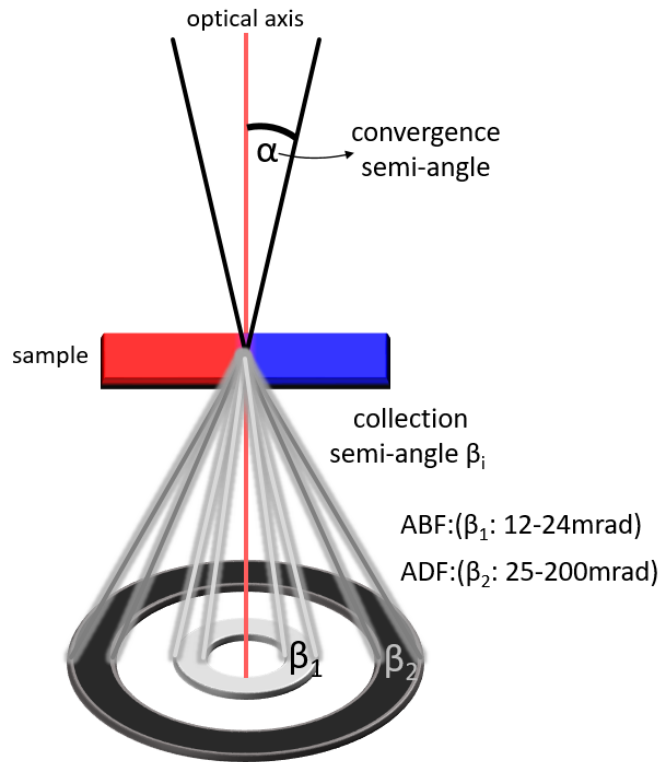
Figure 20: Illustration of the basics of ADF and ABF STEM imaging techniques with the convergence semi-angle α and the scattered electrons toward low-angles (β_1: 12-24 mrad) for ABF imaging and toward high-angles (β_2:25-200 mrad) for ADF imaging.

Annular Bright-Field Imaging. In ABF imaging coherent electrons with small scattering angles, i.e., 10-20 mrad, are detected by an annular detector. First, a phenomenon of paramount interest in ABF imaging is channeling, arising from the preferential alignment of incident electrons along a specific atomic column within a crystal lattice. This focusing of the electron beam in the forward-scattering direction results in a unique contrast mechanism, enabling the visualization of even light elements, such as oxygen, in the specimen with enhanced clarity and precision.[72,73,135] The contrast of ABF imaging is proportional to $Z^{\frac{1}{3}}$. Nevertheless, this correlation is not straightforward and fluctuates based on factors such as the detector range and the semiangle of the probe-forming aperture.[135]

Second, heavy elements will scatter the electron beam toward higher angles, outside of the ABF detector range, ultimately leading to a contrast mechanism visualizing both heavy and light atomic columns as dark spots. The non- or less-scattered electron beam between the atomic columns and in the vacuum will appear bright in the final image.

Electron Energy-Loss Spectroscopy. EELS serves as a powerful spectroscopic technique for assessing both the elemental composition and electronic state of materials by measuring the energy loss of the electron beam after interacting with the TEM specimen.[31,136,137] The EELS spectrum can be subdivided into three distinct regions, including the zero-loss (denoted as the zero-loss peak, ZLP at 0 eV), the low-loss (several meV to several tens of eV), and the high-loss regimes (including all element-specific edges due to intra- and interatomic excitations from core states to states above the Fermi level). Each of those regions offers unique insights and information regarding the material's properties and is depicted in Fig. 21.[138–140] In this thesis, the primary emphasis is directed toward the

investigation of high-loss regions, which can be directly correlated with the unoccupied density of states of correlated oxide materials. Using state-of-the-art instrumentation, such investigations can be conducted at the atomic scale, facilitating unprecedented characterizations of interfaces.[138,140]
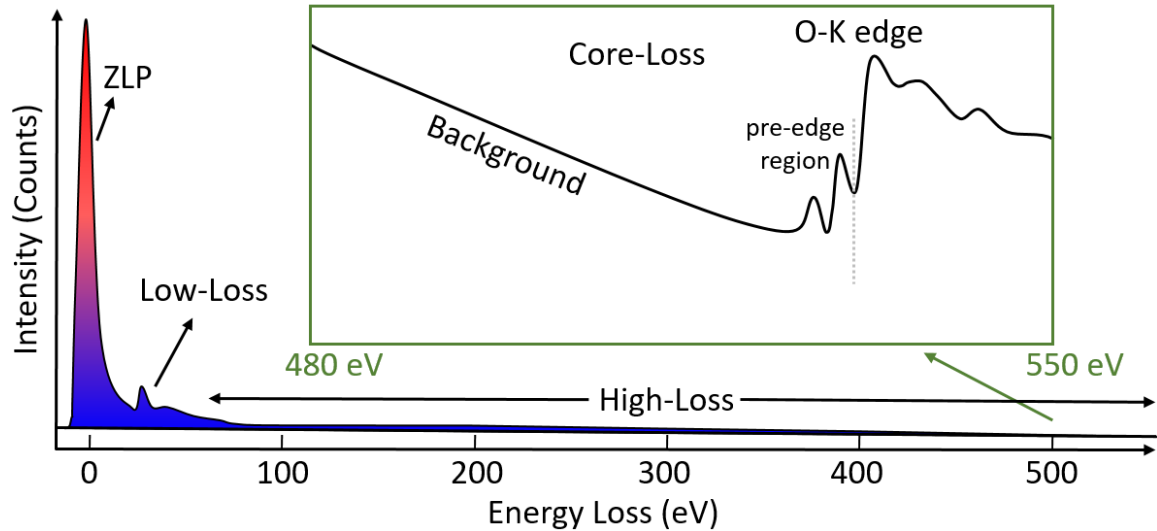
Figure 21: Illustrative diagram of a typical EEL-spectrum with three distinct regions: i) The zero-loss region with the zero-loss peak. ii) The low-loss region highlights plasmonic excitations. iii) The high-loss region with the core-loss edges with a prototypical O-K edge exemplification.

Energy-Loss Near-Edge Structure. Energy Loss Near Edge Structure (ELNES) not only facilitates the differentiation of elements within a sample but also provides a deeper understanding of the electronic state of the specimen.[140–142] In many cases, this allows for the deduction of structure-property relations. In particular, the spectral examination of $3d$ transition metals serves as a valuable approach to elucidate the oxidation states of the constituent atoms, as evidenced in prior research. In the framework of this thesis, mainly O-K, Mn-$L_{2,3}$, and Cu-$L_{2,3}$ edges are detected, analyzed, and interpreted in terms of the ELNES. In this context, the L_3/L_2 ratio has been calculated, which offers a reliable means of assessing the oxidation state of the respective element.[143] This method, based on the distinctive spectral features exhibited in the L_2 and L_3 edges, provides crucial insights into the electronic configuration of the element, allowing for a comprehensive characterization of its chemical state and contributing significantly to the depth of analysis in this research.[143]

Due to the strong correlation of transition metals with oxygen, the O-K edge displays a special role, in particular, its pre-edge region gives valuable insights into the electronic state of the density of states comprising Cu, or Mn 3d, and O 2p orbitals.[144] This unique ability to differentiate between different electronic states of the same element at the atomic scale underscores the significant advantage offered by EELS over all other existing spectroscopic techniques such as x-ray absorption spectroscopy or neutron scattering.

2 La$_2$CuO$_4$–Sr$_2$CuO$_{4-\delta}$ Superlattices

In the first part of this thesis, I would like to emphasize the importance of STEM-EELS investigations as a tool for atomic scale characterization of complex oxide interfaces. Here, I present a robust methodology to distinguish between certain quantum states, namely insulating, metallic, and superconducting states. The compounds La$_2$CuO$_4$ and Sr$_2$CuO$_{4-\delta}$ are used to create novel superconducting interfaces, which we study using STEM-EELS. These materials serve as essential components in the study of advanced interfacial phenomena, providing insight into the intricate properties of atomic-scale superconducting systems. The goal of this project underscores the efficacy of epitaxial engineering in controlling the transfer of spectral weight within a sample, particularly from the Upper Hubbard Band (UHB) to in-plane or out-of-plane hole states and subsequently back to the UHB. Using STEM-EELS analysis, we can visualize hole positions at the atomic scale within CuO planes, allowing us to distinguish between insulating, metallic, and superconducting states. This precise localization of holes not only enhances our understanding of material properties but also provides critical insight into the characterization of heteroepitaxial or intrinsic Josephson junctions. Importantly, this knowledge is particularly relevant in the context of oxide-based superconducting spintronics, motivating further exploration and applications in this cutting-edge field.

Contributions to this publication:
Nicolas Bonmassar conceived the project, wrote the initial manuscript, performed the growth of all samples by MBE using *in situ* RHEED, prepared the samples by tripod polishing, performed the TEM acquisition, performed the TEM data analysis, performed the sheet resistance and mutual inductance measurements, and performed the X-ray diffraction measurements. Georg Christiani and Gennady Logvenov assisted with sample growth. Ute Salzberger assisted with TEM sample preparation. Yi Wang assisted with TEM data evaluation. Y. Eren Suyolcu and Peter A. van Aken supervised this project and provided valuable input on data analysis. All co-authors revised the manuscript.

The following text and figures from this chapter are adopted from this publication: Bonmassar, N., Christiani, G., Salzberger, U., Wang, Y., Logvenov, G., Suyolcu, Y. E. and van Aken, P. A. Design and Differentiation of Quantum States at Subnanometer Scale in La$_2$CuO$_4$–Sr$_2$CuO$_{4-\delta}$ Superlattices. ACS Nano, 10.1021/acsnano.3c01422 (2023).[114]
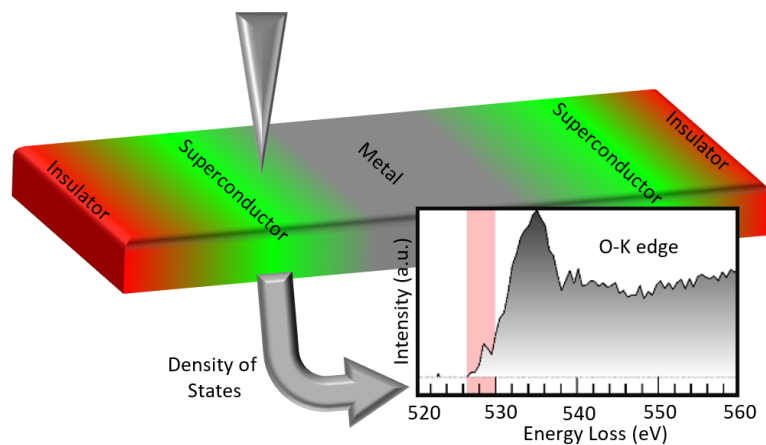
Graphical Abstract. We investigated the distribution of holes, oxygen, and Sr content to identify distinguishable quantum states. We achieved the capability to differentiate insulating, metallic, and superconducting layers at the atomic scale. This figure has been reproduced with permission from *Bonmassar et al.*[114]

2.1 Abstract

We present a study on the properties of superlattices made of ultrathin $Sr_2CuO_{4-\delta}$ layers sandwiched between La_2CuO_4 layers beyond the antiferromagnetic insulating nature of the individual layers of choice. Using molecular beam epitaxy, we synthesized these superlattices and observed superconductivity and metallicity at the interfaces. We probed the hole distribution to determine the discernible quantum states and found that the high-quality epitaxy, combined with mapping the electronic fine structure by electron energy-loss spectroscopy, allowed for the differentiation of insulating, metallic, and superconducting layers at the atomic-column scale. Our results demonstrate the possibility of exploring specific electronic properties at the subnanometer scale and highlight the potential of utilizing metastable $Sr_2CuO_{4-\delta}$ slabs.

2.2 Introduction

Complex oxide materials with intricate electronic phase diagrams hold immense potential for investigating exciting physical phenomena, such as giant magnetoresistance,[145,146] and high-temperature superconductivity.[147] La_2CuO_4 (LCO) serves as a model system for high-temperature superconductivity, transitioning from an antiferromagnetic insulator to a superconductor (SC) through hole[54,148–151] or electron doping.[152] The use of MBE enables the fabrication of high-quality oxide hetero-structures, allowing for the engineering of physical properties at interfaces.[9,41,153,154] For instance, in hetero-structures made of two non-superconducting LCO layers, i.e., undoped LCO and overdoped $La_{2-x}Sr_xCuO_4$ (LSCO), the intermixing of the cations changes the electronic state of the individual materials, resulting in the emergence of interfacial superconductivity.[46,55,155]

Characterizing the electronic states in superconducting cuprates is frequently accomplished using x-ray absorption spectroscopy (XAS)[156,157] and EELS[158,159] in conjunction with scanning transmission electron microscopy (STEM). The pre-peak of the O-K edge, which plays a key role in analyzing hole doping in superconductors,[158–160] is the focus of most studies. In the literature, various terminology has been proposed to describe the O-K edge pre-peak in LSCO. In our work, we will address this emerging O-K edge pre-peak as hole peak (HP). Chemical doping, such as Sr doping in LCO, shifts spectral weight from the upper Hubbard band (UHB) to the HP, thereby introducing holes into the system.[161–163] Polarization-dependent XAS provides information on orbital occupation through high energy resolution,[55,163,164] but with limited spatial resolution, which is inevitable for characterizing innovative applications like Josephson junctions.[165] EELS bridges this gap, offering atomic-scale characterization of orbital occupation, and the ability to quantify cations and anions, and their physical properties as a function of position by probing different phases.

In this work, we aimed to differentiate between metallic, insulating, and superconducting phases at the interface (IF), by probing the holes and atomic distribution. To achieve this, we designed a superlattice (SL) consisting of epitaxial ultra-thin tetragonal $Sr_2CuO_{4-\delta}$ (SCO) layers sandwiched between LCO layers, using an oxide MBE. In bulk, LCO crystallizes in a tetragonal K_2MgF_4-type structure, while Sr_2CuO_3 is orthorhombic and consists of 1D chains of CuO_4-planes.[164] By applying high oxygen pressure, the phase transition from orthorhombic Sr_2CuO_3 to the tetragonal SCO is induced.[165] We utilize ultra-thin SCO layers resulting in improved interface control when the SCO layers are sandwiched between LCO layers. This design simultaneously exhibits superconductivity, metallicity, and insulating phases and enables the analysis of holes and doping contents through

STEM EELS analysis of the O-K, Cu-$L_{2,3}$, La-$M_{4,5}$, and Sr-$L_{2,3}$ edges. The evolution of the O-K edge pre-peak reveals the transfer of spectral weight from the UHB to the HP, which drives superconductivity. The excitations of holes resulting in HPs, the presence of oxygen vacancies, and the Sr content can be directly probed in individual atomic layers, enabling the differentiation and characterization of quantum states at the atomic scale.

2.3 Methods

Oxide-MBE Growth
LCO-SCO bilayer systems consisting of four unit cells LCO and one unit cell SCO have been grown by atomic layer-by-layer oxide MBE for five times on a LSAO (001) substrates (CRYSTAL GmbH) using an MBE system of DCA Instruments. The surface of the SL is protected via an additional four unit cell thick LCO capping layer. The deposition conditions during the growth were $\approx 1 \cdot 10^{-5}$ Torr under oxidizing atmosphere consisting of ozone, radical oxygen and molecular oxygen, and 640°C pyrometer temperature. After the SL was grown, the sample was cooled in vacuum, from 210 °C to room temperature to avoid the formation of interstitial oxygen doping as described elsewhere.[153,154] *In situ* RHEED was performed during the growth to verify the quality of each deposited atomic-layer.

Transport measurements and X-Ray Diffraction (XRD)
Resistance (R) measurement in four-point-probe configuration (Van der Pauw) with alternative direct currents of ± 20 μA were carried out to verify superconductivity of the hetero-structure. Mutual inductance (MI) measurements of the real and imaginary part of the magnetic susceptibility in a two-coil configuration (parallel geometry) with an alternative current of 50 μA and a frequency of 1000 Hz was employed. R and MI vs temperature (T) measurements were controlled by a motorized custom-designed dipstick (T change rate < 0.1 K/s) and the temperature was varied from room temperature to 4 K (liquid helium). Out-of-plane XRD measurement were performed with a diffractometer equipped with a Cu-K$_{\alpha 1}$ source (Bruker D8 Cu-K$_{\alpha 1}$1 = 1.5406 Å to check the general macroscopic quality of the sample.

Scanning Transmission Electron Microscopy
The preparation of electron-transparent specimen included diamond cutting and tripod-wedge polishing. Afterwards, a precision ion polishing system (PIPS II, Model 695) equipped with a liquid nitrogen cooling stage using argon ions was employed for final thinning of all specimens with an estimated final thickness of 15 nm and all TEM specimens yield similar thicknesses. STEM analyses have been performed with a JEOL JEM-ARM200F STEM equipped with a cold-field emission gun, a probe Cs-corrector (DCOR, CEOS GmbH) and a Gatan GIF Quantum ERS electron energy-loss spectrometer equipped with a Gatan K2 direct electron-detection camera. EELS results and STEM images were collected at a convergence semi-angle of 22 mrad resulting in a probe size of 0.8 Å. For ADF imaging, the collection-angle range was 87-209 mrad. EELS data were acquired at a collection semi-angle of 87 mrad. A pixel dwell time of 7.4 ms and an energy dispersion of 0.5 eV/channel (resulting in an energy resolution of 1 eV) were used for all EELS experiments. Principle component analyses (PCA) was applied to reduce the noise in the spectrum images (SI).[166] After PCA including ten components, multiple linear least square (MLLS) fitting was performed on the PCA treated SIs as described elsewhere.[167] For the elemental profiles, ELNES spectra and the 2D projected line scans, MLLS fitting and horizontal pixel summation were performed on raw data with no further treatment,

respectively.

2.4 Tuned Spectral Weight Transfer from UHB to HP
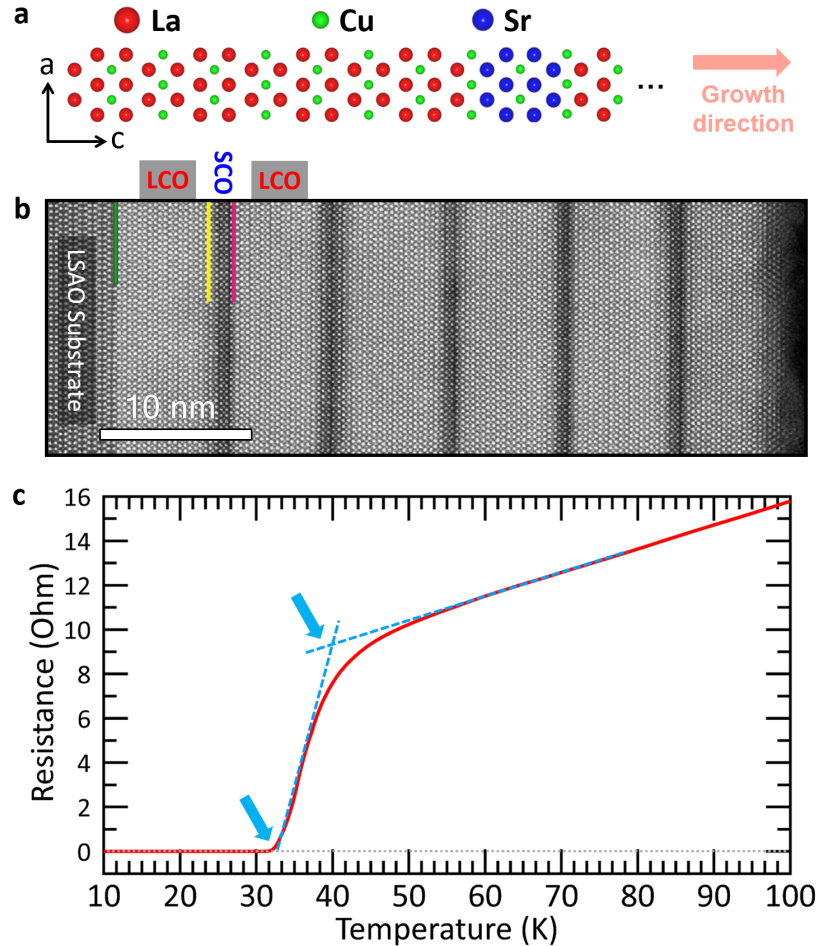
Figure 22: Atomically resolved STEM imaging and transport properties of the LCO-SCO SL. (a) Structural illustration of one of the five LCO-SCO blocks. Red, blue, and green represent La, Cu, and Sr, respectively. (b) ADF overview image depicting the defect-free SL consisting of a repetitive bilayer system, namely eight half-unit cells LCO and two half-unit cells SCO, as well as an LCO protection layer, grown on an LSAO substrate with (001) orientation along the [001] axis. The green line in panel (b) indicates the interface to the substrate. The yellow and pink arrows point out the LCO-SCO and SCO-LCO interfaces IF1 and IF2, respectively. (c) Resistance versus temperature (red) curve. The blue arrows point out the T_C onset and $T_{R=0}$ values. This figure has been reproduced with permission from *Bonmassar et al.*[114]

SLs composed of five repetitive LCO-SCO bilayers were grown by oxide MBE in a layer-by-layer regime and in situ monitored by reflection high-energy electron diffraction (RHEED). To ensure an oxygen-interstitial-free sample, all SLs were vacuum-annealed post-growth. The structural model of the building block, consisting of LCO and SCO, is illustrated in Figure 22a. A low-magnification annular dark field (ADF) image, shown in Figure 221b, provides a comprehensive overview of the SL grown on a LaSrAlO$_4$ (001) substrate and displays a high-quality, perfect epitaxial structure without any undesired defects (see also
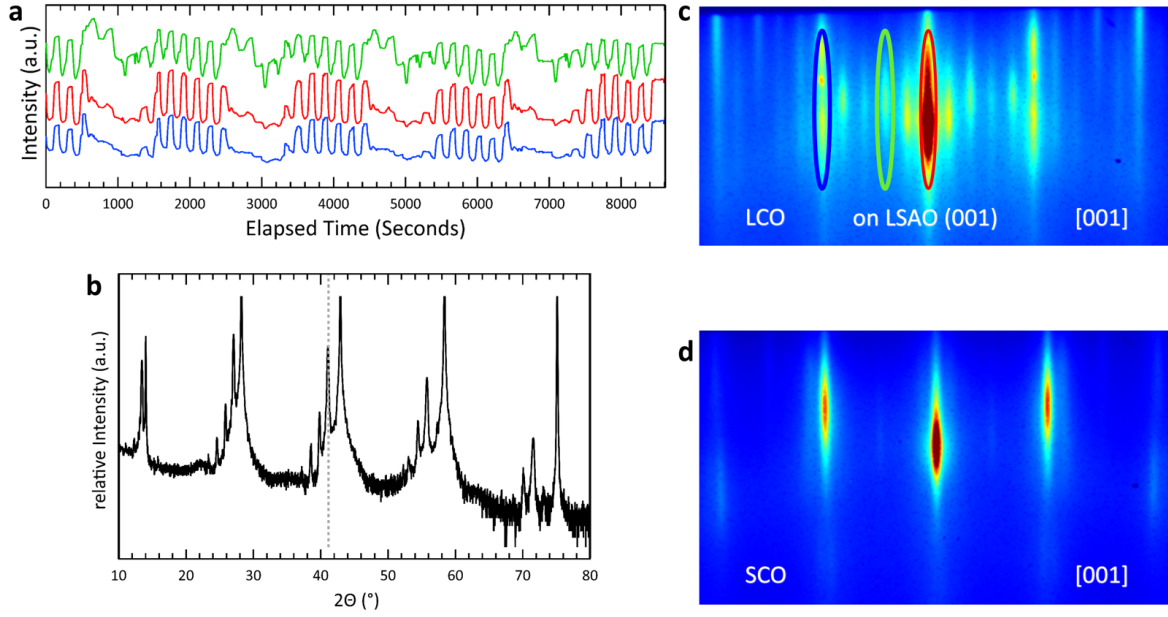
Figure 23: *In situ* **and macroscopic structural characterizations.** (a) Intensity oscillations of Bragg reflections (see (c) blue, red, and green ellipse) during the growth. (b) Out-of-plane x-ray diffraction of the superlattice with Cu-Kα source. (c) LCO and (d) SCO RHEED image, obtained during the growth. This figure has been reproduced with permission from *Bonmassar et al.*[114]

Figure 23). The LCO layers appear brighter compared to the SCO layers due to the difference in atomic weight between La and Sr (Z-contrast),[168] while minor contrast variations are observed in the SCO layers. The chemical potential and crystallographic differences between orthorhombic Sr$_2$CuO$_3$ and tetragonal LCO can result in La/Sr intermixing[169] as further discussed in the next section. The transport properties of this heterostructure were measured with resistance yielding a T_C, Onset of 40 K and a $T_{R=0}$ of 32 K shown in Figure 22, for mutual inductance measurement see Figure 24.
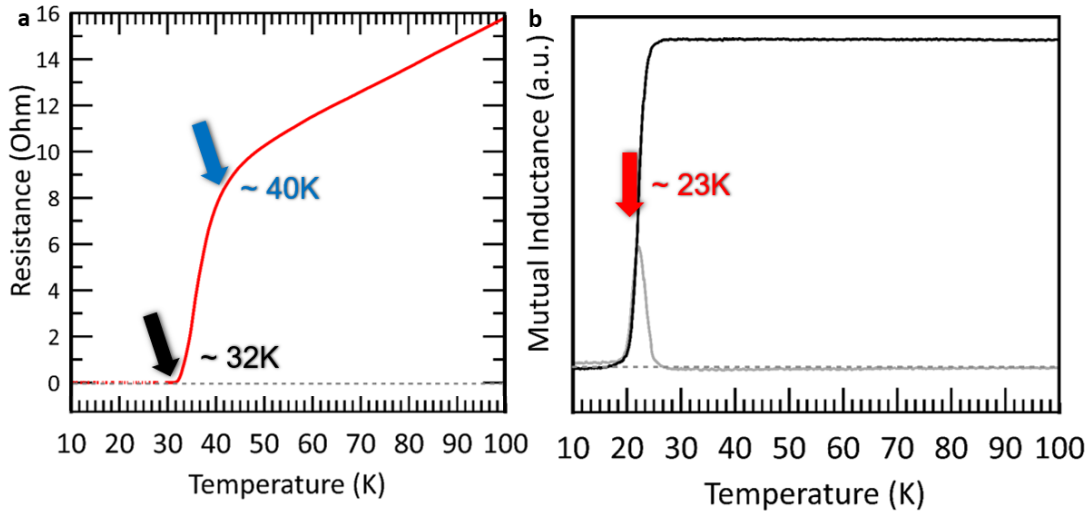
Figure 24: Transport measurements. (a) Resistance and (b) mutual inductance vs. temperature measurements. The blue and black arrows in panel (a) depict the onset and the R=0 temperatures from R vs. T, respectively. The red arrow in panel (b) highlights the maximum of the imaginary part (grey line) and the inflection point of the real part (black curve). This figure has been reproduced with permission from *Bonmassar et al.*[114]
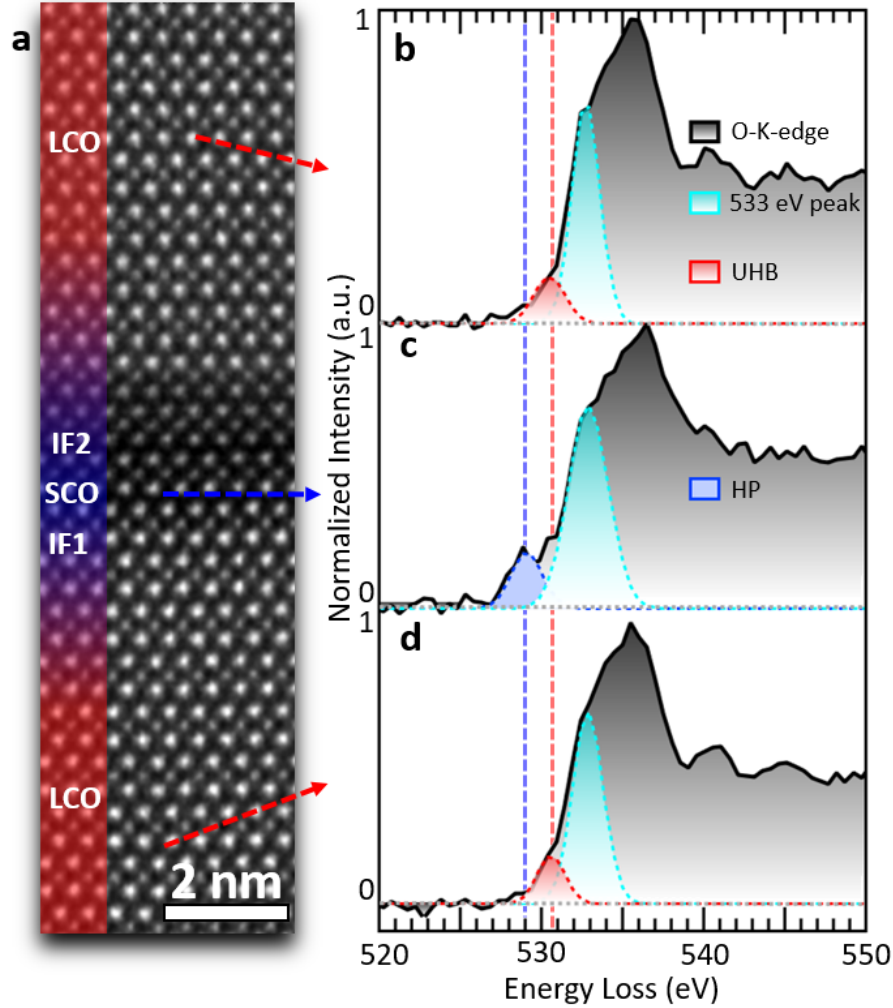
Figure 25: Spectral weight transfer from the UHB to HP. (a) ADF overview of the three regions separated by two interfaces (IF 1 and IF 2) highlighting areas with no Sr (red) and high Sr content (blue). (b), (c), and (d) Gaussian fits with energy constraints for the HP (blue) at 529 eV, the UHB (red) at 530 eV, and a peak at 533 eV (turquoise). Spectra have been obtained from the top, middle, and bottom areas away from the interface, as indicated by the red and blue arrows. This figure has been reproduced with permission from *Bonmassar et al.*[114]

Figure 25a presents a high-magnification image capturing the two key interfaces (IF), i.e., IF1 for LCO-SCO and IF2 for SCO-LCO. Our aim was to shed light on the transfer of spectral weight from the insulating LCO layers (UHB) to the hole-containing superconducting and metallic LSCO layers. By focusing on the pre-peaks of the O-K edge (Figure 25b-d), we were able to uncover insights into this complex process. In Figure 25a, the interfacial region is further analyzed by dividing it into three different areas. An LCO area (top, Fig. 25b) separated from the SCO layer (middle, Fig. 25c), and an LCO area succeeding the SCO layer (bottom, Fig. 25d). Using Gaussian fitting, we identified three distinct peaks, each with its own characteristics. The first peak (i) the HP at ~529 eV (blue) is situated at lower binding energies compared to (ii) the UHB peak at ~530 eV (red), and (iii) a shoulder of the main edge onset at 533.0 eV (turquoise). The results of this analysis are visually compelling and illustrate the efficiency of spectral weight transfer from the UHB to the HP, which is located at lower binding energies.[161,170,171] In subsequent analyses, we aim to further dissect the interfacial area and examine the evolution of holes, Sr- content, and oxygen vacancy formation at the atomic scale.

2.5 Probing the Interfaces: Insulating, Metallic, and Superconducting CuO Planes
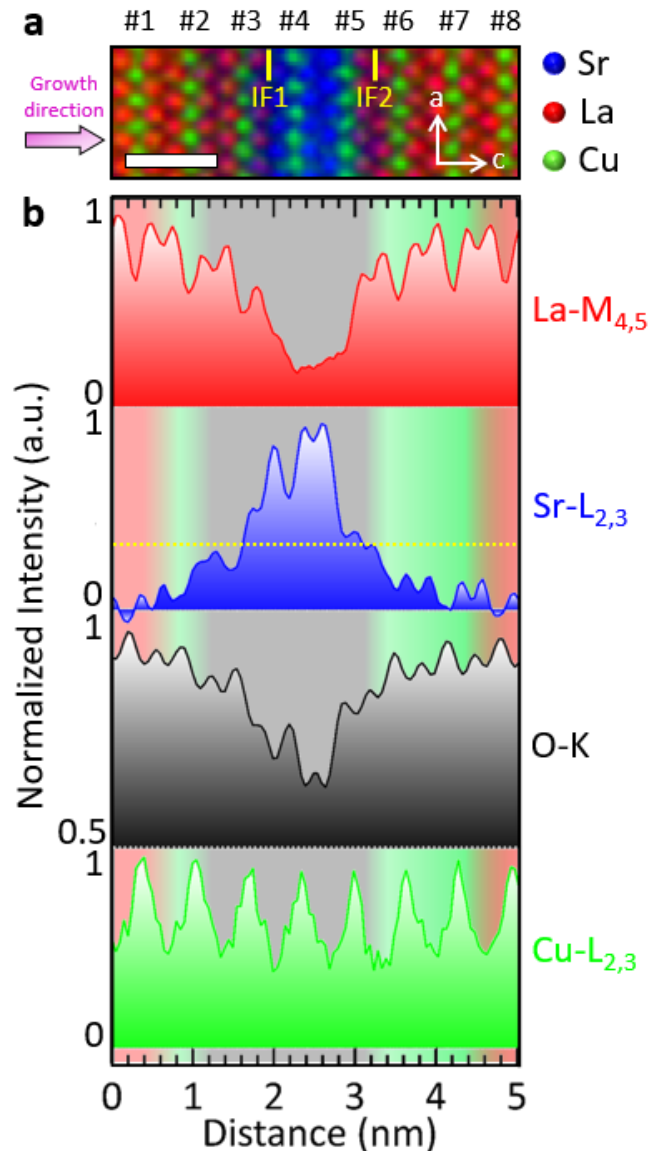
Figure 26: EELS spectrum imaging and corresponding elemental profiles across both interfaces, IF1 and IF2. (a) Color-coded RGB elemental map (La: red, Cu: green, and Sr: blue) of an interfacial region in the SL. The growth direction (purple arrow) was along the crystallographic c direction and interfaces IF1 and IF2 are depicted as yellow lines. (b) Projected –La, Sr, O, and Cu profiles of the whole area at and near the interfaces. The dashed yellow line marks the Sr content obtained from samples with La$_{1.65}$Sr$_{0.35}$CuO$_4$ layers, instead of La$_2$CuO$_4$ layers to differentiate between superconducting and metallic layers. The green background in (b) depicts the area, where a small Sr content is accompanied by a none detectable amount of oxygen vacancies, the grey background depicts the area, where there are many oxygen vacancies, and the red background highlights the two areas, where neither Sr nor oxygen vacancies could be detected. This figure has been reproduced with permission from *Bonmassar et al.*.[114]

We sought to uncover the precise electronic character of the layers in question by making an initial distinction of the corresponding layer positions and correlating O-K and Cu-$L_{2,3}$ edges. This effort is showcased in Figure 26a, where we present an atomically resolved 2D elemental mapping of the interfaces in detail.[167]
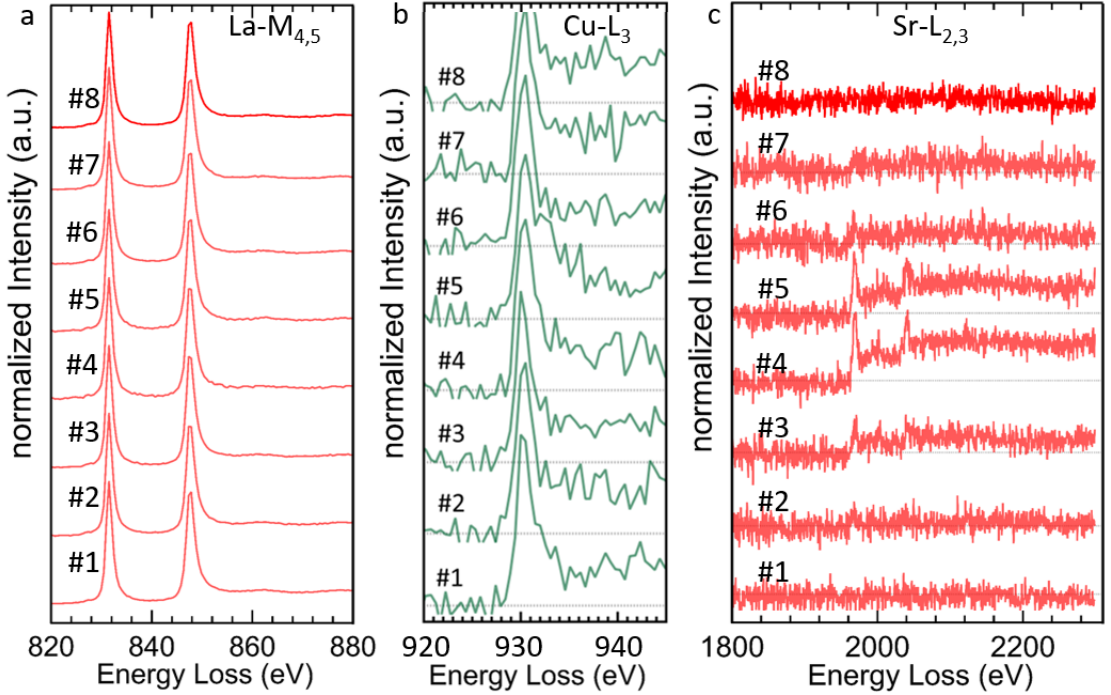
Figure 27: (a) La-$M_{4,5}$, (b) Cu-L_3 and (c) Sr-$L_{2,3}$ edges extracted from the same location as in Fig. 28c. This figure has been reproduced with permission from *Bonmassar et al.*[114]

The eight consecutive CuO planes (green) are numbered to guide the reader through the Sr-induced holes, with green denoting the CuO planes. The first and the last Cu octahedra (planes #1 and #8) showed no detectable amount of Sr as expected for an undoped LCO layer. Conversely, Cu positions #2, #6, and #7 revealed a small Sr content but no detectable oxygen vacancies. Note that the dashed yellow line in Figure 26b highlights a Sr content of x=0.35 and was obtained from EELS measurements of a SL consisting of La$_{1.65}$Sr$_{0.35}$CuO$_4$ and Sr$_2$CuO$_4$. Excitingly, three Cu octahedra with high Sr content (positions #3, #4, and #5) showed evidence of oxygen vacancies (Fig. 26b). With this chemical information about the elemental distribution at the interfaces in hand, we were able to correlate it with the electronic configuration regarding the hole distribution, as seen in Figure 28.

In Figure 28 a,b, the projections of the Cu-L_3 edge and the O-K pre-edge obtained from an EELS spectrum image are shown, with the latter integrated along the crystallographic [100] direction. As for the [001] direction, spatially resolved energy-loss maps are presented. Due to the overlap of the Cu-L_3 edge with the La-M_4 edge, the Cu-L_3 white lines are not used for fine structure analyses, however, are presented in the Figure 27b. In addition, the raw spectra of La-$M_{4,5}$ and Sr-$L_{2,3}$ have been added in Figure 27a,c.

While the Cu-L_3 edge highlights the position of the Cu columns for orientation, the O-K pre-edge region displays the in-plane (red spectra) and out-of-plane (blue spectra) orbital occupation as indicated in Fig. 28c. The first Cu plane #1 with no Sr content (see black profile in Fig. 26b) exhibits a shoulder indicating the UHB at 530 eV, but no holes are detected. At the second Cu position (#2), holes enter the in-plane and out-of-plane orbitals due to the presence of Sr without any detectable oxygen vacancies. With higher Sr concentrations, more holes are present, e.g., the HP increases in positions #3, #4, and

#5. Between Cu positions #5 and #6 a maximum of holes is depicted in the out-of-plane position, which has already been reported before in overdoped samples.[163] This increasing HP is accompanied by an increase in oxygen vacancies, as indicated by the oxygen profile in Figure 26c (black), resulting in CuO$_6$-octahedra that fulfill all requirements for metallicity, such as oxygen vacancies, high Sr content, and strong hole doping. In parallel to the second Cu position, the following two Cu positions (#6 and #7) exhibit conditions for superconductivity, including small Sr-content, holes, and no detectable oxygen vacancies. Finally, the last Cu plane (#8) shows no signs of Sr, no holes, and fully oxygenated species. Figure 28d illustrates the three distinct quantum states identified in our SL, including insulating phases (red), metallic (gray), and superconducting (green) areas.
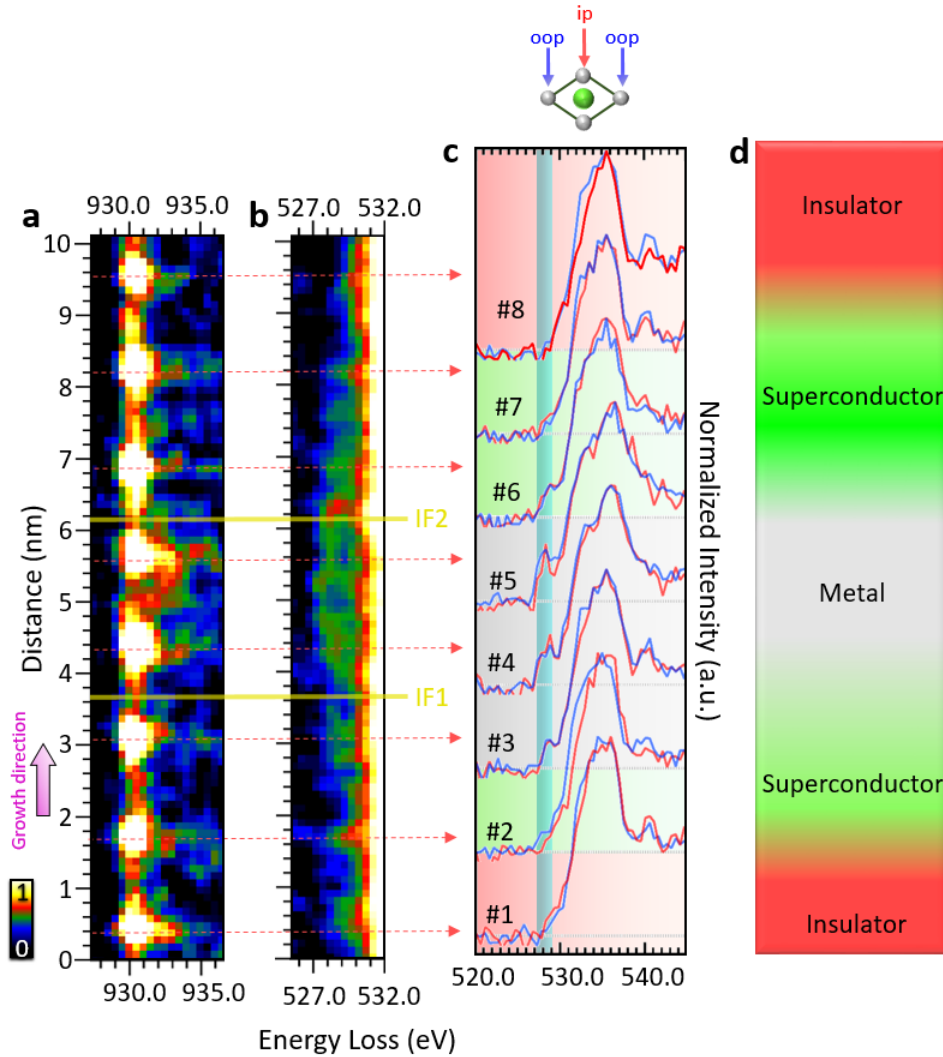
Figure 28: Differentiation between in-plane and out-of-plane orbital occupation via EELS spectrum imaging and O-K pre-edge analysis. Spatially resolved EELS maps of the (a) Cu-L_3 edge and (b) O-K edge. The intensity bar in panel (a) corresponds to both heat maps and interfaces IF1 and IF2 are depicted as yellow lines. (c) EEL Spectra were collected at different positions (1 to 8) and subdivided into out-of-plane (blue) and in-plane (red) orbitals. The shaded region (blue) at 527-529 eV highlights the pre-peak region of the O-K edge. The green background in (c) depicts the area where superconductivity occurs, the grey background depicts the area where metallicity arises, and the red background highlights the areas where an insulating phase ensues. (d) Schematic of the three distinct quantum states: insulating (red), superconducting (green), and metallic (grey) areas. This figure has been reproduced with permission from *Bonmassar et al.*[114]

2.6 Discussion

We report the successful synthesis of high-quality SCO–LCO SLs, in which distinct quantum states are generated at specific sub-lattices. Our findings demonstrate the delocalization of holes within the conducting layers, resulting in the establishment of three distinct quantum states: superconducting, metallic, and insulating phases. Furthermore, these three distinct states could be locally identified as insulating LCO layers and Sr-containing conducting LSCO layers.[113] The achievement of ultra-thin metallic tetragonal $Sr_2CuO_{4-\delta}$, instead of insulating orthorhombic Sr_2CuO_3 is attributed to the high ozone pressure during growth and the epitaxial compressive strain induced by the $LaSrAlO_4$ (001) substrate. Note that the SCO layer is metallic due to hole doping from additional oxygen in the structure, c.f. the additional sample presented in Figure 29.
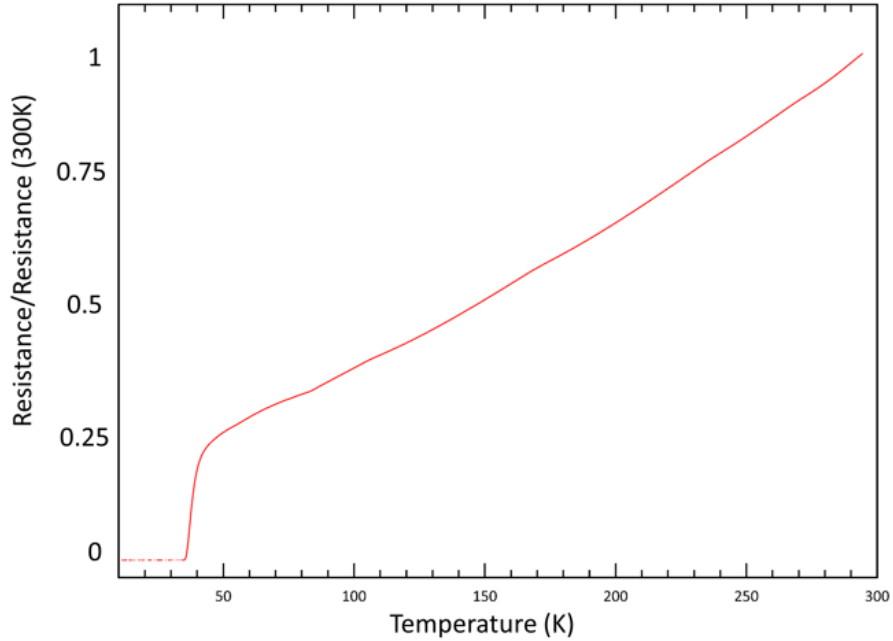
Figure 29: Sheet resistance normalized by the resistance value at 300K versus temperature of another superlattice with thicker SCO (two unit cells) and thinner LCO (three unit cells) layers. Here, the non-linear behavior for temperatures above T_C resembles a more Fermi liquid behavior. This figure has been reproduced with permission from *Bonmassar et al.*[114]

Based on the absence of superconductivity in strongly over-doped $La_{1.65}Sr_{0.35}CuO_{4-\delta}$ and SCO hetero-structures (as shown in Figure 30), the superconductivity in SCO-LCO SLs emerges from the interfacial region and not from the SCO layer. In contrast to the absence of holes in $Sr_2CuO_3$30, our SL, which shows the presence of holes (cf. Figs. 26 and 28), exhibits interfacial superconductivity with T_C, onset ≈ 40 K (cf. Fig. 22c).

In an earlier study, it was demonstrated that high-temperature superconductivity emerges in a single CuO plane31. Here, we show the presence of different superconducting CuO planes at the bottom and top interfaces between LCO-SCO-LCO heterostructures. The single bottom superconducting CuO plane shows a less pronounced pre-peak as compared to the top superconducting CuO planes, most likely due to a broader Sr distribution in the top layers. The broad superconducting transition is a result of every superconducting CuO plane exhibiting its own T_C, due to the varying distribution of Sr in the LCO matrix.[37,155] These results demonstrate the effective control of the hole distribution and the establishment of distinct quantum states in our SCO-LCO SLs, which represents a sig-

nificant advancement in the field of superconductivity. The results of our fitting analysis (Fig. 25) provide strong evidence of the atomic-scale differentiation of conducting phases in the synthesized SCO–LCO SL.
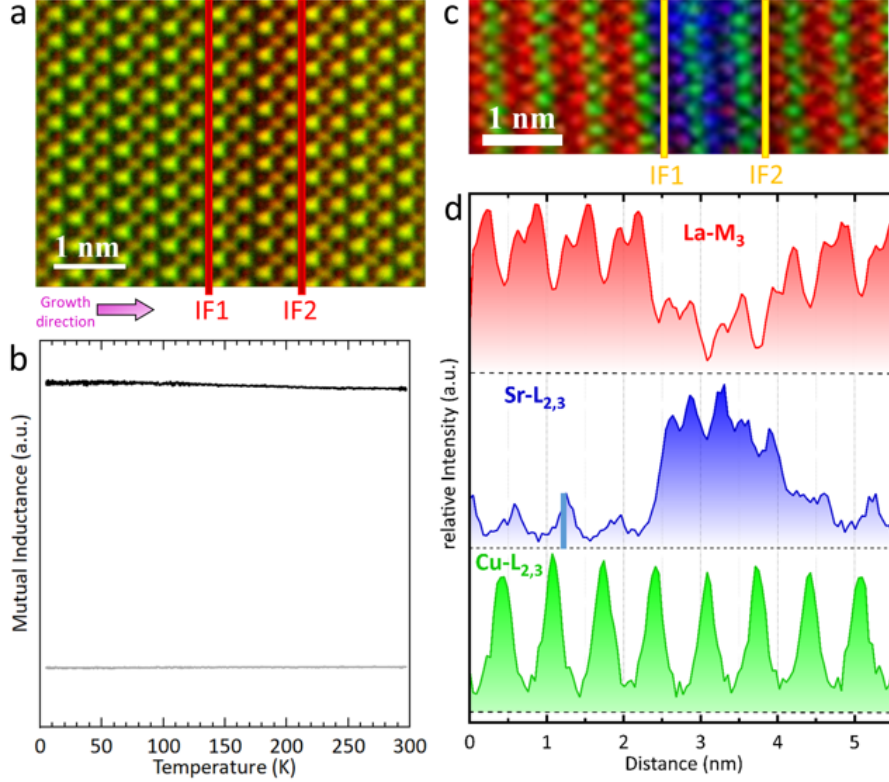
Figure 30: Additional sample composing of La$_{1.65}$Sr$_{0.35}$CuO4–Sr$_2$CuO$_{4-\delta}$ layers. (a) Overlay of HAADF and inverted annular bright-field (iABF) images highlighting both interfaces, IF1 and IF2. (b) Real (black) and imaginary (gray) parts of mutual inductance vs. temperature measurement. (c) EELS elemental map depicting Cu (green), La (red), and Sr (blue) positions in the superlattice. (d) Profiles obtained as in [100] direction integrated elemental distribution along the [001] direction. This figure has been reproduced with permission from *Bonmassar et al.*[114]

Specifically, we observe two phase-pure (i.e., undoped) LCO layers separated from a Sr-doped region, where holes are detected. Our findings reveal a transfer of spectral weight from the upper Hubbard band at 530 eV in the pure insulating LCO layer to the HP at 529 eV in Sr doped LCO, where holes are present. These observations enable us to differentiate between the metallic and superconducting phases based on the number of holes and the presence of oxygen vacancies.

Our study demonstrates the versatility of our epitaxial engineering approach in enabling the transfer of spectral weight from the UHB to in-plane or out-of-plane hole states and back to the UHB in the same sample. Figure 28c showcases the distinction between the superconducting area, indicated by a green background, which indicates holes, small amounts of Sr, and no detectable oxygen vacancies, while the insulating region, highlighted by a red background, lacks holes, Sr dopants, and oxygen vacancies. With the help of STEM-EELS analyses, we provide direct and atomic-scale visualization of the HPs through a plane-by-plane spatial mapping, with which we can distinguish between insulating (no holes), metallic (holes, oxygen vacancies, and high Sr content), and superconduct-

ing (holes, no detectable oxygen vacancies, and low Sr content) CuO-planes. Our results show the precise localization of holes in highly correlated systems with sub-nanometer resolution and provide a crucial tool for the characterization of hetero-epitaxial[37] or intrinsic Josephson junctions,[160,172,173] which are attracting growing interest in oxide-based superconducting spintronics.

3 La$_{1.84}$Sr$_{0.16}$CuO$_4$–Sr$_{2-x}$La$_x$MnO$_4$ Superlattices

Drawing from the outcomes delineated in the preceding section, wherein the intermixing of Sr and La atoms at the interface drives the observation of high-T_C superconductivity, the focus in this section lies in elucidating the pivotal role of interface sharpness. Here, the ultimate objective is to attain a state of minimal intermixing of two neighboring phases, wherein both materials retain their inherent properties without any discernible alterations. While SrLaMnO$_4$ and La$_{2-x}$Sr$_x$CuO$_4$ may exhibit structural compatibility at the epitaxial interface, achieving chemical perfection and the necessary absence of defects or precise apical oxygen spacing remains a challenge critical for properties such as superconductivity. The initial layers of superconducting materials on substrates are often referred to as "dead layers", lacking superconductivity. In oxide-based superconducting materials, where coherence lengths are smaller than in metallic counterparts, these considerations gain heightened importance. The imperative task lies in minimizing the chemical potential at the interface, a prerequisite for the realization of high-T_C oxide-based superconducting spintronics in the future. Thus, this study not only underscores the existing challenges, but also provides a roadmap for overcoming these obstacles, thus motivating the pursuit of advanced oxide-based superconducting spintronics.

Contributions to this publication:
Nicolas Bonmassar wrote the manuscript, performed the growth of all samples by MBE, sample preparation by tripod polishing, TEM imaging, TEM data analysis, sheet resistance measurements, mutual inductance measurements, and X-ray diffraction. Georg Christiani and Gennady Logvenov assisted with sample growth. Tobias Heil wrote the script for determining the position of oxygen in the ABF images. Y. Eren Suyolcu and Peter A. van Aken supervised this project and provided valuable input on data analysis. All co-authors revised the manuscript.

The following text and figures from this chapter are adopted from: Bonmassar, N., Christiani, G., Heil, T., Logvenov, G., Suyolcu, Y. E. and van Aken, P. A. Superconductivity at Interfaces in Cuprate-Manganite Superlattices. *Advanced Science*, 10.1002/advs.202301495 (2023).[91]
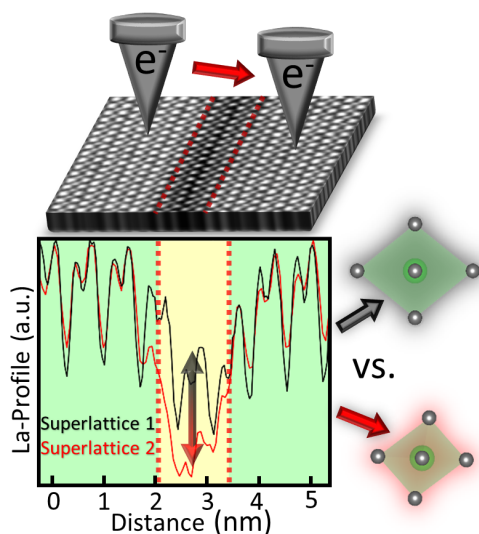
Graphical Abstract Differences in chemical potential lead to local structural distortions, cation intermixing, and the formation of parasitic phases. Therefore, even small distortions or non-stoichiometries can alter the physical properties at the nano-scale. This figure has been reproduced with permission from *Bonmassar et al.*[91]

3.1 Abstract

One of the unsolved problems for using high-T_C superconducting cuprates for spintronic applications is the short coherence lengths of Cooper pairs in oxides (a few Å), which requires atomically sharp and defect-free interfaces. Our research demonstrates the presence of high-T_C superconducting $La_{1.84}Sr_{0.16}CuO_4$ in direct proximity to $SrLaMnO_4$ and provides evidence for the sharpness of interfaces between the cuprate and the manganite layers at the atomic scale. These findings shed light on the impact of the chemical potential at the interface of distinct materials on highly sensitive physical properties such as superconductivity. Additionally, our results show the high stability of ultrathin layers from the same K_2NiF_4-type family, specifically one unit cell of $Sr_{2-x}La_xMnO_4$ and three unit cells of $La_{1.84}Sr_{0.16}CuO_4$. This work advances both the fundamental understanding of the proximity region between superconducting cuprates and manganite phases and the potential use of oxide-based materials in quantum computing.

SUPERCONDUCTING CUPRATE-MANGANITE SUPERLATTICES

Complex oxide superlattices consisting of superconducting cuprates and two chemically different insulating manganites show different critical temperatures. The chemical stability of the parent structure is key to enable high temperature superconductivity with structurally and chemically sharp interfaces between the respective ultra-thin layers. More details can be found in article number 2301495 by Nicolas Bonmassar, Y. Eren Suyolcu, and co-workers.

WILEY-VCH   www.advancedscience.com

Advanced Science Cover, DOI:10.1002/advs.202370138

3.2 Introduction

The study of cuprate-manganite interfaces has gained significant attention in recent years for its potential in oxide-based quantum computing,[39,56,174] and its impact on proximity-,[175] and exchange bias effects.[47] The goal of creating a superconducting π-qubit that is fully isolated from its surroundings is a topic of ongoing research.[60,176–180] However, a major obstacle in achieving this goal is the short coherence lengths ξ of Cooper pairs in oxide materials, which are only a few tens of Å and a few Å for $\xi_{in-plane}$ and $\xi_{out-of-plane}$, respectively.[173] Due to these extremely short coherence lengths, the control of superconductivity at the interface in direct proximity to the tunnel barrier is of utmost importance.[41,181]

It is well known that superconductors are highly susceptible to changes in their apical oxygen distances or small off-stoichiometries in their chemical distribution.[182,183] Even a thin layer of one half-unit cell of non-superconducting material at the top and the bottom interface can inhibit Josephson coupling between the two superconductors without considering the actual tunnel barrier. To minimize structural or chemical defects at the interface, choosing a tunnel barrier should not only be based on structural compatibility but also on the chemical potential difference between the tunnel barrier and the superconducting material.[55] It is also known that intermixing occurs at the interface between two materials with different elements.[61,184] A minimization of the difference in the chemical potential at the interface leads to less intermixing. Therefore, controlling the chemical potential difference at the interface also means controlling the physical properties.

In this work, we study the effect of minimizing the chemical potential between optimally doped superconducting $La_{1.84}Sr_{0.16}CuO_4$ (LSCO) and insulating $Sr_{2-x}La_xMnO_4$ phases (with either x = 0, SMO, or x = 1, LSMO) by doping Sr_2MnO_4 with La. To achieve high-quality interfaces, we use ozone-assisted MBE monitored by in situ RHEED.[9,40,45] This method allows us to control the growth of our samples and ensure that the interfaces are of the highest quality. For a thorough structural and chemical characterization of the interfaces at the atomic scale, we utilize several STEM techniques such as ABF imaging, HAADF imaging, EELS, and ELNES analyses. These techniques enable us to visualize and analyze the interfaces at the atomic level and gain a deep understanding of their structure and composition. Distortions of superconducting CuO_6- and insulating MnO_6-octahedra are a result of the Jahn-Teller effect and can be imaged using ABF.[155] As structural distortions can have a profound influence on the electronic configuration of the material, we show the unoccupied density of states (DOS) to highlight the complex orbital occupation in the interfacial CuO_6- and the MnO_6-octahedra.

Finally, we show how to control superconductivity in the proximity region to a tunnel barrier by manipulating the chemical potential at the interface. Our findings provide valuable insight into the relationship between chemical potential and superconductivity and can help further the development of oxide-based quantum computing.

3.3 Methods

Oxide-MBE Growth

LSCO-(L)SMO heterostructures consisting of three unit cells LSCO and one unit cell (L)SMO were grown by oxide MBE on a LSAO (001) substrates (CrysTec GmbH) using ozone-assisted-MBE (DCA Instruments). The deposition conditions during the growth were $\approx 1 \cdot 10^{-5}$ Torr (under an oxidizing atmosphere consisting of ozone, radical- and

molecular oxygen) and 640 °C (pyrometer temperature). Each growth was monitored by in situ RHEED to assure for atomic layer-by-layer growth.

Transport Measurements and X-Ray Diffraction (XRD)
Resistance (R) measurements with alternative direct currents of ± 30 µA were carried out in four-point-probe configuration (Van der Pauw) to verify superconductivity of the superlattices. Mutual inductance (MI) measurements were employed in a two-coil configuration (parallel geometry) with an alternative current of 50 μA and a frequency of 1000 Hz. All temperature (T) dependent measurements were controlled by a motorized custom-designed dipstick (T change rate < 0.1 K/s) and the temperature was varied from room temperature to 5 K. Out-of-plane XRD measurements were performed to check the general macroscopic quality of the sample. The diffractometer was equipped with a Cu-K_α source (D8 Cu-$K_{\alpha 1}1$ = 1.5406 Å).

Scanning Transmission Electron Microscopy
Electron-transparent specimens were prepared by tripod-wedge polishing. A subsequent precision ion polishing system (PIPS II, Model 695) equipped with a liquid nitrogen filled cooling stage, to ensure for a safe sample preparation without severely damaging the sample, using Ar^+ ions thinned the sample down to < 20 nm thickness. All STEM analyses were performed using a JEOL JEM-ARM200F STEM equipped with a cold-field emission gun, a probe Cs-corrector (DCOR, CEOS GmbH) and a Gatan GIF Quantum ERS electron energy-loss spectrometer equipped with a Gatan K2 direct electron-detection camera. EELS and STEM results were collected at a convergence semi-angle of 22 mrad resulting in a probe size of 0.8 Å. For ADF imaging, the collection-angle range was 87–209 mrad. EELS data were acquired at a collection semi-angle of 87 mrad. A pixel dwell time of 3.7 ms and an energy dispersion of 0.5 eV/channel (resulting in an energy resolution of < 1 eV) was used for the EELS elemental mapping and profiles, whereas for the Mn-L_3/L_2 ratio determination a dispersion of 0.25 eV/channel was used (resulting in an energy resolution of ≈ 0.5 eV). Principle component analyses (PCA) were applied to reduce the noise for the color-coded RGB maps in 34a,c and 40a. After PCA utilizing ten components, multiple linear least square (MLLS) fittings were performed on the PCA treated SIs as described elsewhere.[167] The elemental profiles and all ELNES spectra with their subsequent analyses regarding the Mn-L_3/L_2 ratios were extracted from raw data.

3.4 Overview of the As-Grown Samples

Here, we present SLs of ultrathin superconducting and insulating layers with a total thickness of ≈ 25 nm. We designed two different SLs, each consisting of a fourfold repetition of three unit cells LSCO and one unit cell SMO- or LSMO-layers, respectively (Figure 31a,b and Figure 32). An overview of the high-quality SL with alternating LSCO and LSMO layers is shown in the HAADF image in Figure 31b and similar results are presented in Figure 33 for the SL with SMO layers. The image shows an alternating pattern of thick bright LSCO layers and thinner dark LSMO layers with atomic resolution, starting from the substrate (red bar). The black profile on the left in Figure 31b highlights the HAADF intensity along the SL. The topmost unit cell of the LSCO layer at the surface was affected by environmental influences like moisture and is observed as a damaged layer on top of the heterostructure. To preserve the continuity of the interfaces, the last three unit cells of LSCO on top of the SL are deposited as a protective layer. In addition, the RHEED pattern in Figure 37 points out the sharpness of the interfaces as the 5x5 reconstruction could be retained after the deposition of the first unit cell LSCO after the LSMO layer.
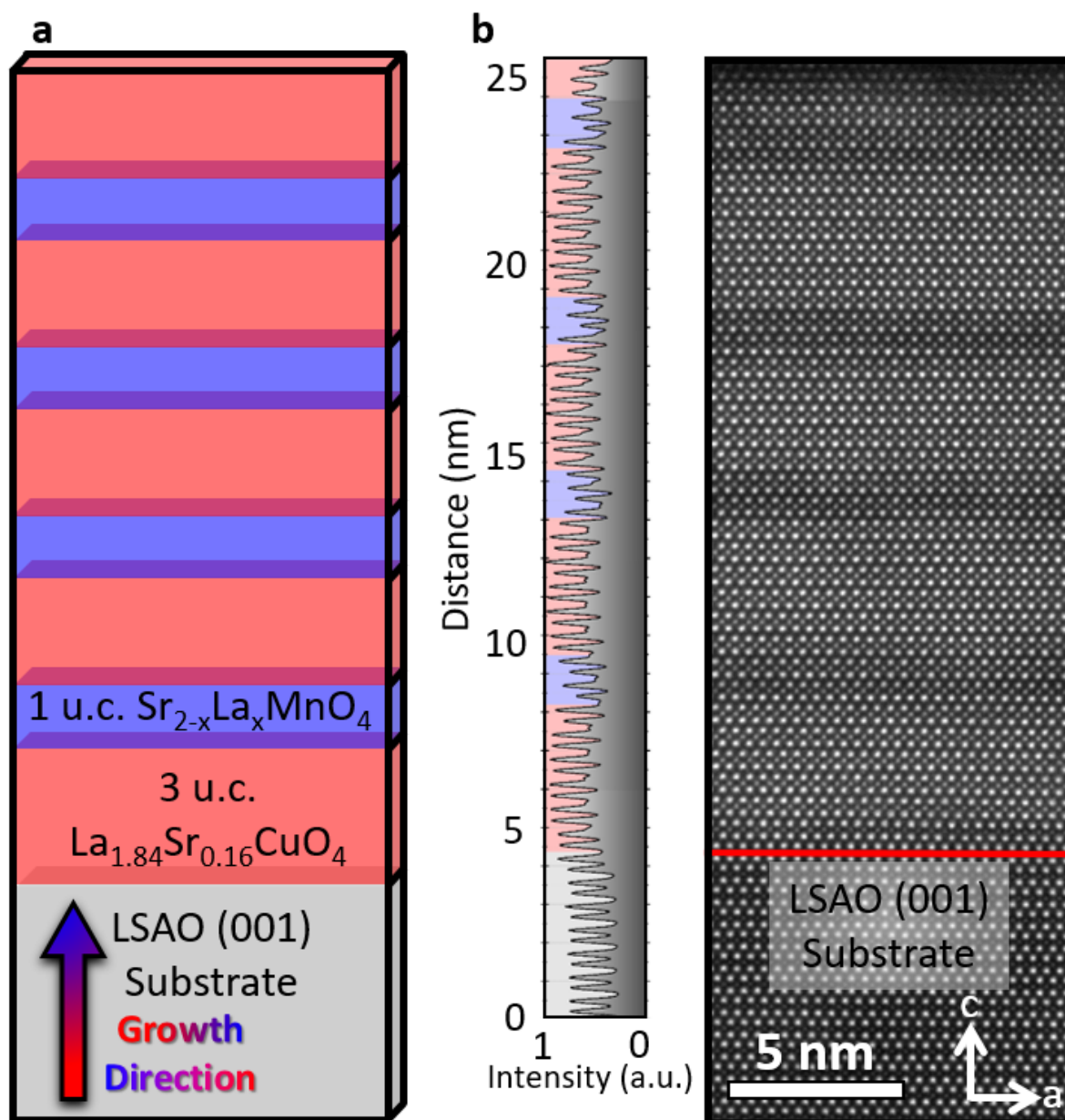
Figure 31: Overview (a) Schematic of the designed heterostructures, with x = 0 and x = 1. (b) Left: HAADF intensity profile integrated from the HAADF image. Red and blue backgrounds account for LSCO and LSMO layers, respectively. Right: HAADF overview image of the SL consisting of LSCO and LSMO. The red bar points out the interface from the substrate to the first LSCO layer. This figure has been reproduced with permission from *Bonmassar et al.*[91]
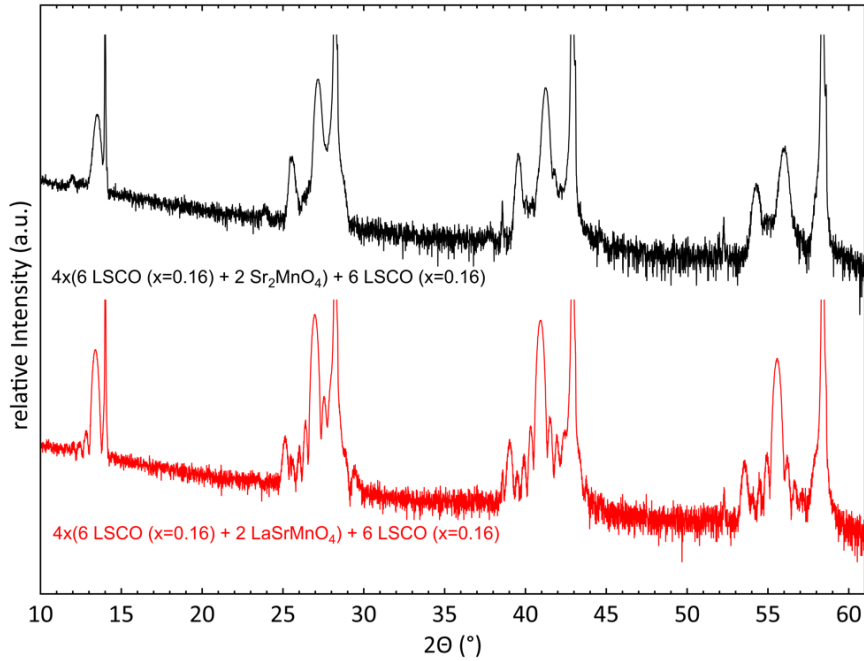
Figure 32: X-ray diffraction of both SLs. Top and bottom diffractogram corresponds to the SL with SMO and LSMO, respectively. This figure has been reproduced with permission from *Bonmassar et al.*[91]
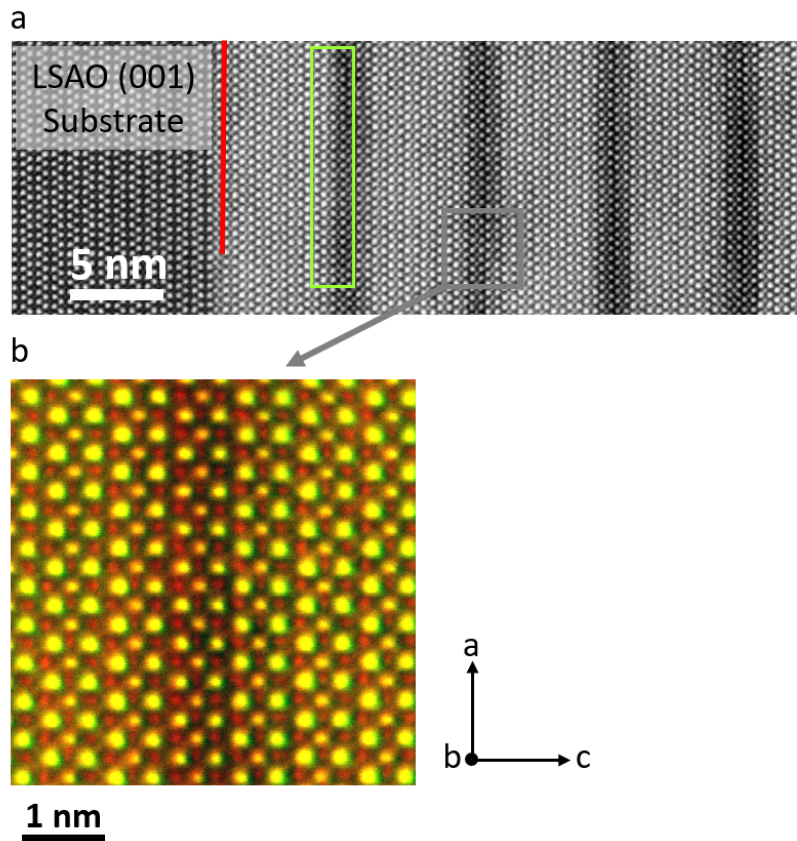
Figure 33: Overview of the superlattice with Sr$_2$MnO$_4$. (a) ADF overview image of the SL consisting of LSCO and SMO. The red bar points out the interface from the substrate to the first LSCO layer. The green box highlights the formation of a 113-type layer in the SMO area. (b) Overlay of high-angle annular dark field and inverted annular bright field images. This figure has been reproduced with permission from *Bonmassar et al.*[91]

39

3.5 Chemical Distribution of Elements

We investigate the two interfaces (IF1 and IF2 highlighted by white dashed lines in Figure 34a,c) of the cuprate-manganite systems using STEM combined with EELS for chemical mapping, which were denoised for a better guide to the eye for the reader (see Figure 35 for raw spectrum images).
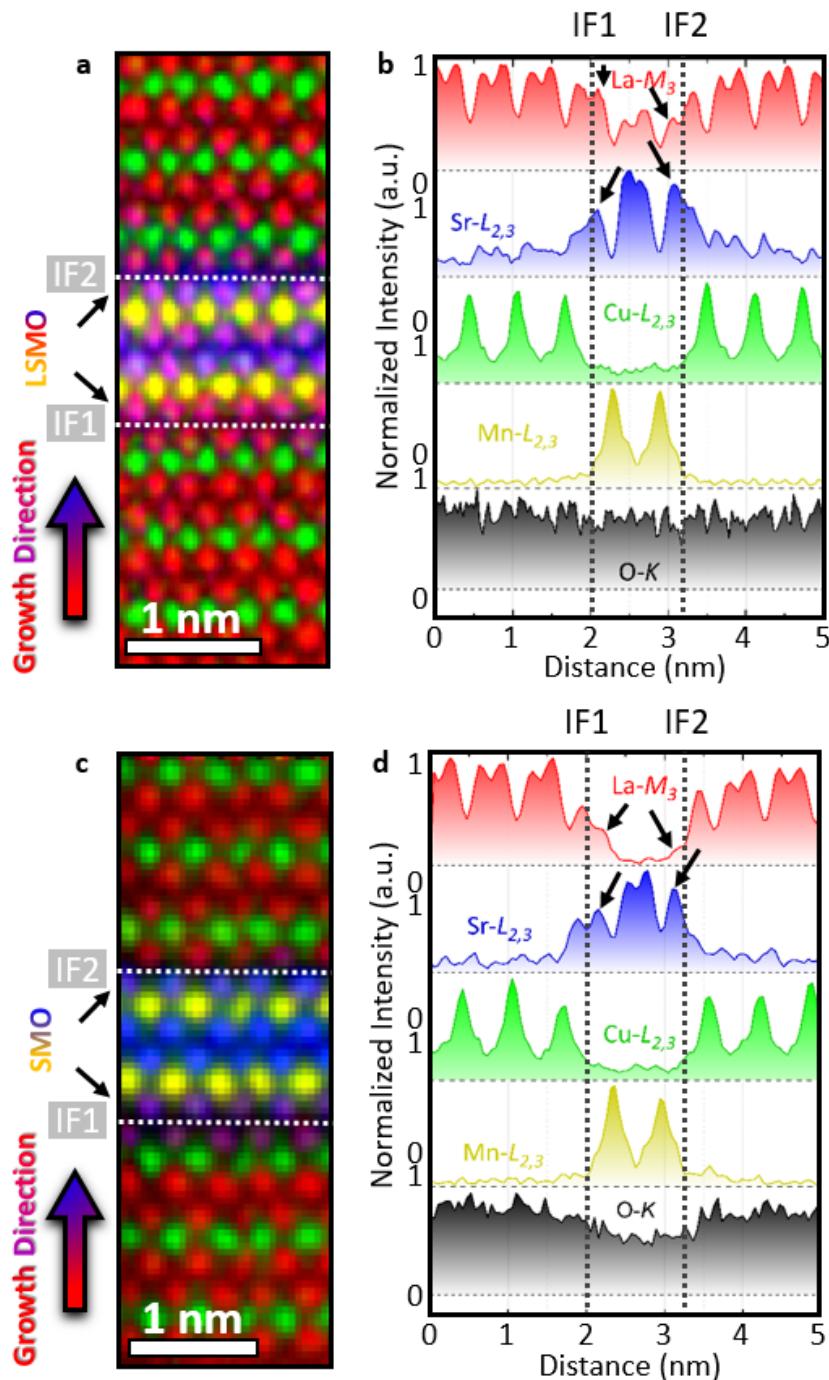
Figure 34: Chemical distribution of elements. (a), (c) EELS elemental mapping and (b), (d) EELS elemental profiles across two interfaces, IF1 and IF2, highlighted as dashed white lines for both superlattices, respectively. The small black arrows highlight differences in La and Sr content within one unit cell of LSMO (a) and SMO (b). The color code for the EELS mapping and the elemental profiles is red: La, blue: Sr, green: Cu, yellow: Mn, and black: O. This figure has been reproduced with permission from *Bonmassar et al.*[91]

The extracted profiles are obtained from raw data and show one to two atomic layer La/Sr intermixing at both sides of the interfaces (see black arrows in Figure 34b,d). Notably, no intermixing of Cu and Mn atoms was observed within the experimental sensitivity of our instruments, despite the thickness of only one unit cell of LSMO and SMO. Both samples show clear signs of Sr segregation (see black arrows below IF2) and more La is detected in the bottom part of the respective unit cell (see black arrows on top of IF1). This segregation is due to the atomic weight differences between La and Sr and has been discussed elsewhere.[155] Note that the SMO layer displays a stronger intermixing of Sr and La cations as compared to the LSMO layer. The effect of this unique type of intermixing on the oxidation state of the Mn atoms will be further explored later on using atomically-resolved fine-structure analyses of each MnO_6-octahedron. Finally, oxygen vacancies could be detected in the SMO layers but not in the LSMO layers.
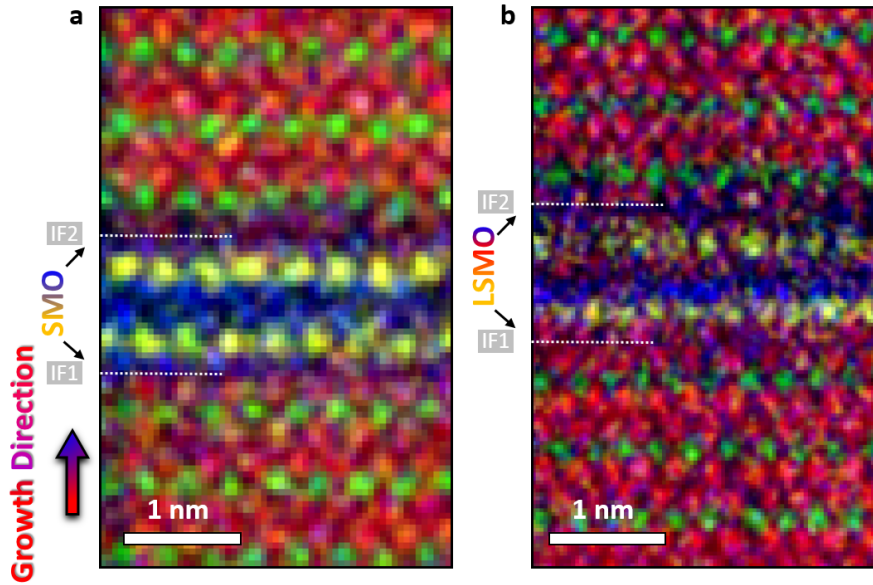
Figure 35: EELS elemental mapping obtained from raw data. (a) and (b) SLs with SMO and LSMO, respectively. The black arrows highlight the two interfaces (IF1 and IF2). This figure has been reproduced with permission from *Bonmassar et al.*[91]

3.6 Ultra-Thin Superconducting Films

Both SLs show high-T_C superconductivity, despite using ultrathin layers of LSCO as indicated by resistance (Figure 3a) and mutual inductance (Figure 36b) measurements. The resistance curves reach zero resistance at 31 K and 38 K for the sample with SMO and LSMO, respectively. The SL with LSMO shows a sharper transition. Mutual inductance measurements reach a full diamagnetic response signal at 25 K and 32 K in the SL with SMO and LSMO, respectively. The differences in critical temperatures between mutual inductance and resistance measurements are typically attributed to a percolation origin of superconductivity resulting from the proximity effect.[48,185] The ultrathin layers of LSCO used in this study are susceptible to exhibiting different critical temperatures due to small differences in the structural and/or electronic configuration,[42,186] such as CuO_6 octahedral tilts, elongations, or compressions. Furthermore, the ultrathin superconducting LSCO layers are sandwiched between non-superconducting manganites, which can lead to a buckling of the CuO_2 planes.[187] In addition, the in situ RHEED pattern indicates the presence of four streaks (Figure 37),[188] which depict a 5x5 super structured oxygen ordering,[45] typically associated with the presence of superconductivity in optimally doped

LSCO. Our findings allow us to combine the microscopic information of sharp LSCO structures with the macroscopic evidence for a clean and optimally doped LSCO unit cell in direct proximity to an insulating phase.
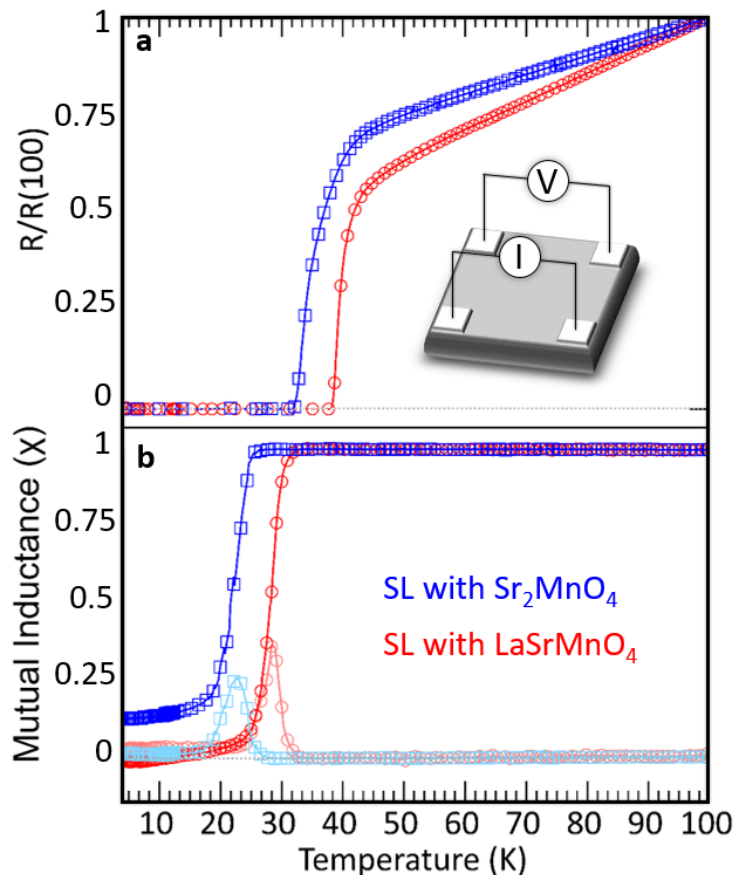
Figure 36: Physical properties of both samples. (a) Resistance and (b) mutual inductance vs. temperature curves in blue squares and red circles for the SL with SMO and LSMO, respectively. The inset in (a) shows the setup for the used four-point van der Pauw geometry. Imaginary parts of the mutual inductance measurements are depicted in lighter blue and lighter red colors, respectively. This figure has been reproduced with permission from *Bonmassar et al.*[91]
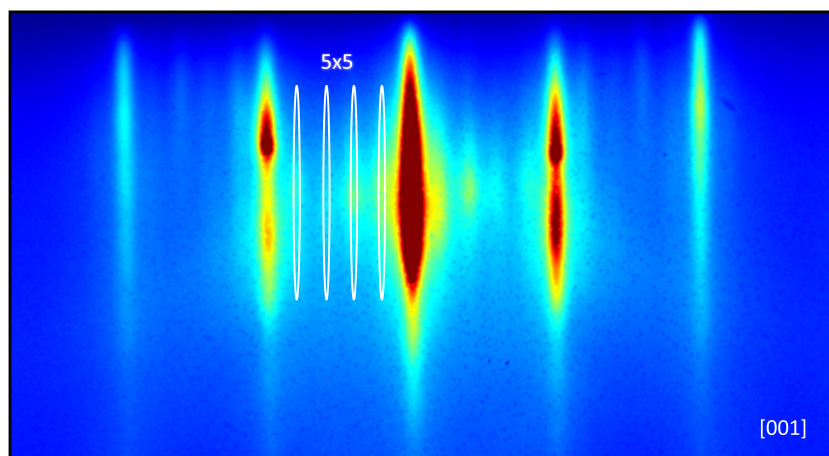
Figure 37: RHEED pattern of the first unit cell LSCO after the LSMO phase highlighting the 5x5 superstructure with four white ellipses. This figure has been reproduced with permission from *Bonmassar et al.*[91]

3.7 Apical and Basal Oxygen Distances

In a first step, we demonstrate the presence of typical anti-Jahn–Teller distorted LSCO layers in close proximity to the formally insulating manganite phase by measuring the oxygen–oxygen distances in both basal and apical directions.[93] We utilize ABF imaging to determine the basal and apical oxygen distances of the different CuO_6- or MnO_6-octahedra. Figure 38 shows overlays of inverted ABF (iABF) and HAADF images and their analyses.
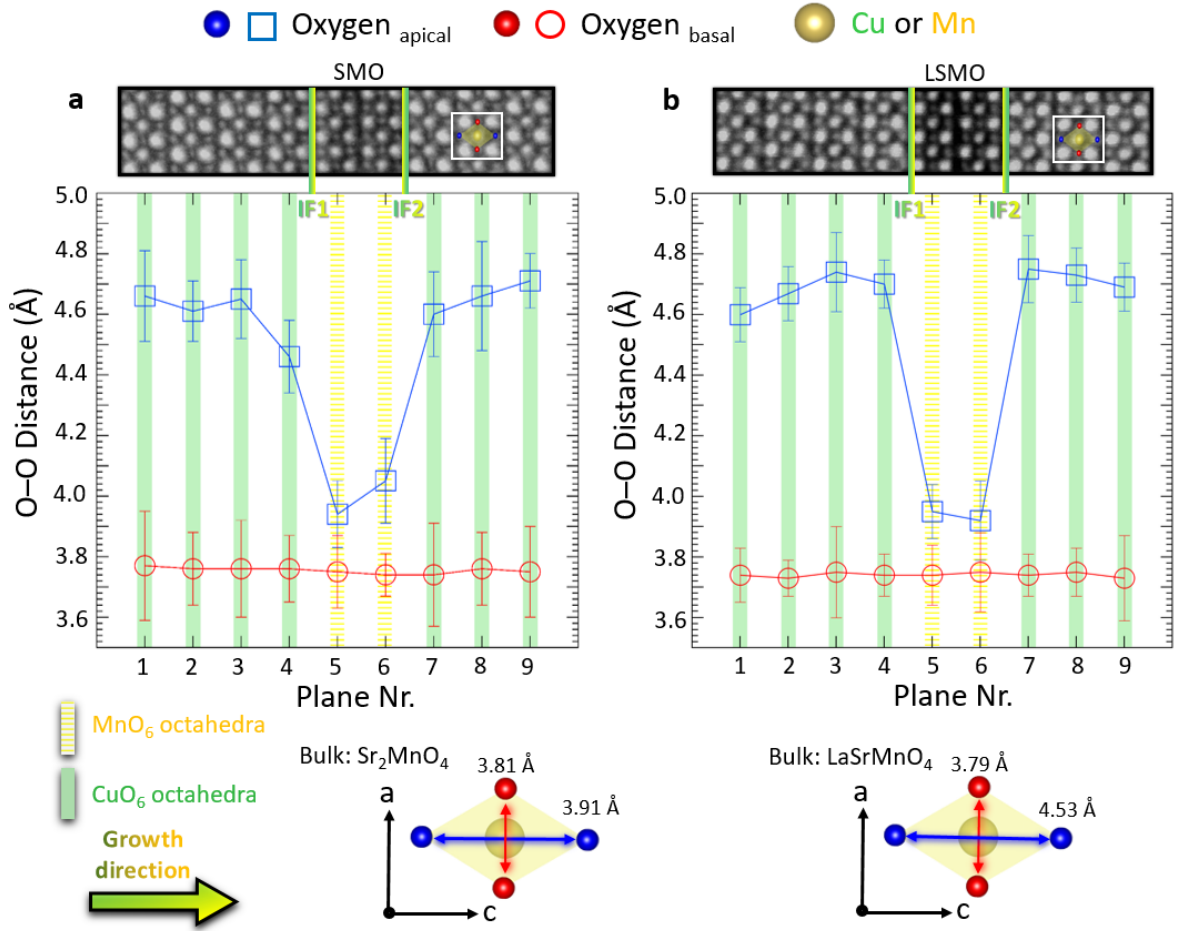
Figure 38: Apical and basal oxygen distances for the SL with SMO (a) and with LSMO (b). The top parts are overlays of HAADF and iABF images for simultaneous visualization of oxygen and A, and B site cation positions. The green arrow points out the growth direction and the two octahedra depict the apical and basal oxygen distances for SMO and LSMO bulk material.[189,190] Error bars arise from two times the standard deviation of atomic-column positions within the same plane. This figure has been reproduced with permission from *Bonmassar et al.*[91]

Additionally, we distinguish between different planes inside the CuO_6- (green bars) and MnO_6-octahedra (yellow bars). The basal oxygen distances (red circles) remain constant for the manganites and the cuprates in both samples (SMO in Figure 38a, LSMO in Figure 38b) and are the same as in the LSAO (001)-oriented substrate, i.e., 3.75 Å.[189] Due to the total thickness of only 25 nm, this holds true for all layers, even for the ones that are far away from the substrate. The apical oxygen distances (blue squares), show a significant decrease when transitioning from LSCO layers (4.6 Å and 4.75 Å) to manganite layers (4.0 Å and 3.9 Å). Furthermore, we observe a sharper decrease at interface

1 (IF1) and a sharper increase at interface 2 (IF2) of the CuO$_6$ apical oxygen distances in the SL with LSMO compared to the SL with SMO. Additionally, the apical oxygen distances of only 3.9 Å for the ultrathin LSMO layers are notably different from their bulk counterparts, which have a distance of 4.5 Å.[93] This indicates the presence of strongly compressed MnO$_6$-octahedra. These longitudinal compressions alter the electronic configuration of the materials by raising the $3\mathrm{d}z^2 - r^2$(out-of-plane) states, resulting in more occupied $3\mathrm{d}x^2 - y^2$ (in-plane) orbitals.[191] The same compression compared to the bulk material has been detected in HAADF results, c.f. Figure 39.
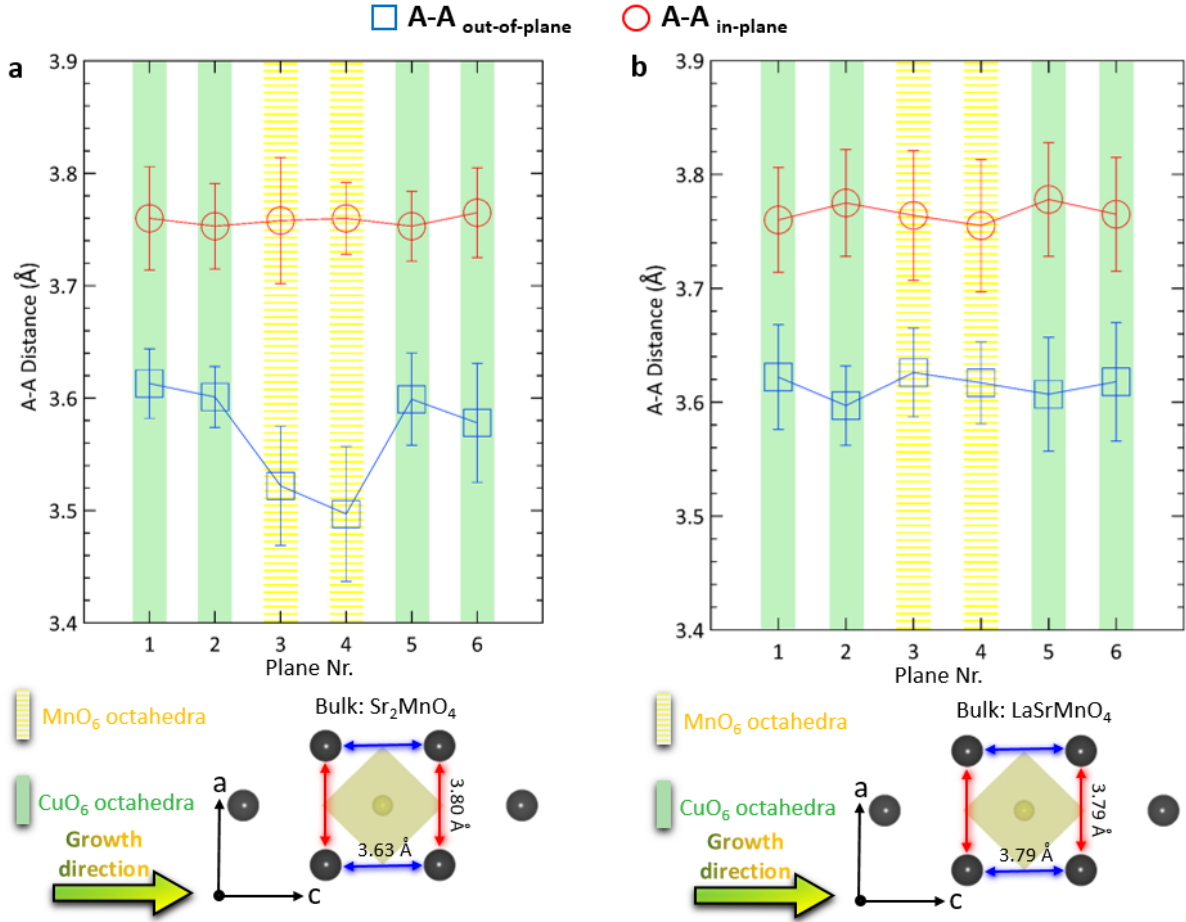
Figure 39: Out-of-plane (blue boxes) and in-plane (red circles) A-site cation distances obtained from HAADF images for the SL with SMO (a) and LSMO (b). The green arrow points out the growth direction and the red and blue arrows depict the out-of-plane and in-plane distances for SMO and LSMO bulk material. Error bars arise from two times the standard deviation of atomic-column positions within the same plane. This figure has been reproduced with permission from *Bonmassar et al.*[91]

In addition, a reduction of the cell volume has been detected in the SMO layer, which is in agreement with the detection of oxygen vacancies in this phase. Such strong effects can even result in completely different physical properties in the strained thin film compared to the unstrained bulk material.[169,192,193]

3.8 Electronic Configuration of the Interfaces

The impact of these structurally distorted MnO_6-octahedra on the electronic configuration of the manganite layers is characterized by utilizing ELNES analyses with atomic resolution (Figure 40).
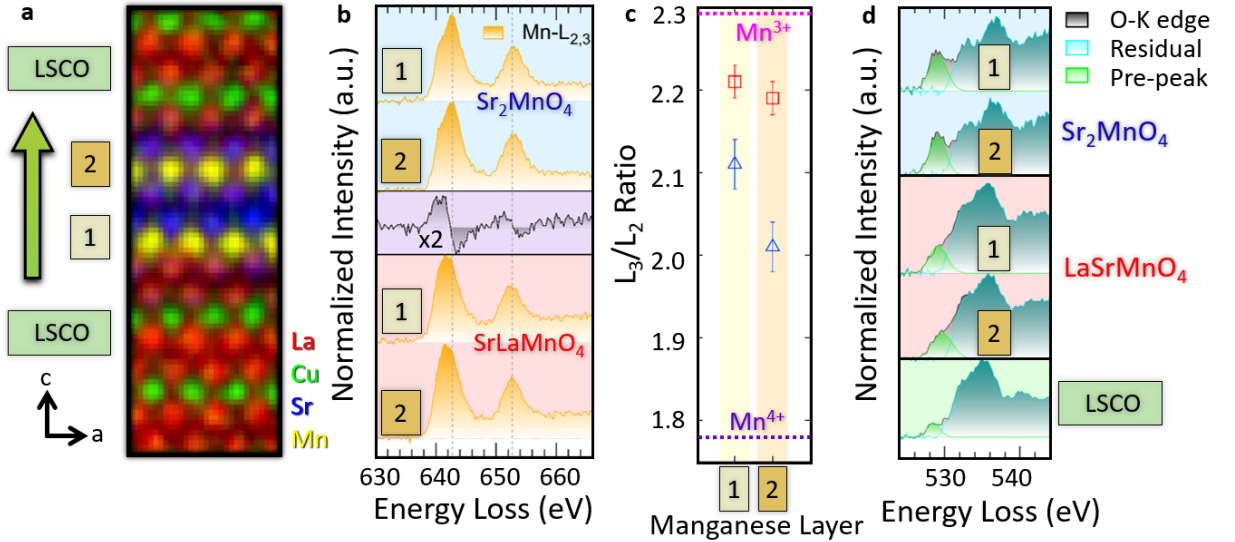
Figure 40: Electronic configuration of the one unit cell thick manganite layers in direct proximity to two superconducting LSCO layers. (a) EELS elemental mapping serves as a guide to the eye for the different regions where the following EEL spectra have been integrated. The green arrow points out the growth direction. (b) Mn-$L_{2,3}$ edges (orange) of the first and second monolayer of the respective unit cells for SMO (blue background) and for LSMO (red background). The spectrum with the purple background in (b) represents the difference spectrum between the sum of spectra 1 and 2 for LSMO and SMO, which highlights the earlier onset of the Mn-$L_{2,3}$ edge in LSMO compared to SMO. (c) Mn-$L_{2,3}$ ratios of the respective manganese layers with Mn^{3+} and Mn^{4+} reference ratios obtained from $LaMnO_3$ and $SrMnO_3$, respectively. (d) O-K edges (black) of the first and second monolayer of the respective unit cells SMO (blue background) and LSMO (red background), and the sum of the top and bottom O-K spectra for LSCO monolayers (green background). Each pre-peak is fitted with a Gaussian function (green) and the residual signal of the O-K edge is depicted in turquoise. This figure has been reproduced with permission from *Bonmassar et al.*[91]

To gain a deeper understanding of the individual unoccupied DOS of the MnO_6-octahedra, we divide the crystallographic unit cell of the $Sr_{2-x}La_xMnO_4$ phases into first and second monolayers as shown in Figure 40a and perform ELNES analyses on raw data. Then, we compare the individual Mn-$L_{2,3}$ edges of SMO (blue background, Figure 40b) with the Mn-$L_{2,3}$ edges of LSMO (red background, Figure 40b). A difference spectrum (Figure 40b, purple background, LSMO spectrum minus SMO spectrum from position 1) of the two manganite phases highlights the earlier onset of the Mn-L_3 edge in LSMO compared to SMO. The Mn-L_3/L_2 ratios are consistently lower for Mn atoms that are located in the second monolayer, indicating higher oxidation states of these Mn atoms. The Mn-L_3/L_2 ratios are calculated by the method of Tan *et al.* in Figure 40c.[194] The reference values for the Mn-L_3/L_2 ratios of Mn^{3+} and Mn^{4+} have been determined from bulk $SrMnO_3$ and $LaMnO_3$. A more pronounced difference in valence states is observed in SMO, whereas only a small difference in valence states is observed in LSMO. Finally, the fitted Gaussian functions in the pre-edge region of the O-K edges (Figure 40d) highlight a smaller pre-

peak in La-doped LSMO compared to SMO, indicating a lower Mn valence in the LSMO layer. This finding qualitatively confirms the results from the Mn-$L_{2,3}$ edge analyses, where a lower oxidation state of Mn atoms in LSMO is detected. However, an electronic differentiation of the two separate MnO$_6$-octahedra of the O-K pre-peak was not possible in contrast to the L_3/L_2 ratio determination, where small differences could be detected. Furthermore, the O-K edge pre-peak (mobile carrier peak) at 528.8 eV of the CuO$_6$-octahedra (green Gaussian fit with green background in Figure 40d) together with the high apical oxygen distance of 4.75Å (Figure 38b) indicates superconducting bottom and top CuO$_6$-octahedra that are separated by only one unit cell thick LSMO. Note that, the O-K edge pre-peak in the LSCO layer, which is induced by Sr-doping of a charge transfer insulator (La$_2$CuO$_4$) resulting in the introduction of mobile carriers, should not be confused with the O-K edge pre-peak of other antiferromagnetic insulators like bulk LSMO and bulk SMO that stay an insulator despite exhibiting a pre-peak in the O-K edge.[94]

3.9 Discussion

In summary, this is the first report about SLs consisting of only one unit cell thick SMO and LSMO layers between three unit cell thick superconducting LSCO layers. We deliberately focused on completely disentangled CuO$_6$ and MnO$_6$ octahedra, to avoid any interfacial hybridization of Cu 3d and Mn 3d orbitals, resulting in chemically sharp and superconducting interfaces. Notably, both LSMO and SMO deviate from their formal valence states of pure Mn^{3+} and Mn^{4+}, respectively. However, the deviation from the formal pure Mn^{3+} state for LSMO lies within the possible stoichiometry variations that can originate from the calibration of metal fluxes ($\approx$ 5% off stoichiometric) prior to the MBE growth. The deviation from the formally pure Mn^{4+} in the SMO layer is also due to the formation of oxygen vacancies in this phase, thereby lowering the Mn valence to a mixed Mn^{4+}/Mn^{3+} state.

On top of that, both manganite layers show clear signs of intermixing with neighboring La cations that ultimately alter the oxidation state of the manganese atoms. A stronger effect of the asymmetric cationic distribution on the Mn valence could be detected in the SMO layer compared to the LSMO layer (c.f. Figure 34b,d and Figure 40c). We attribute this finding specifically to the higher chemical potential between LSCO and SMO as compared to the chemical potential between LSCO and LSMO. Additionally, a 113-type parasitic phase can be detected in the SL consisting of SMO as indicated in Fig. 33a. These differences between the intermixed SMO phase and the more stable LSMO phase indicate the importance of the chemical potential between the two phases on both sides of the interface. The top and the bottom LSCO layers in direct proximity to LSMO are less affected regarding their apical oxygen distances and Sr content as compared to the LSCO layers next to SMO. Differences in Sr/La intermixing that directly influence the apical oxygen distances and defect formation (parasitic 113-type phase in SL with SMO) account for the higher T_C in both resistance and mutual inductance measurements of the SL with La-doped LSMO.

Structurally, most materials with similar crystallographic a and b axes will match perfectly at the interface when epitaxially grown. However, this does not guarantee chemical perfectness, the absence of defects, or the apical oxygen distances required for certain physical properties such as superconductivity. In fact, the first layers of superconducting materials on top of the substrate or layered structures are often referred to as "dead layers" due to the absence of superconductivity in these layers.[42] This is particularly important for oxide-based superconducting materials, as the coherence lengths of Cooper pairs in

oxide materials are smaller than in superconducting metals. Therefore, it is crucial to minimize the chemical potential at the interface for the realization of future high-T_C superconducting oxide-based spintronic.

4 Bi-Directional Growth of Thin Films: Unlocking Anisotropic Ferromagnetism and Superconductivity

In this section, I present an advanced growth model that enables a bi-directional growth of thin films. Upon growing on offcut substrates, one gains an additional degree of freedom regarding the growth direction, effectively allowing for an atomic terrace-by-terrace type of growth along the in-plane and out-of-plane direction Exciting possibilities open up within the groundbreaking bi-directional growth model that holds the key to the design of novel quantum materials. Based on the insights gained in the previous sections, the combination of state-of-the-art growth methods such as MBE and advanced characterization techniques such as STEM-EELS has led to this discovery. This advance opens new frontiers in the search for innovative materials with unprecedented functionalities and potential uses in industry and fundamental science including in-plane Josephson junctions, magnetic tunnel junctions, anisotropic colossal magnetoresistance effects, or new epitaxial designs such as the design of Peltier element/high-T_C superconductor heterostructures.

Contributions to this publication:
Nicolas Bonmassar conceived the project, wrote the initial manuscript, performed the growth of all samples by MBE using *in situ* RHEED, prepared the samples by tripod polishing, performed the TEM acquisition, performed the TEM data analysis, performed the XRD measurements, performed the resistance measurements on the devices, and performed the superconducting quantum interference device measurements. Georg Christiani and Gennady Logvenov assisted with sample growth. Maximilian Brucker performed atomic force microscopy. Y. Eren Suyolcu and Peter A. van Aken supervised this project and provided valuable input on data analysis. All co-authors revised the manuscript.

The following text and figures from this chapter are adopted from: Bonmassar, N., Christiani, G., Brucker, M., Logvenov, G., Suyolcu, Y. E. and van Aken, P. A. Bi-Directional Growth of Thin Films: Unlocking Anisotropic Ferromagnetism and Superconductivity. Adv. Funct. Mater., 10.1002/adfm.202314698 (2024).[195]
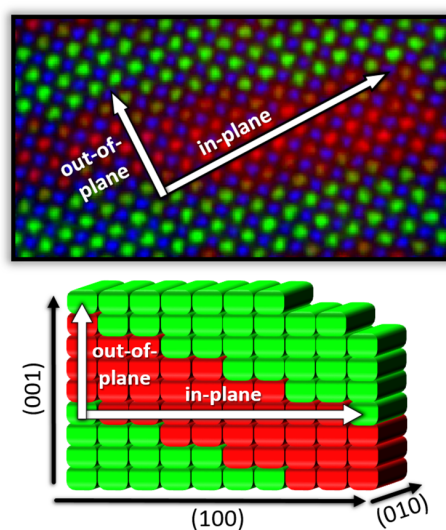
Graphical abstract This bi-directional growth enables the simultaneous control of in-plane and out-of-plane orbital occupation. A notable outcome involves the realization of anisotropic ferromagnetism and superconductivity. This figure has been reproduced with permission from *Bonmassar et al.*[195]

4.1 Abstract

The pursuit of breakthroughs in thin film technology drives us to explore novel growth strategies of quantum materials that surpass conventional limitations. Departing from the prevailing unidirectional growth approach, our methodology allows for atomic precision in both the in-plane and out-of-plane directions. To demonstrate the capabilities of this transformative technique, we engineer a bi-directionally grown superlattice comprised of alternating $LaMnO_3$ and $SrMnO_3$ layers, enabling the emergence of interfacial ferromagnetism. By adopting this superlattice as a model system, we highlight the vast potential of our approach through comprehensive analysis and characterization. Furthermore, we extend the application of our method to the growth of superconducting $La_{1.84}Sr_{0.16}CuO_4$ thin films on various offcut substrates. Remarkably, these substrates induce an anisotropic critical current originating from two distinct mechanisms.

4.2 Introduction

Thin film technologies have catalyzed remarkable advancements in our society-, fueling technological quantum leaps in liquid crystal displays,[196] metal-oxide-semiconductor (MOS) transistors,[171] photovoltaic devices,[197] light emitting diodes[198] or magnetic memory devices.[199] Beyond their pervasive presence in our daily lives, thin films hold paramount significance in fundamental research, showcasing phenomena such as the electric field effect in a few atomic layers of carbon,[200] the quantum Hall effect in MOS devices,[19] and the giant magnetoresistance effect in Fe/Cr multi-layered thin films.[201] MBE ushered in a new era by enabling the production of thin films with unprecedented qualities.[91,114,202] Notably, the integration of MBE growth for oxide materials led to the realization of record-breaking physical properties, including high-T_C superconductivity and colossal magnetoresistance.[37,40,55,203,204] However, a common characteristic shared by all epitaxial thin films, irrespective of their crystal structure and properties, is their reliance on a single growth direction. Non-offcut thin films establish connections through either their in-plane or out-of-plane orbitals, resulting in orbital occupation predominantly in one direction at the interface. Nevertheless, the advent of offcut substrates can pave the way for a novel research frontier, wherein both the in-plane and out-of-plane orbital occupations can be simultaneously harnessed to investigate new material systems harboring unexplored physical phenomena. Regrettably, the attainment of controlled growth on an atomic scale in such materials remains an elusive goal. Consequently, the pursuit of coherent and controlled growth along two directions represents a potential game changer for all thin film technologies.

To provide a compelling visual representation of our bi-directional growth technique, we present Figure 41a, illustrating the atomic terrace-by-terrace process compared to the traditional uni-directional atomic layer-by-layer growth depicted in Figure 41b. The grey arrows demonstrate the arrangement of terraces (layers) during the growth process. Notably, our controlled bi-directional growth approach unlocks the capability of alternating in-plane and out-of-plane layers, offering a paradigm shift from one-dimensional growth methods, where materials are solely layered in the out-of-plane direction. The cornerstone of this offcut technology lies in the utilization of precisely engineered vicinal substrates providing high offcut angles, a crucial factor for enabling the formation of controlled terrace widths. In the past, vicinal substrates have been employed for the synthesis of various compounds, including fractional SLs,[205] investigating defect formation effects,[206] circumventing twin boundary formation in high-T_C superconductors like

YBCO,[207] the formation of antiphase boundaries,[208,209] and studying anisotropic transport properties in single-phase thin films.[210–212] Building upon this knowledge, we employ *in situ* RHEED-assisted MBE with unparalleled atomic precision to directly control the growth of terraces. In each deposition step, we deposit material A or B precisely atop the former terrace or adjacent, as illustrated in Figure 41a. This approach allows for the combined out-of-plane and in-plane growth, depending on whether the new terrace is deposited on top of or next to the former terrace, respectively. The orchestrated interplay of atomic interactions in our bi-directional growth scheme culminates in the realization of thin films with unprecedented control, atomic precision, and the ability to exhibit unique structural and functional properties.
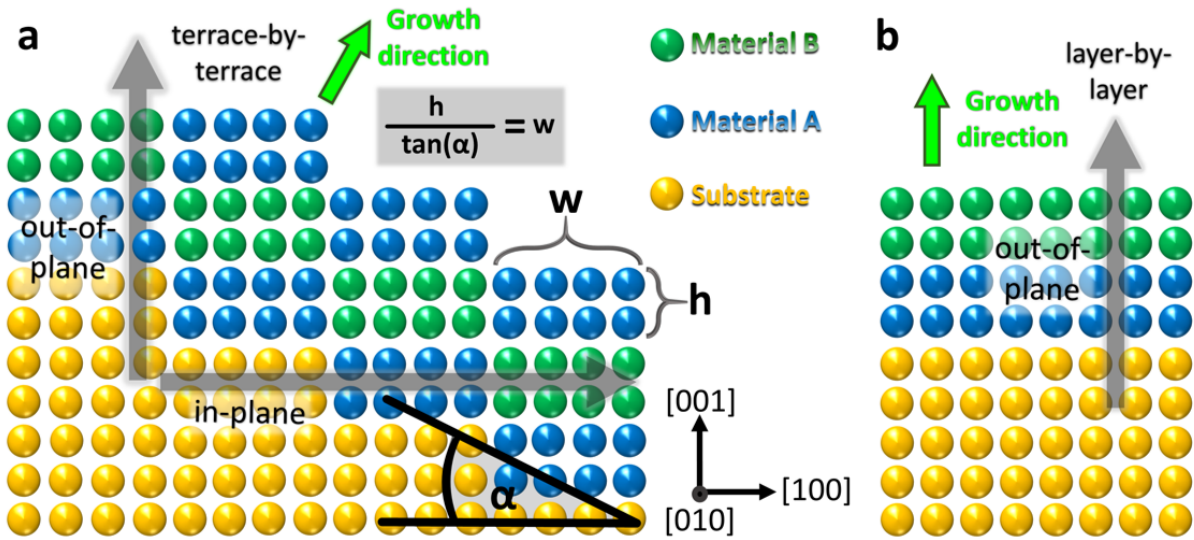
Figure 41: Comparison of the two growth mechanisms terrace-by-terrace vs. layer-by-layer growth. (a) Exemplifying the transformative potential of terrace-by-terrace growth allows for remarkable control over terrace width w by judiciously selecting the offcut angle α while maintaining a fixed step height value h of the substrate. The profound implications of this technique are highlighted by the emergence of both A (blue) and B (green) materials, manifesting in both the out-of-plane and in-plane directions (grey arrows), increasing the degree of freedom of the subsequent thin film. (b) In stark contrast, layer-by-layer growth on non-offcut substrates confines to a unidirectional growth (grey arrow). The green arrows depict the growth directions. This figure has been reproduced with permission from *Bonmassar et al.*[195]

In the realm of thin film engineering, recent strides in substrate treatment methodologies[213] coupled with the remarkable capabilities of *in situ* RHEED-assisted MBE,[40,45] have ushered in a new era, enabling the utilization of offcut substrates for the growth of bi-directional SLs. Crucially, the offcut angle α emerges as the decisive factor governing the terrace width w,[214] while the intrinsic step height of the substrate determines the height of the terraces h (Figure 41a). Note that while the thickness of individual layers in the SL is four unit cells, the sketch (Figure 41) displays one unit cell thick layer for a reader-friendly presentation. The precise control of terrace widths through this innovative approach grants us the ability to manipulate the size of the atomic building blocks for each layer within the heterostructure, consequently dictating the desired in-plane distances. This fine-grained control over the interlayer spacing of the bi-directionally grown thin film becomes instrumental in tailoring the material system's structural properties and emergent physical phenomena.

4.3 Methods

RHEED assisted MBE Growth under Ozone
SMO-LMO SL and LSCO thin films were grown on STO (001) (CrysTec GmbH) with an offcut angle of 25°and on LSAO (001) (CrysTec GmbH) with an offcut angle of 0°, 12°, and 25°along the (100) direction, respectively, using MBE under a strongly oxidizing atmosphere consisting of ozone, molecular- and radical oxygen (DCA Instruments).[45] The deposition conditions during all growths were ≈1·10-5 Torr and 680-700 °C (pyrometer temperature). Each deposited layer has been monitored by *in situ* RHEED during the growth.

Measurement of Physical Properties
The resistance (R) was measured with direct currents of ± 30 μA in a linear four-point-probe configuration. R measurements were controlled by a motorized custom-designed dipstick (temperature change rate < 0.1K/s) and samples were cooled down from room temperature to 4.2K. Magnetic properties were measured using a superconducting quantum interference device (SQUID) utilizing a Magnetic Property Measurement System (MPMS, Quantum Design Co.) in vibrational mode (vibrational sample magnetometry). Hall bars have been fabricated using UV-lithography. We determined the experimental error of both devices in two directions by measuring Hall bars fabricated from thin films grown on non-offcut substrates. Typically, the miscut angle of our LSAO substrates is about 0.3-0.5°, which corresponds to surface terrace widths of 120-80 nm.

STEM
All specimens were thinned to electron transparency by tripod-wedge polishing and subsequent ion polishing. A precision ion polishing system (PIPS II, Model 695) equipped with a liquid nitrogen filled cooling stage, to ensure for safe sample preparation without severely damaging the sample, using Ar^+ ions was utilized to thin the sample down to less than 30 nm thickness. STEM investigations were performed with a JEOL JEM-ARM200F, which is equipped with a cold-field emission gun, a probe Cs-corrector (DCOR, CEOS GmbH), and a Gatan GIF Quantum ERS electron energy-loss spectrometer with a following Gatan K2 direct electron-detection camera. A convergence semi-angle of 22 mrad resulting in a probe size of 0.8 Å has been used for all STEM and EELS analyses. The collection-angle range was 87-209 mrad for annular dark field (ADF) imaging. EELS data were acquired at a collection semi-angle of 87 mrad. An energy dispersion of 0.5 eV/channel (resulting in an energy resolution of less than 1 eV) and a pixel dwell time of 3.7 ms and were used for all EELS experiments. For the false color-coded RGB maps principle component analyses (PCA using 10 components) were performed to reduce the noise. Multiple linear least square (MLLS) fittings were performed on the PCA treated spectrum images to separate the peaks of the spectrum as described elsewhere.[167] The Mn L_3/L_2 white line ratios were analyzed using the raw data.

Atomic Force Microscopy (AFM) and X-ray Diffraction (XRD)
The AFM results were obtained utilizing an Asylum Cypher AFM in tapping mode. Out-of-plane x-ray diffraction patterns were recorded utilizing a monochromatic Cu-K$_{\alpha 1}$ source. The samples were tilted by 25°towards [100] to align the crystal into zone axis orientation.

4.4 Unveiling the Bi-directional Nature of the SL

To demonstrate the viability of our concept, we embark on the synthesis of a SL composed of two distinct materials $LaMnO_3$ (LMO) and $SrMnO_3$ (SMO), employing the precise control afforded by *in situ* RHEED-monitored ozone-assisted MBE. Our SL design features a repeating unit of four unit-cell thick SMO and LMO ultrathin layers, forming a basis bilayer stack that is replicated five times, ultimately constituting the complete SL structure. These intricate layers are grown on a (001)-oriented $SrTiO_3$ substrate, displaying a high offcut angle α of 25°towards the (100) direction, which is an essential parameter for our bi-directional growth approach. Analyzing the substrate's surface geometry reveals a step height of 0.390 nm, equating to the c-axis dimension of a single unit cell.[215]
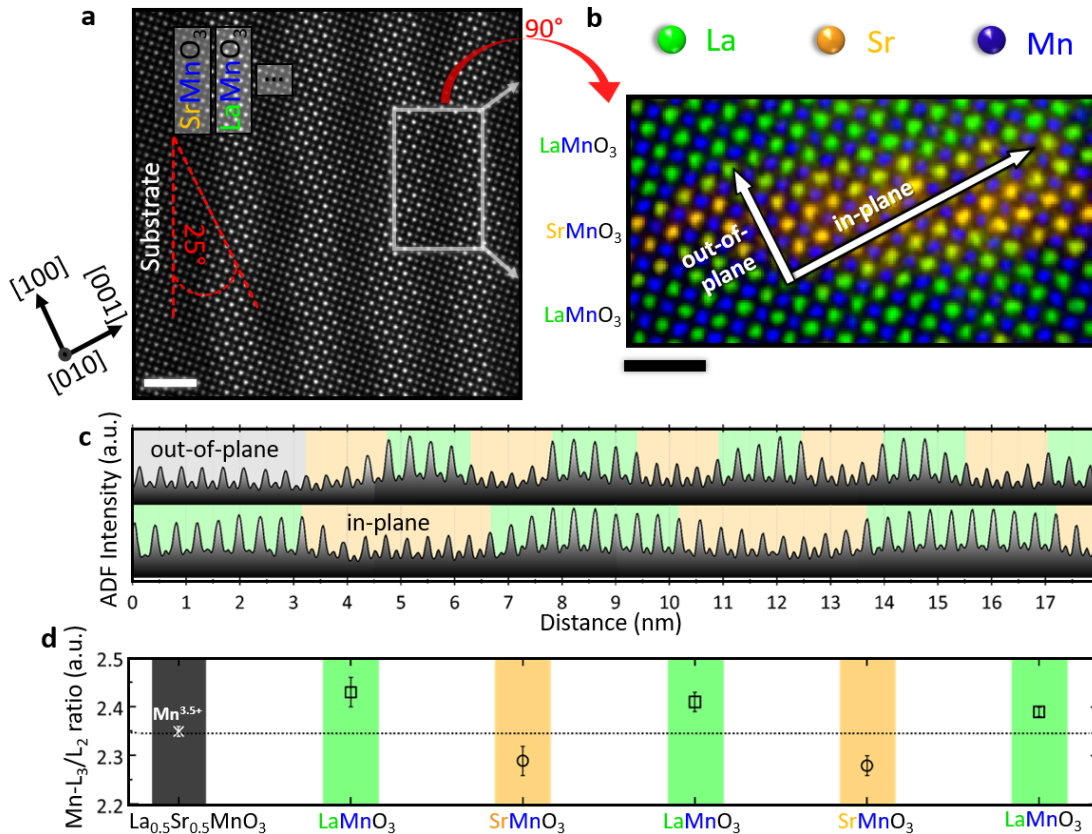
Figure 42: Structural and chemical analysis of the bi-directionally grown superlattice. (a) HAADF overview image reveals the alternating nature along the crystallographic [100] and [001] axis, illustrating the precise arrangement of layers. The white scale bar represents 2 nm. Notably, subtle thickness variations at the sub-nanometer scale manifest as contrasting regions in the HAADF images, with LMO layers exhibiting bright contrast and the SMO layers displaying dark contrast, a phenomenon observed even in conventional layer-by-layer grown SLs.[103,216] (b) EELS elemental mapping showcases the bi-directional character of the SL, with false color-coded representations of La (green), Sr (orange), and Mn (blue). The black scale bar represents 1 nm. (c) Profile plots along the crystallographic a- (in-plane) and c-axes (out-of-plane) offer a comprehensive illustration of the bi-directional nature of the SL. Green and orange background correspond to the LMO and SMO layers, respectively. (d) Mn L_3/L_2 white-line ratios serve as a powerful indicator of the alternating electronic states within the LMO and SMO layers. The profile backgrounds in green and orange highlight the respective layers, while the black background with the white cross represents the reference Mn L_3/L_2 ratio for the mixed $Mn3.5^+$ valence state in half-doped $La_{0.5}Sr_{0.5}MnO_3$. This figure has been reproduced with permission from *Bonmassar et al.*[195]

The mean terrace width amounts to a mere two unit cells. Remarkably, each building block within the SL structure, comprising either an SMO or LMO layer, corresponds theoretically to an in-plane distance spanning eight unit cells. Consequently, each terrace along the (100) direction encompasses a compositionally well-defined arrangement of four SMO and four LMO building blocks.
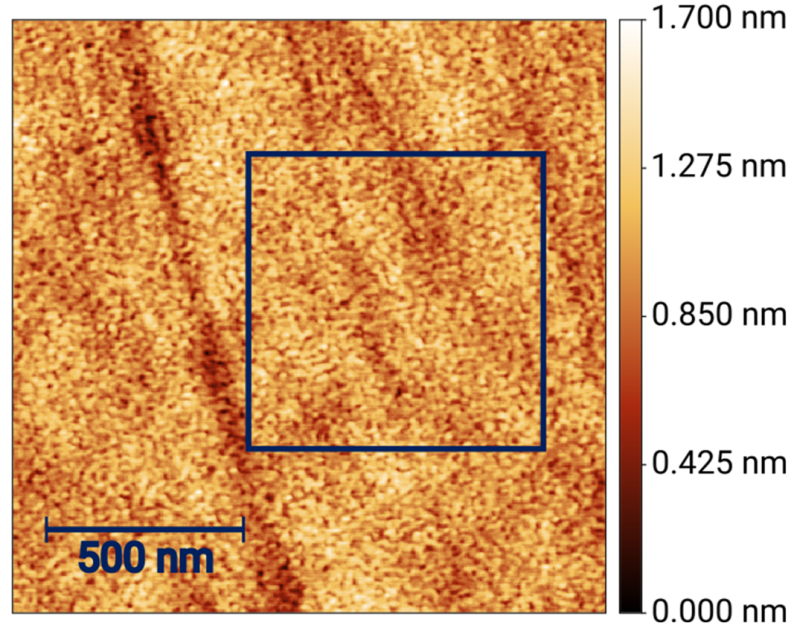
Figure 43: Atomic force microscopy proves the surface smoothness of the bi-directionally grown superlattice. The black box highlights the area, on which the root mean square roughness of 174 pm was determined. This figure has been reproduced with permission from *Bonmassar et al.*[195]
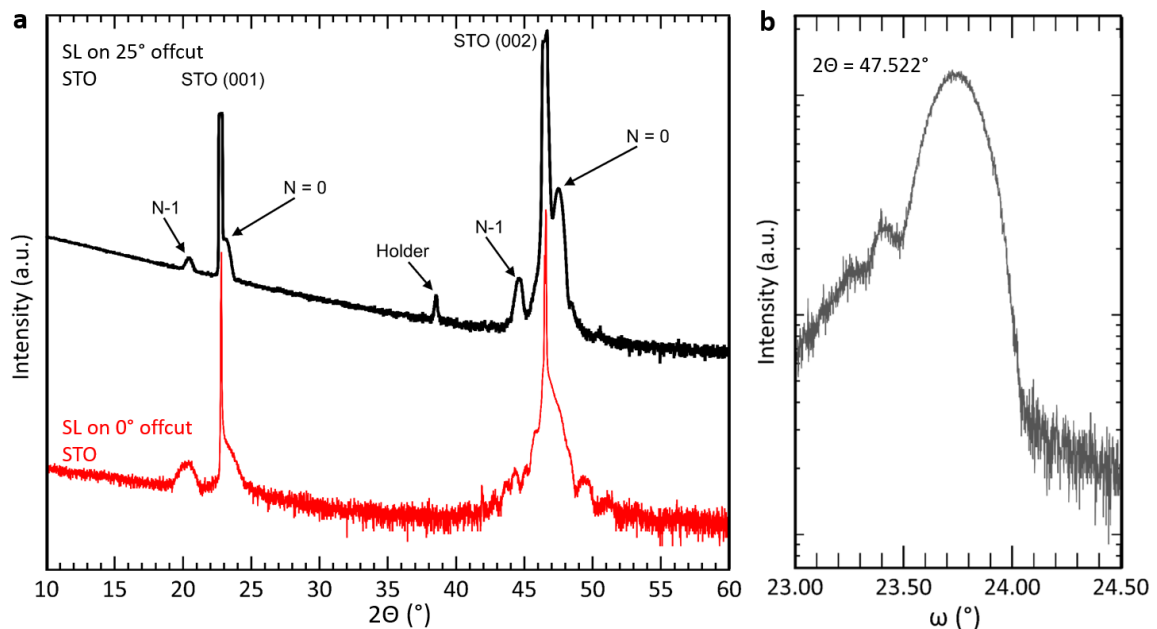
Figure 44: Comparison of the X-ray diffraction patterns of the bi-directionally grown manganite superlattice with the superlattice grown on a conventional substrate, highlights the high crystallographic quality on a macroscopic scale. Due to the huge offcut of 25°the sample had to be tilted into the exact angle leading to the observation of an additional peak from the holder. (b) Rocking curve (omega scan) of the bi-directionally grown superlattice obtained at $2\Theta = 47.522°$. This figure has been reproduced with permission from *Bonmassar et al.*[195]

Thorough characterization through atomic force microscopy and out-of-plane x-ray diffraction reinforces the exceptional quality and smoothness of the thin film surface, as evidenced by a surface roughness of only 0.174 nm (as showcased in Figure 43 and 44). These macroscopic-scale measurements affirm the structural integrity and fidelity achieved throughout the epitaxial growth process.

The profound influence of the strategically chosen 25 °offcut angle becomes strikingly evident when scrutinizing the crystallographic structure along the [100]-direction, as visualized by high-angle annular dark field (HAADF) imaging in Figure 42a and 45.
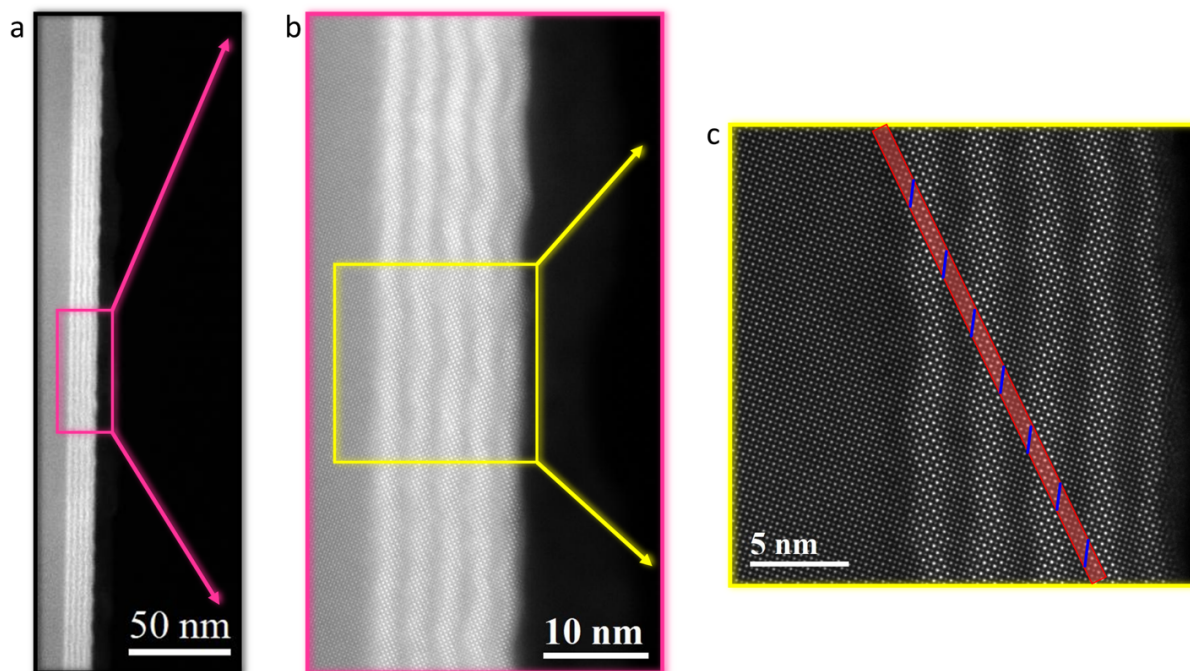
Figure 45: Annular dark-field overview images of the bi-directionally grown manganite superlattice at low (a), medium (b), and high (c), magnification. The red bar in (c) indicates the final terrace with atomic resolution to visualize the in-plane interfaces (blue lines) from $SrMnO_3$ (dark) to $LaMnO_3$ (bright). This figure has been reproduced with permission from *Bonmassar et al.*[195]

Figure 42b displays a captivating false color-coded elemental map (Sr: orange, La: green, and Mn: blue), providing a vivid visualization of the alternating arrangement of SMO and LMO layers in both the out-of-plane and in-plane directions, as discerned through electron energy-loss spectroscopy (EELS). The mean size of the in-plane building blocks, depicted by the orange and green backgrounds in Figure 42c, is found to be approximately 3.40 nm, which aligns remarkably well with the calculated in-plane distance of 3.350 nm. Intriguingly, measurements along the [100]-and [001]-directions (Figure 42c) reveal indistinguishable a-axis values (0.390±0.002 nm) for both LMO and SMO layers. However, the c-axes of the SMO layers exhibit an average value of 0.374±0.003 nm, a clear indication of tensile strain within these layers.[217] In contrast, the LMO layers maintain their (pseudo-)cubic crystal structure, as expected based on prior extensive discussions and reports.[43,103,216] The successful growth of the epitaxial thin film is further corroborated by the Mn L_3/L_2 white-line ratio analysis of the energy-loss near-edge structure (ELNES) (Figure 42d), where the anticipated alternation of Mn oxidation states is confirmed. The reference point of Mn3.5$^+$, representing half-doped $La_{0.5}Sr_{0.5}MnO_3$ (depicted by the white

cross), occupies an intermediate position between the individual LMO and SMO layers, reinforcing the desired Mn oxidation state modulation. A black dashed line has been included as visual guidance to aid readers' comprehension.

4.5 Emergence of Anisotropic Ferromagnetism
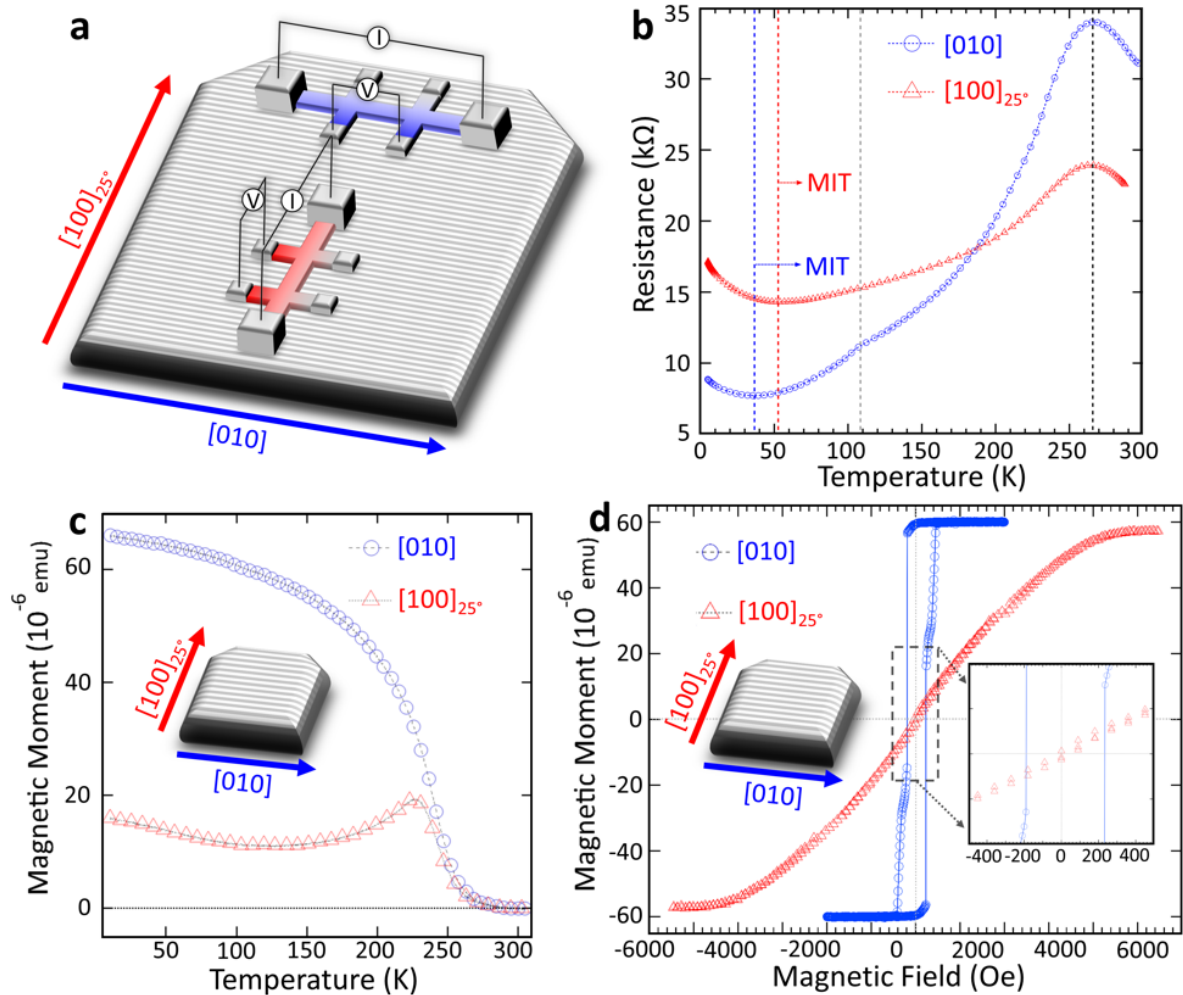
Figure 46: Anisotropic ferromagnetism in the $(SMO)_4 + (LMO)_4$ SL. (a) Illustration of the two Hall bars fabricated to align with the parallel (blue [010]) or perpendicular (red $[100]_{25°}$) orientations to the terraces. (b) and (c), Resistance and magnetization versus temperature profiles, respectively, obtained for both in-plane configurations. Intriguingly, a subtle resistance anomaly appears at 106 K (gray dashed line), potentially stemming from a cubic to tetragonal phase transition of the $SrTiO_3$ substrate.[218] The blue balls and red triangles symbolize the [010] and $[100]_{25°}$ directions, corresponding to the applied current and the magnetic field (field strength displays 500 Oe). (d) Magnetization versus magnetic field obtained at 100 K. The inset within panel d magnifies magnetic fields, highlighting disparate coercive fields in each direction. A distinct step around 200 Oe emerges in the hysteresis loop for the [010] direction, suggestive of a second magnetic phase characterized by marginally higher coercive fields. This figure has been reproduced with permission from *Bonmassar et al.*[195]

Controlling local magnetic properties is a crucial aspect of strongly correlated epitaxial superlattices. To investigate the impact of bi-directional growth on the physical properties, we focus on a SL composed of $(SMO)n + (LMO)n$ with periodicity n = 4. Previous studies

on non-offcut substrates have demonstrated that SMO-LMO SLs exhibit ferromagnetism (FM).[43,44,216] However, the transition to the metallic FM phase depends on the SMO:LMO ratio (1:2) and the periodicity with a limit of n $\geq$ 3 for the metallic FM phase.[44,216] In this study, we present the emergence of a Curie temperature (T_{Curie}) by harnessing the bi-directional nature of the SL, accompanied by intriguing anisotropic metallic transport properties (Figure 46). Temperature-dependent resistance measurements (R vs T) were performed on Hall bars with a width of 5 μm (schematically shown in Figure 46a) to ensure homogeneous current distribution. The transport properties parallel ([010], blue) and perpendicular to the terraces ($[100]_{25°}$, indicating a 25° tilt of the [100] direction, red) are determined, as depicted in Figure 46b. At room temperature, we observe anisotropic resistance values of 31 $k\Omega$ and 22 $k\Omega$ parallel and perpendicular to the terraces, respectively. Both directions exhibit a metal-to-insulator transition (MIT) at 265 K denoted by the black dashed line. Notably, the steeper slope in the parallel direction indicates a more metallic behavior as compared to the perpendicular direction. A second anisotropic MIT arises at 37 K and 53 K along the parallel and perpendicular directions to the terraces, respectively. The origin of these MITs may stem from strained materials as it has been discussed elsewhere.[219] This novel temperature-dependent field-free anisotropic transport mechanism strongly suggests anisotropic scattering processes due to the presence of alternating SMO and LMO phases along the crystallographic a- and b-axes as illustrated in Figure 42 and Figure 45.

Consistent with the initial MIT in resistance measurements, we further note the emergence of a T_{Curie} observed at 265 K in magnetization vs temperature measurements in Figure 46c. When a magnetic field of 500 Oe is applied, we observe lower magnetization perpendicular to the terraces compared to the parallel direction, indicating anisotropic saturation fields. This intriguing behavior is vividly demonstrated in Figure 46d, where magnetization vs magnetic field measurements at 100 K reveal distinct saturation fields. Along the [010] direction, a typical ferromagnetic hysteresis loop is observed, characterized by a coercive field of $\approx$ 200 Oe and a saturation field of $\approx$ 400 Oe. In contrast, the direction perpendicular to the terraces exhibits an almost superparamagnetic response without a measurable coercive field (as seen in the inset in Figure 46d) but displays a higher saturation field of $\approx$ 4500 Oe.

4.6 Emergence of Anisotropic high-T_C Superconductivity and Intrinsic Josephson Effect

Through our novel approach, we exert precise control over the growth of superconducting $La_{1.84}Sr_{0.16}CuO_4$ (LSCO) on offcut substrates of $LaSrAlO_4$ (LSAO), resulting in anisotropic critical currents (I_C) originating from two different crystallographic directions with distinct mechanisms. While offcut substrates are conventionally employed to fabricate intrinsic Josephson junctions owing by tilting the c-axis towards in-plane orientations (Figure 47a,b, red), we unveil an additional effect: The confinement of the width of the superconducting planes in one direction giving rise to superconducting stripes along the [010] direction (Figure 47a,b, blue). To investigate these superconducting films, we fabricate Hall bars, as depicted in Figure 47c, each with a width of 10 μm, enabling measurements of I-V (measured at 4.2 K) and R-T characteristics either parallel (blue data points) or perpendicular (red data points) orientations to the terraces, as illustrated in Figure 47d,e. Significantly, the LSCO films grown on 25° offcut substrates exhibit two effects originating from different mechanisms. The first effect arises from intrinsic c-axis tunneling, i.e., intrinsic Josephson effect, evident in the I-V measurements along the
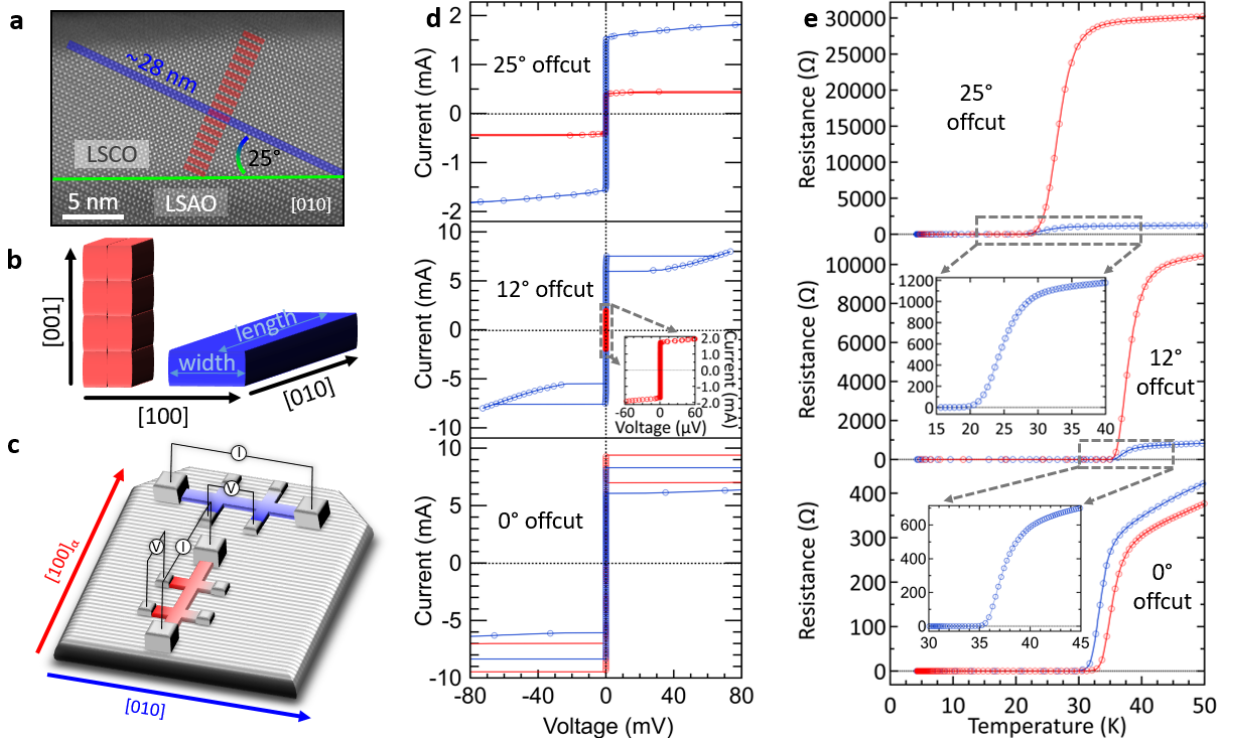
Figure 47: Anisotropic superconductivity in LSCO thin films. (a) HAADF image revealing the origin of the anisotropic I_C in an LSCO thin film grown on a 25° offcut LSAO substrate. The intrinsic Josephson effect arises from c-axis tunneling (depicted as red blocks), while the narrow terrace width (indicated by a blue line) creates a weak link along the crystal's a-axis. (b) Illustration displaying the red and blue regions from panel A emphasizing the intrinsic c-axis tunneling (red) and the width and length of the resulting superconducting stripes (blue). (c) Schematic representation of two Hall bars with a width of 10 μm, oriented in parallel (blue [010]) and perpendicular (red [100]$_\alpha$) directions to the terraces. (d) and (e) Current-Voltage (I-V) characteristics conducted at 4.2 K of three distinct LSCO thin films, measured parallel (blue) and perpendicular (red) to the terraces and R-T curves illustrating the T_C measured parallel (blue) and perpendicular (red) to the terraces. As a consequence of the weak link formation in the canted superconducting stripes, they show a lower T_C of about 20 K compared to the other LSCO thin films with a T_C above 30 K. This figure has been reproduced with permission from *Bonmassar et al.*[195]

[100]$_{25°}$ direction. The second effect occurring along the [010] direction, stems from the formation of superconducting stripes with an approximate width of ≈ 28 nm ($\frac{0.66\,\text{nm}}{\tan(25°)}$) and a length spanning from several hundred to thousands of nm, contingent upon substrate quality. This work demonstrates a facile approach to simultaneously generate two different types of homojunctions within the same sample. Notably, on 12° offcut substrates, a pronounced anisotropy along the [010] (blue) and [100]$_{12°}$ (red) directions is discernible in both the I-V and R-T measurements. Along the [010] direction, the I-V measurements exhibit a minor hysteresis loop, while the I-V measurement along the [100]$_{12°}$ direction displays a prominent intrinsic Josephson effect. On 0° offcut substrates, the I-V curves for LSCO manifest strong isotropic hysteresis loops, likely attributable to Joule heating,[220] whereas R-T measurements reveal no discernible signs of anisotropy within the experimental error of $\approx 10\%$.

4.7 Discussion

We present a terrace-by-terrace growth using *in situ* RHEED-assisted MBE, enabling
precise control over the ferromagnetic and superconducting properties in two crystallo-
graphic dimensions. The strong coherence originating from homogenous terrace widths
results in controlled and coherent growth along both axes. To demonstrate the effi-
cacy of our approach, we fabricate a SL composed of five bilayers of $(SMO)_4 - (LMO)_4$.
Through atomic-scale modulation of the in-plane and out-of-plane orbital occupation, we
successfully transform an insulating material (n = 4 and SMO:LMO ratio of 1:1) into
a ferromagnetic metal. We attain precise control over orbital occupation by employing
in situ monitoring of RHEED oscillations, indicative of shutter openings from individual
element sources (refer to SI Figure 48 and SI Figure 49).
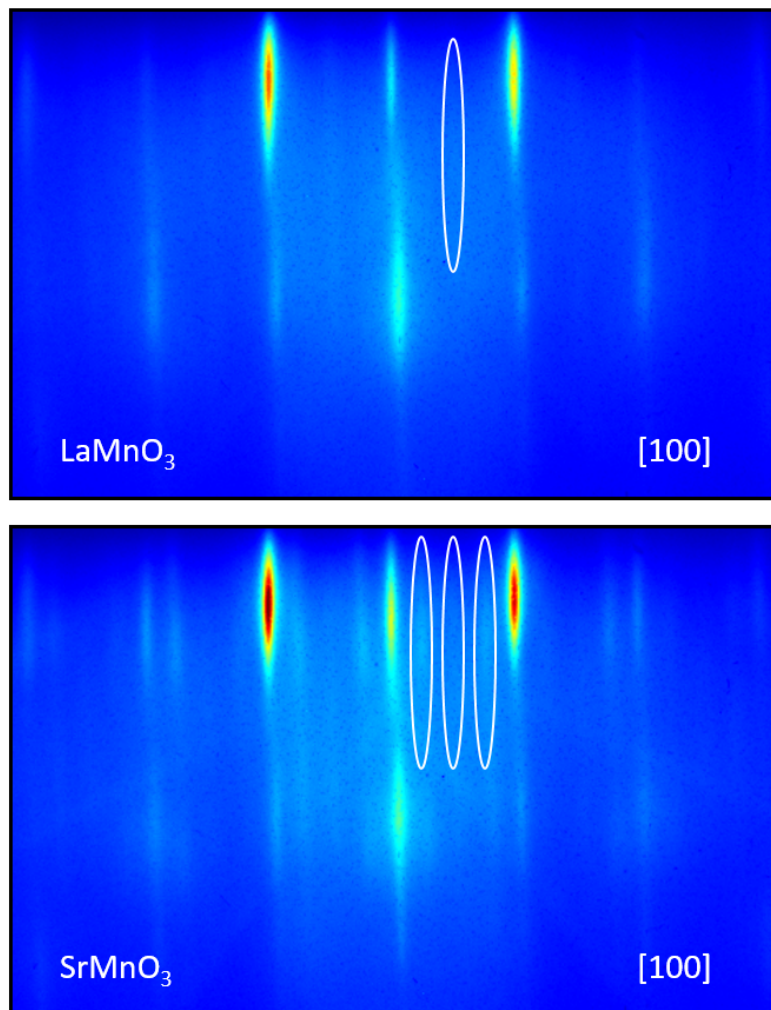
Figure 48: *In situ* reflection high-energy electron diffraction patterns obtained of $LaMnO_3$ and
$SrMnO_3$ layers during the growth. The white ellipses indicate the presence of a superstructure,
which is more visible in the $SrMnO_3$ layers than in the $LaMnO_3$ layers. This figure has been
reproduced with permission from *Bonmassar et al.*[195]

Specifically, the deposition of each atomic layer on individual terraces, contributing to
the bi-directional terrace-by-terrace growth, is tracked precisely through the RHEED sig-
nal. The alternating structures observed within the in-plane direction bear tremendous
scientific significance, particularly in the realm of oxide-based in-plane Josephson junc-
tions, which hold immense promise as future building blocks for the design of novel qubits

exploiting π-junctions. The pronounced anisotropy in coercive fields (200 Oe vs 0 Oe) suggests potential applications of this bi-directionally grown heterostructure as a spin valve, promising for future spintronic devices. Furthermore, leveraging our atomically precise growth technique, we grow superconducting LSCO films leading to the formation of anisotropic homojunctions. These junctions exhibit two distinct mechanisms: i) the intrinsic Josephson effect, facilitated by c-axis tunneling across the terraces, and ii) the creation of superconducting stripes with a width of < 30 nm, effectively forming a weak link due to a confinement effect. Our findings highlight the critical role of offcut substrates in driving the formation of bi-directionally grown thin films that encompass anisotropic ferromagnetism and facilitate the emergence of anisotropic superconductivity. Through this study, we highlight the transformative potential of our novel growth technique and shed light on the underlying mechanisms governing the behavior of advanced thin film systems. Our preliminary results represent a promising way for the design and fabrication of highly tailored thin-film architectures with functionalities that have never been reported before, thereby unlocking unprecedented opportunities for the development of next-generation electronic, spintronic, and quantum devices.
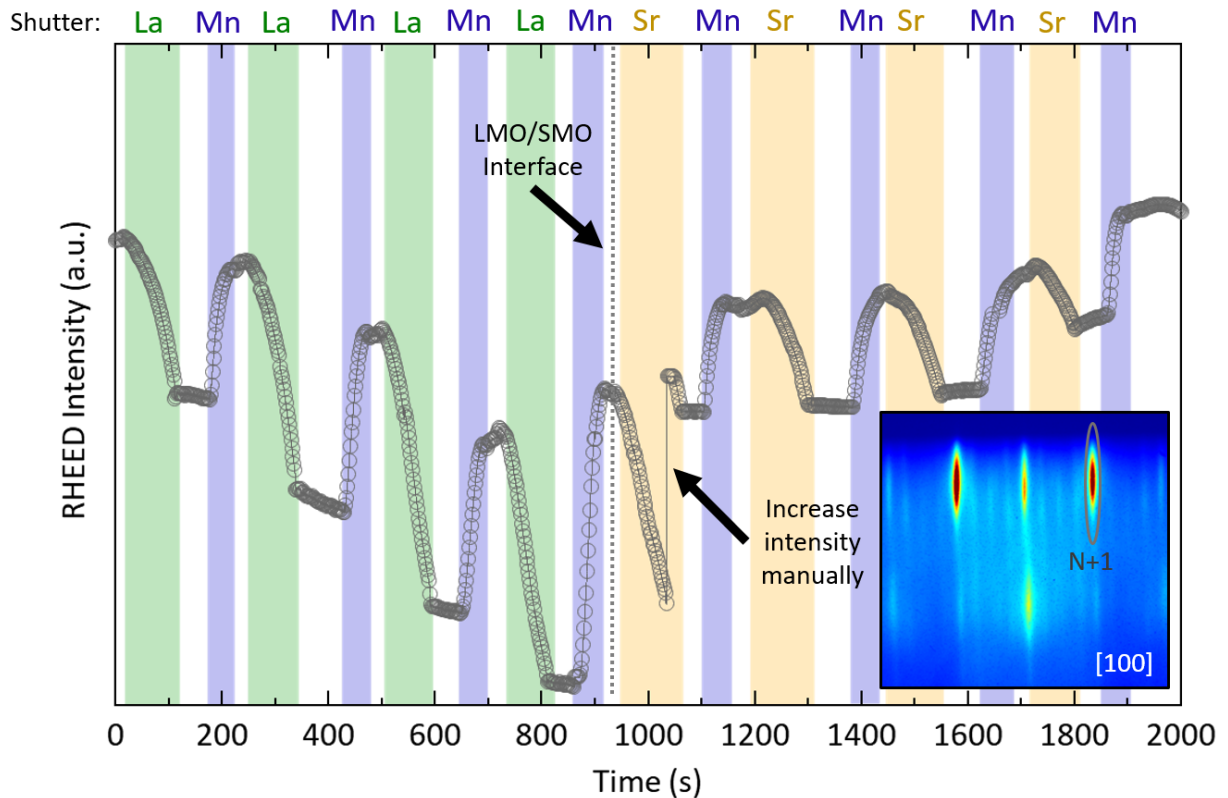
Figure 49: Real-time monitoring and control of the bidirectional growth by adjusting the *in situ* high-energy electron diffraction oscillations of the N+1 reflection, see inset bottom right. The decrease in intensity during the La/Sr shutter opening, highlighted by the green/orange background, is due to A-site cation deposition, while the increase in intensity during the Mn shutter opening is due to Mn deposition, highlighted by the blue background. Note that the sudden jump at about 1000s is due to manually increasing the intensity by increasing the filament current. This figure has been reproduced with permission from *Bonmassar et al.*[195]

5 Offcut Substrate-Induced Defect Trapping at Step Edges

In the final part of my thesis, I explore the possibilities associated with the use of bidirectional growth, highlighting the opportunities for defect engineering at the atomic scale. The underlying idea of this work was to trap defects at step edges, leading to defect-free bulk structures. More specifically, we successfully prevented the formation of antiphase boundaries in bulk $La_{0.66}Sr_{0.34}MnO_3$. Since the terrace widths in 15°offcut $LaSrAlO_4$ substrates are as small as 2.5 nm, a high density of step edges is present at the surface. Defect trapping occurs in the first two unit cells of the deposited material and leads to strong relaxation after the step edge has grown over, allowing defect-free thin film growth in subsequent layers. The prevention of antiphase boundary formation is critical as it ensures the integrity and coherence of crystal structures, preserves material homogeneity, and improves the overall performance and reliability of electronic and spintronic devices in terms of consistent electrical properties. In addition, suppression of antiphase boundaries is essential in the production of superconducting materials, ensuring uniformity in the crystal lattice and enhancing the superconducting properties. Therefore, the use of offcut substrates is emerging as a route to defect engineering at oxide interfaces.

Contributions to this publication:
Nicolas Bonmassar conceived the project, wrote the initial manuscript, performed the growth of all samples by MBE using *in situ* RHEED, prepared the samples by tripod polishing, performed the TEM acquisition, performed the TEM data analysis, performed the mutual inductance measurements on the devices, and performed the superconducting quantum interference device measurements. Georg Christiani and Gennady Logvenov assisted with sample growth. Y. Eren Suyolcu and Peter A. van Aken supervised this project and provided valuable input on data analysis. All co-authors revised the manuscript.

The following text and figures from this chapter are adopted from: Bonmassar, N., Christiani, G., Logvenov, G., Suyolcu, Y. E. and van Aken, P. A. Offcut Substrate-Induced Defect Trapping at Step Edges. Nano Lett., 10.1021/acs.nanolett.4c00832 (2024).[221]
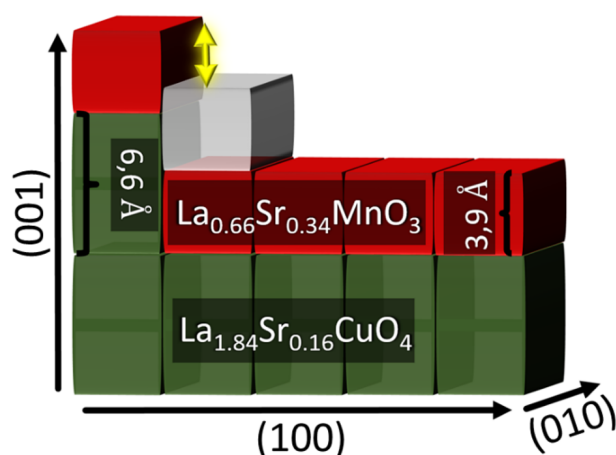
Graphical Abstract: Origin of the defective unit cell (gray) at the step edge. Due to the lattice mismatch between $La_{0.66}Sr_{0.34}MnO_3$ and $La_{1.84}Sr_{0.16}CuO_4$ the $La_{0.66}Sr_{0.34}MnO_3$ structure adapts to the underlying $La_{1.84}Sr_{0.16}CuO_4$ via the formation of a defective unit cell. This unit cell was identified as the second unit cell in direct proximity to the step edge. This figure has been reproduced with permission from *Bonmassar et al.*[221]

5.1 Abstract

We report step edge-induced localized defects suppressing subsequent antiphase boundary formation in the bulk structure of a trilayer oxide heterostructure. The heterostructure encompasses a layer of $La_{0.66}Sr_{0.34}MnO_3$ sandwiched between a superconducting $La_{1.84}Sr_{0.16}CuO_4$ bottom layer and an insulating La_2CuO_4 top layer. The combination of a minor a-axis mismatch (Δ 0.11 Å) and a pronounced c-axis mismatch (Δ 2.73 Å) at the step edges leads to the emergence of localized defects exclusively forming at the step edge. Employing atomically resolved electron energy-loss spectroscopy maps, we discern the electronic state of those defects in the second $La_{0.66}Sr_{0.34}MnO_3$ unit cell near the step edge. In particular, a reduction in the pre-edge region of the O-K edge indicates the formation of oxygen vacancies induced by the strained step edge. This study underscores our capability to control defects at the nanoscale.

5.2 Introduction

Precise control of defect formation is of paramount importance for spintronics and electronic devices, as these imperfections can strongly affect material conductivity,[23,222] magnetism,[223] and ultimately device functionality.[224] The manipulation of defects at the step edges, which can induce antiphase boundaries (APBs) plays an important role in catalysis,[225] where their presence can drastically influence surface interactions,[226] reaction pathways,[227] and catalytic efficiency.[226] Hence, understanding the underlying mechanism governing the formation and control of defects presents transformative prospects for elevating both device performances and catalytic processes.[228,229] Recent investigations have unveiled the formation of APBs, notably originating at the step edges of substrate terraces.[209] Furthermore, it has been demonstrated that two APBs tend to merge when two steps are closely positioned next to each other to minimize their surface energy.[209] We used precise offcut substrates, ensuring uniform terrace widths, and consequently reducing the distances between step edges resulting in a high density of step edges.[230] Ozone-assisted MBE guided by RHEED stands as the forefront technique, ensuring high-quality complex oxide heterostructures.[40,41] This approach not only achieves exceptional film quality but also empowers precise control over the growth of individual unit cells.[114,231] Complex oxides have established themselves as record holders in diverse properties, including high-T_C superconductivity,[37,91,232] colossal magnetoresistance,[233] and multiferroicity,[234] underscoring their exceptional versatility and performance.[55]

Here, we focus on the profound impact of large offcut angles, yielding nanometer-scale terrace widths of a mere five to seven unit cells. This structural design manifests in the formation of localized defects at step edges. To probe this phenomenon, we employed STEM-EELS and HAADF imaging. We complement these advanced imaging techniques with extensive data analysis methodologies such as ELNES and geometric phase analysis (GPA), to meticulously examine the formation of defects.[235] Through this multi-faceted approach, we unveiled the formation of defects at the step edge but also discerned their electronic- and crystallographic characteristics, leading to the prohibition of APBs.

5.3 Methods

RHEED-Assisted MBE Growth in Ozone
LSCO-LSMO-LSCO heterostructures were epitaxially grown on LSAO (001) (CrysTec GmbH) with a 15°offcut angle toward the (010) direction, respectively, using MBE under a highly oxidative atmosphere composed of ozone, molecular oxygen, and radical oxygen (DCA Instruments). The growth process for all depositions took place at approximately 1·10-5 Torr and temperatures ranging from 680 to 700 °C as measured by a pyrometer. *In situ* RHEED was employed to monitor each deposited layer during the growth.

Diamagnetic Response Signal
Measurements of mutual inductance (MI) were carried out using a two-coil configuration (parallel geometry) with an alternating current of 50 μA and a frequency of 1000 Hz to determine the real and imaginary components of the magnetic susceptibility.

STEM
All specimens were thinned to electron transparency using tripod-wedge polishing, followed by ion polishing. Ar^+ ion thinning the samples to less than 30 nm thickness was accomplished using a precision ion polishing system (PIPS II, Model 695) equipped with a cooling stage filled with liquid nitrogen to minimize sample preparation-induced artefacts. STEM analyses were performed using a JEOL JEM-ARM200F transmission electron microscope equipped with a cold-field emission gun, a probe CS-corrector (DCOR, CEOS GmbH), and a Gatan GIF Quantum ERS electron energy-loss spectrometer. A convergence semi-angle of 22 mrad, resulting in a probe size of 0.8 Å, was used for all STEM and EELS analyses. HAADF imaging was performed within a collection-angle range of 87-209 mrad. EELS data were acquired with a collection semi-angle of 87 mrad. A 0.5 eV/channel energy dispersion (yielding an energy resolution of less than 1 eV) and a pixel dwell time of 3.7 ms were employed for all EELS experiments. To reduce noise, false color-coded RGB maps were generated using principal component analysis (PCA) with 10 components. Multiple linear least square (MLLS) fitting of PCA-treated spectra was performed to separate spectral peaks.[167] Analyses of Mn-$L_{2,3}$ and O-K edges were carried out using raw data. Strain analysis was conducted using Geometry Phase Analysis (GPA), a technique pioneered by Martin Hytch, through a commercial GPA plugin (HREM Research Inc.) integrated into Gatan DigitalMicrograph software.

5.4 Observation of Defect Formation at Step Edges
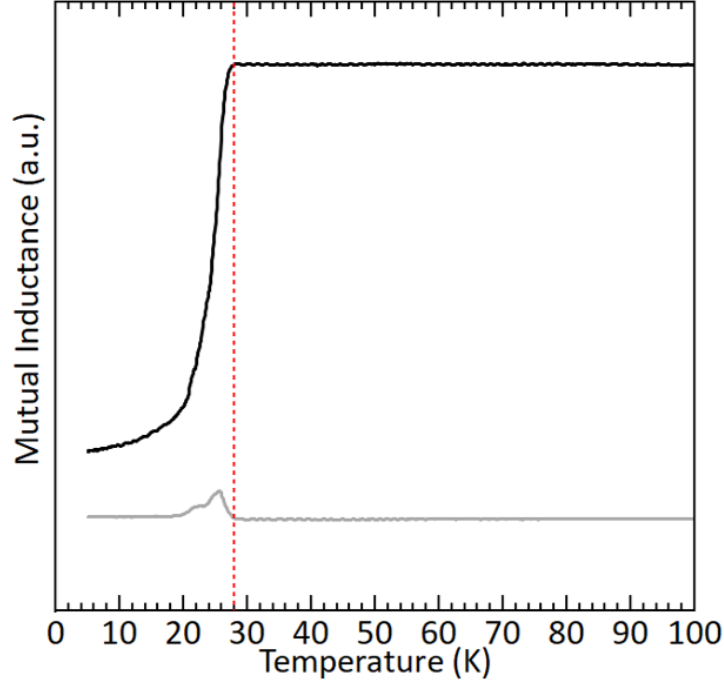
Figure 50: Temperature dependent mutual inductance measurement showcasing the superconducting transition at around 28 K (red vertical dashed line). This figure has been reproduced with permission from *Bonmassar et al.*[221]

Initially, we focus on a trilayer consisting of a $La_{0.66}Sr_{0.34}MnO_3$ (LSMO) layer with perovskite-type pseudo-cubic 113 crystal structure sandwiched between a superconducting $La_{1.84}Sr_{0.16}CuO_4$ (LSCO) bottom layer with tetragonal K_2NiF_4 type (or 214) crystal structure (see mutual inductance measurements in Figure 50 for the superconducting property) and an insulating La_2CuO_4 (LCO) top layer. This trilayer was grown on (001) oriented $LaSrAlO_4$ (LSAO) with an offcut of 15° toward the a-axis, allowing for the study of defect formation at step edges occurring every 1-2 nm. On top of that, the use of high-angle offcut substrates allows for the growth of a heterostructure where ferromagnetic layers (LSMO) are in the same plane as superconducting (LSCO) or antiferromagnetic (LCO) layers.

A minor a-axis mismatch of 0.11 Å and a substantial c-axis mismatch of 2.73 Å arise at the step edge. Note that for our calculations, we used the bulk values from the literature for a tetragonal half-unit cell LSCO and a pseudo-cubic approximation for LSMO.[236,237] Figure 51a illustrates the dislocations at the step edges (indicated by dashed yellow boxes, a direct outcome of the pronounced c-axis mismatch. The green lines correspond to the widths of the initial substrate terraces, marking the origin of the subsequent heterostructure. Focusing on the LSAO/LSCO interface, no detectable defects are observed. Figure 51b further illustrates the formation of the defective unit cell. The two unit cells of LSMO (red and blue spheres) sum up to a total out-of-plane value of 7.76 Å, whereas an LSCO half-unit cell (red and green spheres) has a c-axis value of 6.61 Å. The effect of this mismatch is pointed out by the yellow arrow. This concept is proven by atomically resolved EELS elemental mapping (Mn: blue, La: red, and Cu: green) showcased in Figure 51c. Here, the defective unit cell can be identified as the second LSMO unit cell in proximity to the step edge, highlighted by the gray circle. Lattice adaption to the structural mismatch

and chemical intermixing of the Cu atoms from the LSCO into the second LSMO unit cell at the step edge, leads to this localized defect formation. Elemental profiles of the cation distribution are shown in SI Figure 52. Furthermore, the LSMO layers vary slightly in their thicknesses, which can be attributed to step bunching due to imperfect substrates and step bunching occurring during the growth.
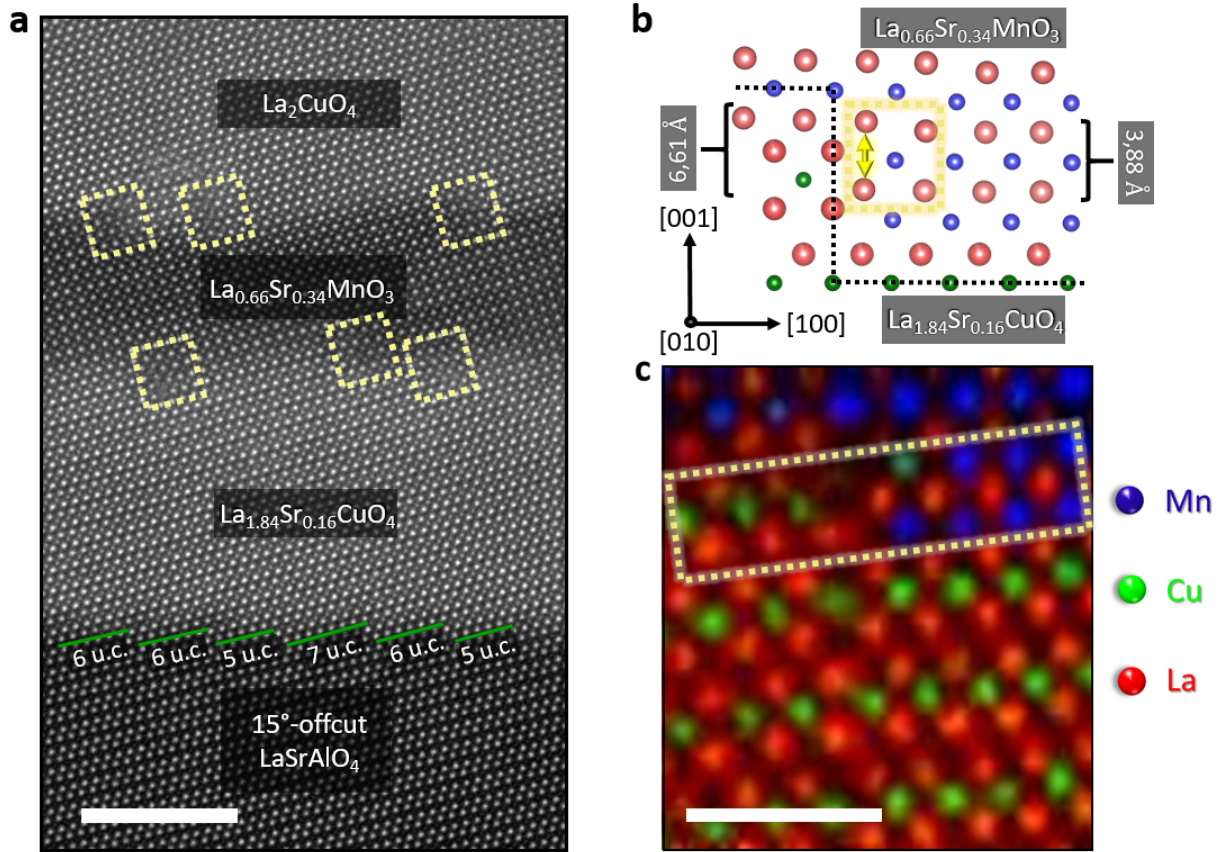
Figure 51: Step Edge Induced Defect Formation. (a) Overview HAADF image of the trilayer system, LSCO-LSMO -LCO, grown on LSAO possessing a 15° offcut angle towards the b-axis. Red (blue in panel c) arrows point out the step edges. Green lines highlight the different terrace widths of the substrate. The scale bar is 5 nm. (b) Illustration of the mechanism behind the defect formation. Due to the considerable c-axis mismatch between LSMO and LSCO, the system forms a defect, indicated by the gray box. (c) Atomically resolved EELS mapping shows that the defect is formed in the second LSMO unit cell highlighted by the gray circle. The two arrows point out the interface between LSCO and LSMO. This figure has been reproduced with permission from *Bonmassar et al.*[221]

Moreover, we demonstrate that this mismatch between the crystal structures at the step edge induces the formation of a complicated bonding situation at the step edge as indicated by the two arrows in Figure 51c. Here, the Cu B-site cation (green) within the LSCO phase undergoes a positional exchange with the La A-site cation (red) of the LSMO phase. Simultaneously, the La A-site cation (red) within the LSCO phase executes a positional exchange with the Mn B-site cation (blue).

Despite these local irregularities, the *in situ* obtained RHEED images do not show any sign of defect formation during the growth, as indicated in Figure 53 do not show any evidence of defect formations. In addition, there is no APB formation in the subsequent LSMO or
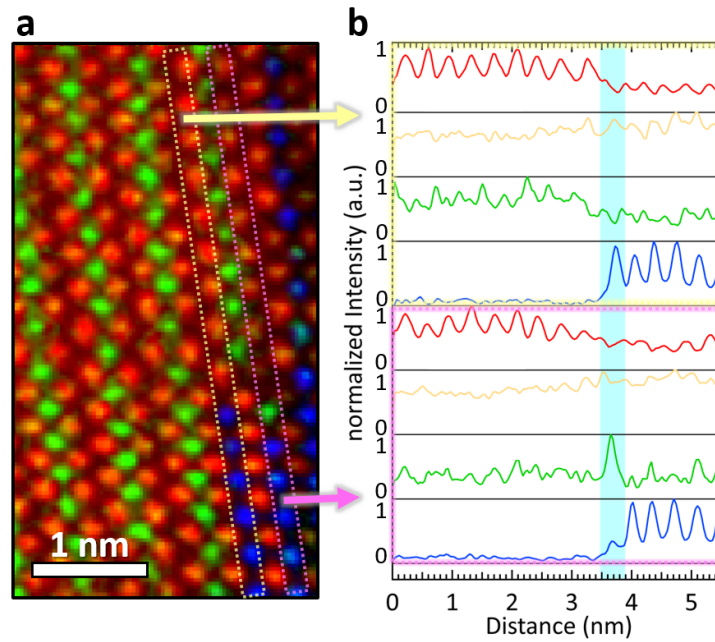
Figure 52: Elemental map (**a**) and profiles (**b**) of La (red), Sr (yellow), Cu (green), and Mn (blue) obtained from the yellow and pink dashed rectangles. The turquoise background in panel (**b**) marks the position of the step edge. This figure has been reproduced with permission from *Bonmassar et al.*[221]

LCO layer, which are typically found at step edges with large lattice mismatches.[209] The surface reconstruction highlighting half-order streaks, which is visible in Fig. 53a,b along the [100] azimuth is due to excess B-site cations.[238] The diffuse lines originate from Kikuchi lines.[239] No modifications of the RHEED images are observed at the interface between LSCO/LSMO or LSMO/LCO. Such deviations from defect-free RHEED images would manifest in sharp reflections at positions different from the substrate or the respective thin film material.[239,240]
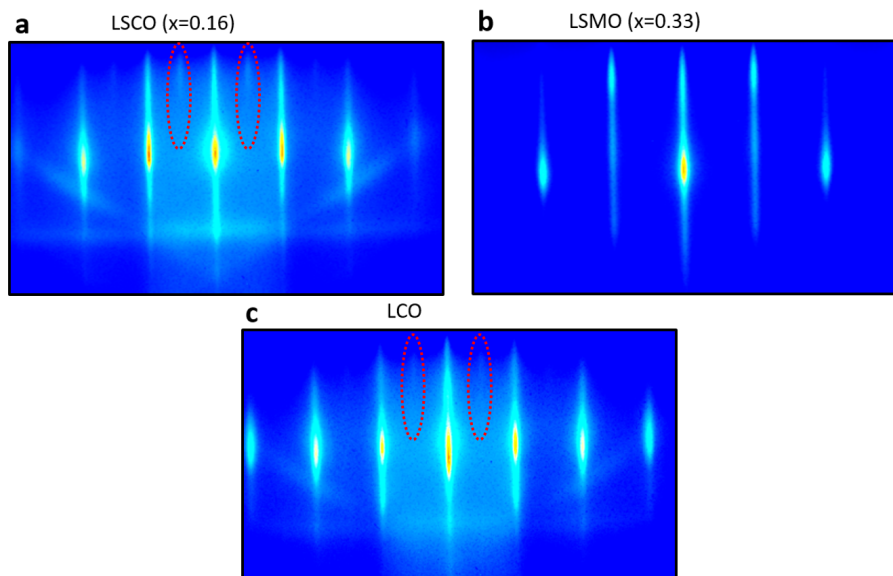
Figure 53: RHEED images of distinct monolayers during the growth: (a) 15 ML of LSCO (x=0.16), (b) 16 ML LSMO (x=0.33), and (c) 26 ML of LCO. This figure has been reproduced with permission from *Bonmassar et al.*[221]

5.5 Strain mapping
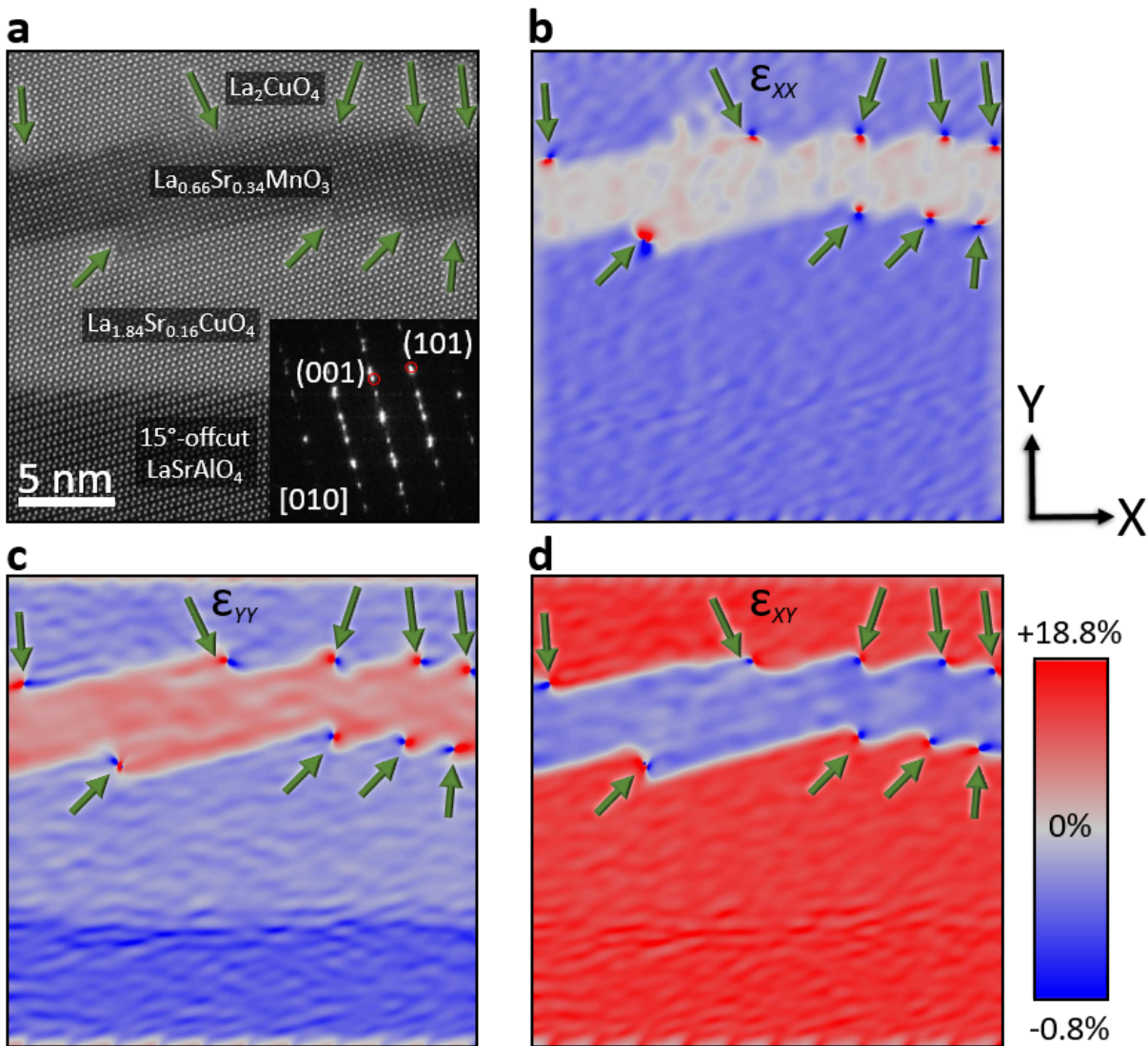
Figure 54: Strain-induced lattice deformation in highly perturbed materials. (a) HAADF image highlighting the specific area used for the strain calculation. The inset shows the FFT with the two reciprocal lattice vectors g_1 (001) and g_2 (101) within red circles, which have been used for the strain analysis. (b) Lattice mismatch in the X-direction of the image. (c) Lattice mismatch in the Y-direction of the image. (d) Shear strain highlighting the mean lattice dilatation. Red arrows point out distinct step edges of interest and the gray arrow points out the interface of the LSAO substrate to the LSCO layer. The X and Y directions of the image are indicated by the black arrows. Blue arrows point out the same positions as the red ones, but the color has been changed for simplicity for the reader. This figure has been reproduced with permission from *Bonmassar et al.*[221]

Figure 54 presents discernible strain variations within the heterostructure, utilizing geometric phase analysis. Conventionally, strain mappings have been applied to materials with subtle lattice distortions. However, in the context of this investigation, significant c-axis lattice mismatches of up to 18% introduce complexities that may challenge a straightforward interpretation of the data. Our focus is exclusively on the step edge regions, where a correlation between large lattice mismatches and localized strain effects is deduced from the strain mapping. Figure 54a represents an overview HAADF image presenting the

region of interest for the strain analysis. The inset in Figure 54a corresponds to a fast Fourier transformation of the HAADF image, highlighting the presence of reciprocal lattice vectors g_1 (0-11) and g_2 (011), encircled in red. Both g-vectors correspond to the sandwiched pseudocubic LSMO layer and are carefully selected to enhance the visibility of the strain states at the step edge interfaces. The LSMO layer was used as the reference area and the spatial resolution of the strain mapping is 1.15 nm. In Figure 54b, the strain in the X-direction is shown, revealing strongly strained materials at the LSCO/LSMO and LSMO/LCO step edges. Figure 54c presents the strain in the Y-direction, highlighting substantial strain localization at the step edge region indicated by the green arrows. The step edge region, denoted by the green arrows, emerges as a hotspot of tensile strain, which can introduce oxygen vacancies.[241] Additionally, Figure 54d depicts shear strain distributions, unraveling tensile strain (red) within the LSAO, LSCO, and LCO layers, as indicated by the green arrows, ascribed to the relatively smaller a- and much higher c-axes of LSAO, LSCO, and LCO compared to the reference area LSMO. Moreover, the observed shear strain (Figure 54d) further reinforces the correlation between localized structural perturbations and distinct oxidation states of Mn atoms within the step edge regions. While tensile strain can drive the formation of oxygen vacancies,[41,242] we exercise caution in attributing their formation at the step edge solely based on strain analysis. Therefore, our efforts are shifting towards atomically resolved ELNES analyses, poised to provide a conclusive understanding of the step edge region.

5.6 Electronic Configuration of Step Edge Defects

Figure 55a represents a HAADF image showcasing the step edge, with distinct regions marked by four unit cells of LSMO and the interface between the LSCO (pink background) and the LSMO (yellow background) through a white dashed line. Note that the dashed white lines go through the bottom and top B-site cations of the LSCO and LSMO unit cells, respectively, to highlight the formation of intermixed Cu-Mn materials. This type of intermixing is described elsewhere.[169] The gray arrow and the dashed circle point out the position of the region of interest at the step edge. We focus on the pre-edge region of the O-K edge, as it provides accessible means to observe and analyze electronic changes due to the hybridization of oxygen 2p orbitals with transition metal 3d t_{2g} and e_g orbitals. This approach allowed us to gain valuable insights into the electronic states at the atomic scale despite the inherent limitations of energy resolution in atomically resolved ELNES depicted in Figure 55b. Within this pre-edge region, there are discernible changes characterized by a significant decrease in the intensity of the pre-peak feature, highlighted against a green background. This reduction in intensity signifies a corresponding reduction in the Mn valence state.[243] This finding concurs with established reports, where the pronounced tensile strain can increase the oxygen vacancy concentration and, therefore, introduce electrons into the system, subsequently reducing the Mn valence.[244] Another explanation in the subtle changes in the pre-peak region of the O-K edge at the step edge, could be chemical intermixing between Cu and Mn cations as indicated in Figure 51c and Figure 52.
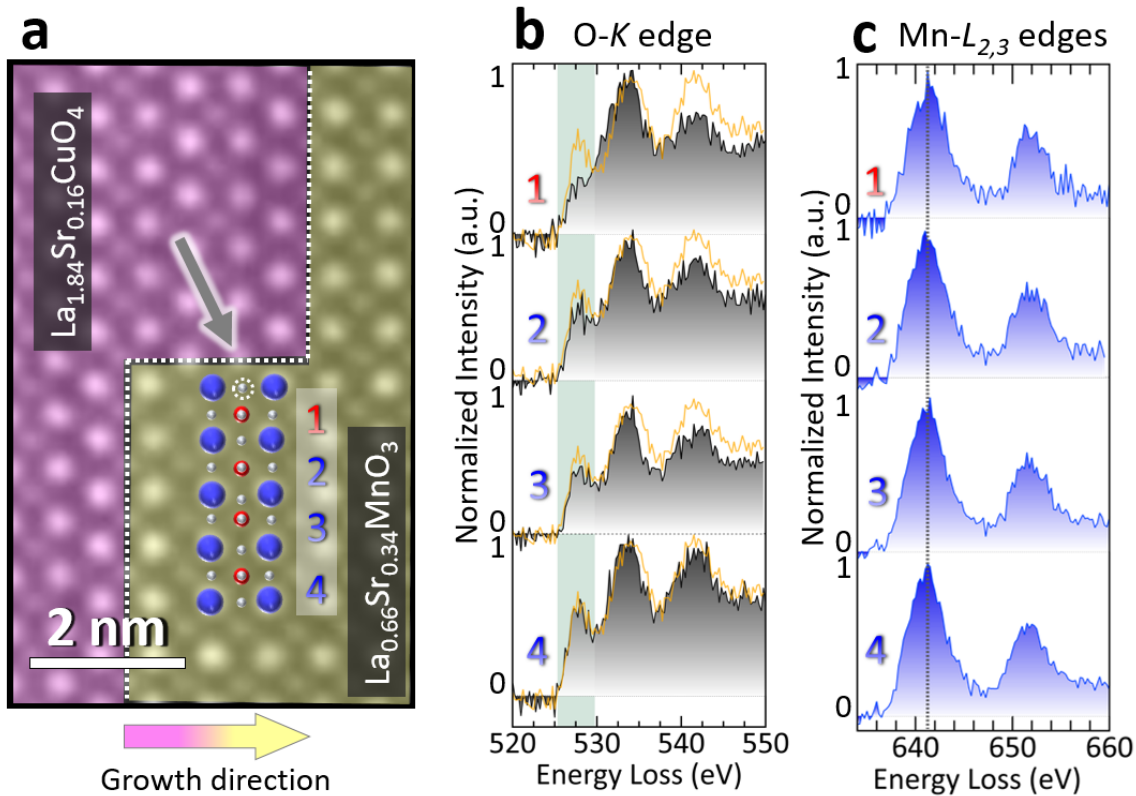
Figure 55: Insights into the electronic structure at the step edge. (a) HAADF image highlighting a step edge of the LSCO-LSMO interface with dashed white lines. The blue numbers denote the Mn atoms outside of the deformed unit cell and the red number denotes the position of the LSMO unit cells, which is in direct proximity to the step edge. (b) Atomically resolved ELNES of the four LSMO unit cells performed on the pre-edge region of the O-K edge with the reference LSMO O-K edge obtained from the center of the sample as an orange profile. (c) Similar analysis utilizing the Mn-$L_{2,3}$ edges for each of the four LSMO unit cells. This figure has been reproduced with permission from *Bonmassar et al.*[221]

Yet, the complexity of this scenario amplifies given the role of the LSCO layer, acting as an in-plane compressive force upon the LSMO layer. This interplay of tensile and compressive strains at the step edge gives rise to a characteristic electronic structure, distinct from either strain in isolation. Therefore, we compared the pre-edge region of the center of our LSMO layer (orange profile) to directly compare each of the four assigned unit cells with layers farther away from the interfaces to LSCO and LCO. Our results show that the first three unit cells in direct proximity to the step edge have reduced pre-peaks and overall O-K edges, whereas the fourth unit cell shows a pre-peak and O-K edge of a similar height than in the center part of our LSMO layer, which is in agreement with the locally strained step edge region. The effect of strain on the physical properties originating from the substrate has been reported and discussed elsewhere.[169] Note that, within the experimental energy resolution and signal-to-noise ratio in our atomically resolved EELS measurements, we can not resolve the subtle peak shifts in the Mn-L_3 edge, c.f. Figure 55c. As a result, these nuanced shifts in the edge could not be accurately resolved or characterized in terms of an L_3/L_2 ratio analysis, which needs a sufficient signal-to-noise ratio. However, our fine structure analyses in the pre-peak of the O-K edge indicate either the reduced oxidation states of the Mn atoms at the step edge via the formation of oxygen vacancies, or the mixing of Cu and Mn atoms leading to distorted unit cells, consistent with the pronounced lattice distortions observed in our strain maps in Figure 54b, c.

5.7 Defect-free Sample

In materials characterized by minimal lattice mismatches, localized step edge defects are absent, as indicated in Figure 56. This is in stark contrast to the prior LSCO-LSMO-LCO trilayer exhibiting significant lattice disparities. Particularly, the examination of LSCO and $LaSrMnO_4$ bilayers with tetragonal 214 crystal structure grown on an (001) oriented LSAO substrate with a 15° offcut towards the a-axis, distinguished by a mere 2 pm difference in c-axis values,[93] reveals an absence of detected defects, underscoring the role of lattice coherence in influencing the formation of defects. Utilizing a 15° offcut angle for the LSAO substrate ensures identical conditions to those governing the LSCO-LSMO-LCO trilayer within our experimental setup.
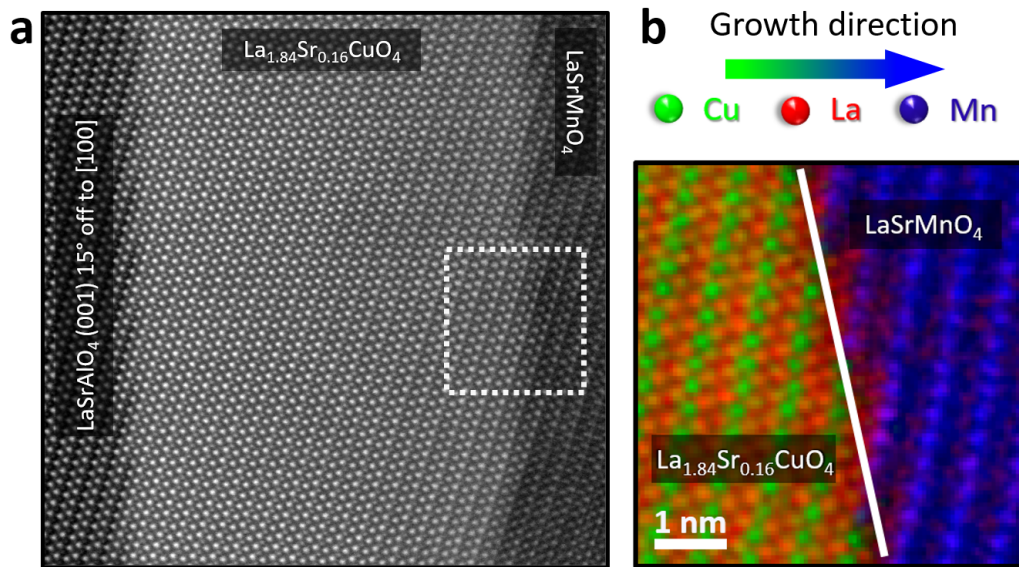
Figure 56: Unveiling coherent interfaces with structurally congruent materials. (a) HAADF overview image delineating the bilayer structure. The first interface is the LSAO substrate (dark contrast on the left side) next to the LSCO (bright contrast in the middle), positioned in the middle of the image. The second LSCO-$LaSrMnO_4$ interface (dark contrast on the right-hand side) is depicted on the right-hand side. The white square showcases the area for the EELS elemental mapping. (b) Atomically resolved EELS elemental mapping with La in red, Cu in green, and Mn in blue shows the high chemical quality of the bilayer system. The white line highlights the interface between the cuprate and the manganite layer. This figure has been reproduced with permission from *Bonmassar et al.*[221]

The absence of defect formations is further demonstrated by atomically resolved EELS elemental mappings in Figure 56b. In this context, the interface reveals a striking degree of crystallographic and chemical coherence, underscoring the pristine structural integrity of the studied system. The structural coherence exhibited by the LSCO-$LaSrMnO_4$ interface holds promise for the realization of in-plane devices, particularly regarding high-T_C Josephson junctions. This potential arises from the notably elevated in-plane coherence length of the Cooper pairs in oxide high-T_C materials, about 2.4 nm, notably greater than the corresponding out-of-plane coherence length of a mere 0.3 nm.[91] This structural attribute enhances the feasibility of manufacturing high-performance in-plane devices. Herein, the alignment of the materials' crystalline axes facilitates efficient Cooper pair transport, thereby promoting the effective pinning of vortices and facilitating the manifestation of Josephson junctions, thus, holding promise for advanced device architectures.

5.8 Discussion

Utilizing the geometric attributes of precise offcut substrates coupled with the unique advantages offered by layer-by-layer growth through oxide MBE, we present a compelling demonstration of defect trapping at the sub-nanometer scale. We observed that these step edge-induced defects are localized and do not penetrate the bulk of the subsequent thin film. We attribute this defect trapping to the pronounced c-axis mismatch between the bottom and top epitaxial layers. The formation of defects induces structural re-arrangements at the sub-nanometer scale, consequently introducing novel chemical and electronic properties in these localized regions. This allows tuning of the electrical transport properties, as ferroelectricity is known to be induced by tensile strained $SrTiO_3$.[245] The discernible local spectral variations, characterized by employing atomic resolution STEM imaging and high-resolution EELS, offer insights into the complex interplay between electronic states and strain at step edges. These controllable defects thus stand as a promising tool for avoiding the formation of 2D defects, such as APBs. Notably, the control over APBs holds a profound role in catalysis, given their potential to significantly influence surface reactivity, adsorption, and overall catalytic performance.[225,226] The prevention of APB formation in bulk benefits both fundamental science and practical applications that may underpin critical technological advancements. The formation of localized defects and the prevention of APBs in the subsequent thin film layer benefit fundamental science and practical applications that may underpin critical technological advancements.

6 Outlook and Future Advancements in Terrace-by-Terrace Growth

6.1 Summary and Objectives

The first study highlights the effectiveness of epitaxial engineering in manipulating spectral weight transfer within a sample, specifically from the UHB to in-plane or out-of-plane hole states and back to the UHB. Through STEM-EELS analysis, we achieve atomic-scale visualization of hole positions in CuO planes, distinguishing between insulating, metallic, and superconducting states. This precise localization of holes provides valuable insights for the characterization of heteroepitaxial or intrinsic Josephson junctions, especially in the context of oxide-based superconducting spintronics. The outlook suggests the potential application of these findings in advancing the understanding and development of correlated systems and Josephson junctions.

While materials with similar crystallographic a- and b-axes may structurally match at the epitaxial interface, this doesn't ensure chemical perfection, the absence of defects, or the required apical oxygen spacing, which is crucial for properties such as superconductivity. The first layers of superconducting materials on substrates are often referred to as 'dead layers' due to their lack of superconductivity. This is particularly important in oxide-based superconductors, where the coherence lengths are smaller than in metallic superconductors. Minimizing the chemical potential at the interface is crucial for the realization of high-T_C oxide-based superconducting spintronics in the future. Therefore, this study highlights the need to address these challenges and how to overcome them for the advancement of oxide-based superconducting spintronics.

Finally, future studies on offcut substrates are promising as we introduce a novel bi-directional growth model for the design of innovative quantum materials. Building on the findings of previous sections, the integration of state-of-the-art growth techniques, such as MBE, and advanced characterization techniques, such as STEM-EELS, has led to a breakthrough discovery. In particular, the identification of step-edge-induced geometric anisotropies paves the way for understanding and exploiting anisotropic physical properties in quantum materials.

The impact of this work is given by the presentation of a newly discovered growth model, i.e. bi-directional growth, but also by the unique combination of designing new materials in the MBE and the ability to control the grown samples at the atomic scale using state-of-the-art electron microscopy. This allowed us to identify interfacial defects at the atomic level and their absence in the subsequent thin film material. Therefore, we hope that thin film growers and microscopists with a focus on materials science will find this work helpful as a starting point for their discoveries.

6.2 Offcut Substrate-Induced Tailoring of Thin Film Architectures

Recent research efforts have made remarkable breakthroughs in materials science, particularly in the areas of thin film growth and defect engineering. Our approach using terrace-by-trace growth with *in situ* RHEED has opened an opportunity for precise control of ferromagnetic and superconducting properties in two crystallographic dimensions. The uniform terrace widths lead to controlled and coherent growth along both axes. A key aspect of our research is the creation of tailored thin film architectures with previously

unattainable functionalities. Our success in fabricating a SL composed of five bilayers of $(SMO)_4$ - $(LMO)_4$ demonstrates the transformative potential of our novel growth technique. By carefully modulating the in-plane and out-of-plane orbital occupancy, we have transformed an insulating material (with a nominal layer thickness of $n = 4$ and a SMO:LMO ratio of 1:1) into a ferromagnetic metal. This transition represents a leap in our ability to design materials with tailored magnetic properties, with implications for spintronics and magnetic storage.

6.3 Anisotropic Superconducting Homojunctions

Using our atomically precise growth technique, we have grown superconducting thin films, leading to the formation of anisotropic superconducting homojunctions. These junctions exhibit two distinct mechanisms: first, the intrinsic Josephson effect facilitated by c-axis tunneling across the terraces; and second, the creation of superconducting stripes, which are less than 30 nm wide. This quantum confinement effect is effectively forming a weak link. Future investigations will explore the fundamental physics underlying these phenomena, to exploit them for applications in quantum computing and high-performance electronics.

6.4 Defect Trapping at Step Edges

Our results showed the localized formation of defects at the step edge leading to a relaxation of the following thin film layers and the prohibition of antiphase boundaries, which do form at the step edge in non-offcut substrates with high lattice mismatches. In a three-layer oxide heterostructure grown on an LSAO offcut substrate, we observed the formation of localized defects resulting from a small a-axis mismatch (0.11 Å) and a more pronounced c-axis mismatch (2.73 Å) at the step edges. Atomically resolved EELS maps have provided invaluable insights into the electronic states of these defects, giving hints for the formation of oxygen vacancies in parallel with the prohibition of antiphase boundaries in the subsequent bulk thin film.

Potential industrial applications of this work could be that antiphase boundary-free thin films are critical for semiconductor manufacturing, where uniform crystal structures contribute to improved electronic properties, leading to enhanced device performance and reliability. In addition, in optoelectronic devices such as light-emitting diodes and photodetectors, the absence of antiphase boundaries ensures uniformity of material properties leading to improved optical performances. Another application could be the insertion of a two-unit cell thick sacrificial layer before the deposition of the thick and antiphase boundary-free material of interest.

6.5 Future Directions of Offcut Technologies

The future of controlled terrace-by-terrace growth is full of exciting possibilities. First, we anticipate further advances in our terrace-by-terrace growth technique, extending its application to a wider range of material systems and exploring its scalability for industrial use. We also suggest an in-depth exploration of the potential applications of anisotropic superconducting homojunctions, with a strong focus on quantum technologies. High-temperature superconducting devices hold great promise for industrial applications as they have the potential to revolutionize electronics, power transmission, and medical imaging by enabling the transport of electrical currents without resistance, leading to

energy efficiency and novel technologies.

Defect engineering remains a promising area for future investigation. The control and manipulation of defect formation at the nanoscale opens up new areas of research for tailoring materials with unprecedented electronic, magnetic, and catalytic properties.

In conclusion, this recent discovery of simultaneous in-plane and out-of-plane orbital control has not only expanded our understanding of thin film growth and defect engineering but has also set the stage for future innovations in materials science and technology. The future of this research is rich in possibilities and promises to open up unprecedented opportunities for the development of cuprate-based **high T_C superconducting diodes** or **high-performance Peltier elements** by introducing atomically engineered **in-plane thermoelectric and superconducting heterostructures** for sub-T_C cooling, potentially enabling the use of quantum devices at room temperature. Unlocking the full potential of layered oxides through in-plane and out-of-plane orbital bonding between two different materials is the key to discoveries for both fundamental research and industrial purposes.

List of Figures

References

1. Baibich, M. N., Broto, J. M., Fert, A., van Nguyen, D. F., Petroff, F., Etienne, P., Creuzet, G., Friederich, A. & Chazelas, J. Giant magnetoresistance of (001)Fe/(001)Cr magnetic superlattices. *Physical Review Letters* **61,** 2472–2475 (1988).

2. Binasch, G., Grünberg, P., Saurenbach, F. & Zinn, W. Enhanced magnetoresistance in layered magnetic structures with antiferromagnetic interlayer exchange. *Physical Review. B* **39,** 4828–4830. ISSN: 0163-1829 (1989).

3. Jonker, G. H. & van Santen, J. H. Ferromagnetic compounds of manganese with perovskite structure. *Physica* **16,** 337–349. ISSN: 00318914 (1950).

4. Bednorz, J. G. & Mller, K. A. Possible high-T_C superconductivity in the Ba-La-Cu-O system. *Zeitschrift fr Physik B Condensed Matter* **64,** 189–193. ISSN: 0722-3277 (1986).

5. Wu, M. K., Ashburn, Torng, C. J., Hor, P. H., Meng, R. L., Gao, L., Huang, Z. J., Wang, Y. Q. & Chu, C. W. Superconductivity at 93 K in a new mixed-phase Yb-Ba-Cu-O compound system at ambient pressure. *Physical Review Letters* **58,** 908–910 (1987).

6. Josephson, B. D. Possible new effects in superconductive tunnelling. *Physics Letters* **1,** 251–253. ISSN: 00319163 (1962).

7. Golubov, A. A., Kupriyanov, M. Y. & Il'ichev, E. The current-phase relation in Josephson junctions. *Reviews of Modern Physics* **76,** 411–469. ISSN: 0034-6861 (2004).

8. Mannhart, J. & Schlom, D. G. Oxide interfaces-an opportunity for electronics. *Science* **327,** 1607–1611 (2010).

9. Ramesh, R. & Schlom, D. G. Creating emergent phenomena in oxide superlattices. *Nature Reviews Materials* **4,** 257–268 (2019).

10. Johnson, M. & Silsbee, R. H. Interfacial charge-spin coupling: Injection and detection of spin magnetization in metals. *Physical Review Letters* **55,** 1790–1793 (1985).

11. Han, W., Otani, Y. & Maekawa, S. Quantum materials for spin and charge conversion. *npj Quantum Materials* **3** (2018).

12. Williams, R. Becquerel Photovoltaic Effect in Binary Compounds. *The Journal of Chemical Physics* **32,** 1505–1514. ISSN: 0021-9606 (1960).

13. O'Regan, B. & Grätzel, M. A low-cost, high-efficiency solar cell based on dye-sensitized colloidal TiO_2 films. *Nature* **353,** 737–740 (1991).

14. Reyren, N., Thiel, S., Caviglia, A. D., Kourkoutis, L. F., Hammerl, G., Richter, C., Schneider, C. W., Kopp, T., Rüetschi, A.-S., Jaccard, D., Gabay, M., Muller, D. A., Triscone, J.-M. & Mannhart, J. Superconducting interfaces between insulating oxides. *Science* **317,** 1196–1199 (2007).

15. Dagotto, E. Complexity in strongly correlated electronic systems. *Science* **309,** 257–262 (2005).

16. Park, D.-S., Rata, A. D., Maznichenko, I. V., Ostanin, S., Gan, Y. L., Agrestini, S., Rees, G. J., Walker, M., Li, J., Herrero-Martin, J., Singh, G., Luo, Z., Bhatnagar, A., Chen, Y. Z., Tileli, V., Muralt, P., Kalaboukhov, A., Mertig, I., Dörr, K., Ernst, A. & Pryds, N. The emergence of magnetic ordering at complex oxide interfaces tuned by defects. *Nature Communications* **11,** 3650 (2020).

17. Imada, M., Fujimori, A. & Tokura, Y. Metal-insulator transitions. *Reviews of Modern Physics* **70,** 1039–1263. ISSN: 0034-6861 (1998).

18. Sun, H. Y., Mao, Z. W., Zhang, T. W., Han, L., Zhang, T. T., Cai, X. B., Guo, X., Li, Y. F., Zang, Y. P., Guo, W., Song, J. H., Ji, D. X., Gu, C. Y., Tang, C., Gu, Z. B., Wang, N., Zhu, Y., Schlom, D. G., Nie, Y. F. & Pan, X. Q. Chemically specific termination control of oxide interfaces via layer-by-layer mean inner potential engineering. *Nature Communications* **9,** 2965 (2018).

19. Klitzing, K. v., Dorda, G. & Pepper, M. New Method for High-Accuracy Determination of the Fine-Structure Constant Based on Quantized Hall Resistance. *Physical Review Letters* **45,** 494–497. ISSN: 0031-9007 (1980).

20. J. Hubbard. Electron correlations in narrow energy bands. *Proceedings of the Royal Society of London. Series A. Mathematical and Physical Sciences* **276,** 238–257. ISSN: 0080-4630 (1963).

21. Zaanen, J., Sawatzky, G. A. & Allen, J. W. Band gaps and electronic structure of transition-metal compounds. *Physical Review Letters* **55,** 418–421 (1985).

22. Bardeen, J., Cooper, L. N. & Schrieffer, J. R. Microscopic Theory of Superconductivity. *Physical Review* **106,** 162–164. ISSN: 0031-899X (1957).

23. Nakajima, H., Kurushima, K., Mine, S., Tsukasaki, H., Matsuoka, M., Gao, B., Cheong, S.-W. & Mori, S. Charged domain boundaries stabilized by translational symmetry breaking in the hybrid improper ferroelectric $Ca_{3-x}Sr_xTi_2O_7$. *Communications Materials* **2** (2021).

24. Tian, H., Verbeeck, J., Brück, S., Paul, M., Kufer, D., Sing, M., Claessen, R. & van Tendeloo, G. Interface-induced modulation of charge and polarization in thin film Fe_3O_4. *Advanced Materials* **26,** 461–465 (2014).

25. Lotnyk, A., Ross, U., Bernütz, S., Thelander, E. & Rauschenbach, B. Local atomic arrangements and lattice distortions in layered Ge-Sb-Te crystal structures. *Scientific Reports* **6,** 26724 (2016).

26. Crewe, A. V., Wall, J. & Langmore, J. Visibility of single atoms. *Science* **168,** 1338–1340 (1970).

27. Krivanek, O. L., Chisholm, M. F., Nicolosi, V., Pennycook, T. J., Corbin, G. J., Dellby, N., Murfitt, M. F., Own, C. S., Szilagyi, Z. S., Oxley, M. P., Pantelides, S. T. & Pennycook, S. J. Atom-by-atom structural and chemical analysis by annular dark-field electron microscopy. *Nature* **464,** 571–574 (2010).

28. Shin, D. H., Kirkland, E. J. & Silcox, J. Annular dark field electron microscope images with better than 2 Å resolution at 100 kV. *Applied Physics Letters* **55,** 2456–2458. ISSN: 0003-6951 (1989).

29. Reyren, N., Thiel, S., Caviglia, A. D., Kourkoutis, L. F., Hammerl, G., Richter, C., Schneider, C. W., Kopp, T., Rüetschi, A.-S., Jaccard, D., Gabay, M., Muller, D. A., Triscone, J.-M. & Mannhart, J. Superconducting interfaces between insulating oxides. *Science* **317,** 1196–1199 (2007).

30. Ramasse, Q. M., Seabourne, C. R., Kepaptsoglou, D.-M., Zan, R., Bangert, U. & Scott, A. J. Probing the bonding and electronic structure of single atom dopants in graphene with electron energy loss spectroscopy. *Nano Letters* **13,** 4989–4995 (2013).

31. Rose, H. H. Optics of high-performance electron microscopes. *Science and Technology of Advanced Materials* **9,** 014107 (2008).

32. Shibata, N., Kohno, Y., Nakamura, A., Morishita, S., Seki, T., Kumamoto, A., Sawada, H., Matsumoto, T., Findlay, S. D. & Ikuhara, Y. Atomic resolution electron microscopy in a magnetic field free environment. *Nature Communications* **10,** 2308 (2019).

33. Zachman, M. J., Tu, Z., Choudhury, S., Archer, L. A. & Kourkoutis, L. F. Cryo-STEM mapping of solid-liquid interfaces and dendrites in lithium-metal batteries. *Nature* **560,** 345–349 (2018).

34. Pennycook, S. J. The impact of STEM aberration correction on materials science. *Ultramicroscopy* **180,** 22–33. ISSN: 0304-3991 (2017).

35. Pan, G. A., Ferenc Segedin, D., LaBollita, H., Song, Q., Nica, E. M., Goodge, B. H., Pierce, A. T., Doyle, S., Novakov, S., Córdova Carrizales, D., N'Diaye, A. T., Shafer, P., Paik, H., Heron, J. T., Mason, J. A., Yacoby, A., Kourkoutis, L. F., Erten, O., Brooks, C. M., Botana, A. S. & Mundy, J. A. Superconductivity in a quintuple-layer square-planar nickelate. *Nature Materials* **21,** 160–164 (2022).

36. Mundy, J. A., Brooks, C. M., Holtz, M. E., Moyer, J. A., Das, H., Rébola, A. F., Heron, J. T., Clarkson, J. D., Disseler, S. M., Liu, Z., Farhan, A., Held, R., Hovden, R., Padgett, E., Mao, Q., Paik, H., Misra, R., Kourkoutis, L. F., Arenholz, E., Scholl, A., Borchers, J. A., Ratcliff, W. D., Ramesh, R., Fennie, C. J., Schiffer, P., Muller, D. A. & Schlom, D. G. Atomically engineered ferroic layers yield a room-temperature magnetoelectric multiferroic. *Nature* **537,** 523–527 (2016).

37. Logvenov, G., Gozar, A. & Bozovic, I. High-temperature superconductivity in a single copper-oxygen plane. *Science* **326,** 699–702 (2009).

38. Naito, M. & Sato, H. Stoichiometry control of atomic beam fluxes by precipitated impurity phase detection in growth of $(Pr,Ce)_2CuO_4$ and $(La,Sr)_2CuO_4$ films. *Applied Physics Letters* **67,** 2557–2559. ISSN: 0003-6951 (1995).

39. Mannhart, J. & Schlom, D. G. Oxide interfaces–an opportunity for electronics. *Science* **327,** 1607–1611 (2010).

40. Schlom, D. G. Perspective: Oxide molecular-beam epitaxy rocks! *APL Materials* **3,** 062403 (2015).

41. Suyolcu, Y. E., Christiani, G., van Aken, P. A. & Logvenov, G. Design of Complex Oxide Interfaces by Oxide Molecular Beam Epitaxy. *Journal of Superconductivity and Novel Magnetism* **33,** 107–120. ISSN: 1557-1939 (2020).

42. Gozar, A. & Bozovic, I. High temperature interface superconductivity. *Physica C: Superconductivity and its Applications* **521-522,** 38–49. ISSN: 09214534 (2016).

43. Koida, T., Lippmaa, M., Fukumura, T., Itaka, K., Matsumoto, Y., Kawasaki, M. & Koinuma, H. Effect of A-site cation ordering on the magnetoelectric properties in $[(LaMnO_3)_m / (SrMnO_3)_m]_n$ artificial superlattices. *Physical Review B* **66.** ISSN: 0163-1829 (2002).

44. Bhattacharya, A., May, S. J., te Velthuis, S. G. E., Warusawithana, M., Zhai, X., Jiang, B., Zuo, J.-M., Fitzsimmons, M. R., Bader, S. D. & Eckstein, J. N. Metal-insulator transition and its relation to magnetic structure in $(LaMnO_3)_{2n}/(SrMnO_3)_n$ superlattices. *Physical Review Letters* **100,** 257203. ISSN: 0031-9007 (2008).

45. Suyolcu, Y. E., Christiani, G., Gemperline, P. T., Provence, S. R., Bussmann-Holder, A., Comes, R. B., van Aken, P. A. & Logvenov, G. Engineering ordered arrangements of oxygen vacancies at the surface of superconducting La_2CuO_4 thin films. *Journal of Vacuum Science & Technology A* **40,** 013214. ISSN: 0734-2101 (2022).

46. Gozar, A., Logvenov, G., Kourkoutis, L. F., Bollinger, A. T., Giannuzzi, L. A., Muller, D. A. & Bozovic, I. High-temperature interface superconductivity between metallic and insulating copper oxides. *Nature* **455,** 782–785 (2008).

47. Kim, G., Khaydukov, Y., Bluschke, M., Suyolcu, Y. E., Christiani, G., Son, K., Dietl, C., Keller, T., Weschke, E., van Aken, P. A., Logvenov, G. & Keimer, B. Tunable perpendicular exchange bias in oxide heterostructures. *Physical Review Materials* **3** (2019).

48. Gupta, C., Parab, P. & Bose, S. Superfluid density from magnetic penetration depth measurements in Nb-Cu 3D nano-composite films. *Scientific Reports* **10,** 18331 (2020).

49. Cao, Y., Fatemi, V., Fang, S., Watanabe, K., Taniguchi, T., Kaxiras, E. & Jarillo-Herrero, P. Unconventional superconductivity in magic-angle graphene superlattices. *Nature* **556,** 43–50 (2018).

50. Törmä, P., Peotta, S. & Bernevig, B. A. Superconductivity, superfluidity and quantum geometry in twisted multilayer systems. *Nature Reviews Physics* **4,** 528–542 (2022).

51. Scalapino, D. J. A common thread: The pairing interaction for unconventional superconductors. *Reviews of Modern Physics* **84,** 1383–1417. ISSN: 0034-6861 (2012).

52. Keimer, B., Kivelson, S. A., Norman, M. R., Uchida, S. & Zaanen, J. From quantum matter to high-temperature superconductivity in copper oxides. *Nature* **518,** 179–186 (2015).

53. Hashimoto, M., Vishik, I. M., He, R.-H., Devereaux, T. P. & Shen, Z.-X. Energy gaps in high-transition-temperature cuprate superconductors. *Nature Physics* **10,** 483–495. ISSN: 1745-2473 (2014).

54. Bednorz, J. G. & Müller, K. A. Possible high-T_C superconductivity in the Ba-La-Cu-O system. *Zeitschrift für Physik B Condensed Matter* **64,** 189–193. ISSN: 0722-3277 (1986).

55. Hwang, H. Y., Iwasa, Y., Kawasaki, M., Keimer, B., Nagaosa, N. & Tokura, Y. Emergent phenomena at oxide interfaces. *Nature Materials* **11,** 103–113 (2012).

56. Sanchez-Manzano, D., Mesoraca, S., Cuellar, F. A., Cabero, M., Rouco, V., Orfila, G., Palermo, X., Balan, A., Marcano, L., Sander, A., Rocci, M., Garcia-Barriocanal, J., Gallego, F., Tornos, J., Rivera, A., Mompean, F., Garcia-Hernandez, M., Gonzalez-Calbet, J. M., Leon, C., Valencia, S., Feuillet-Palma, C., Bergeal, N., Buzdin, A. I., Lesueur, J., Villegas, J. E. & Santamaria, J. Extremely long-range, high-temperature Josephson coupling across a half-metallic ferromagnet. *Nature Materials* **21,** 188–194. ISSN: 1476-1122 (2022).

57. Reyren, N., Thiel, S., Caviglia, A. D., Kourkoutis, L. F., Hammerl, G., Richter, C., Schneider, C. W., Kopp, T., Rüetschi, A.-S., Jaccard, D., Gabay, M., Muller, D. A., Triscone, J.-M. & Mannhart, J. Superconducting interfaces between insulating oxides. *Science* **317,** 1196–1199 (2007).

58. Liu, F.-s. Advantages of High-Tc Cuprates over Semiconductors for Making Room Temperature Electronic Devices. *Journal of Superconductivity and Novel Magnetism* **25,** 215–219. ISSN: 1557-1939 (2012).

59. Cai, R., Yao, Y., Lv, P., Ma, Y., Xing, W., Li, B., Ji, Y., Zhou, H., Shen, C., Jia, S., Xie, X. C., Žutić, I., Sun, Q.-F. & Han, W. Evidence for anisotropic spin-triplet Andreev reflection at the 2D van der Waals ferromagnet/superconductor interface. *Nature Communications* **12,** 6725 (2021).

60. Ioffe, L. B., Geshkenbein, V. B., Feigel'man, M. V., Fauchère, A. L. & Blatter, G. Environmentally decoupled sds -wave Josephson junctions for quantum computing. *Nature* **398,** 679–681. ISSN: 0028-0836 (1999).

61. Visani, C., Tornos, J., Nemes, N. M., Rocci, M., Leon, C., Santamaria, J., te Velthuis, S. G. E., Liu, Y., Hoffmann, A., Freeland, J. W., Garcia-Hernandez, M., Fitzsimmons, M. R., Kirby, B. J., Varela, M. & Pennycook, S. J. Symmetrical interfacial reconstruction and magnetism in $La_{0.7}Ca_{0.3}MnO_3/YBa_2Cu_3O_7/La_{0.7}Ca_{0.3}MnO_3$ heterostructures. *Physical Review B* **84.** ISSN: 1098-0121 (2011).

62. Charaev, I., Bandurin, D. A., Bollinger, A. T., Phinney, I. Y., Drozdov, I., Colangelo, M., Butters, B. A., Taniguchi, T., Watanabe, K., He, X., Medeiros, O., Božović, I., Jarillo-Herrero, P. & Berggren, K. K. Single-photon detection using high-temperature superconductors. *Nature Nanotechnology* **18,** 343–349 (2023).

63. Merino, R. L., Seifert, P., Retamal, J. D., Mech, R. K., Taniguchi, T., Watanabe, K., Kadowaki, K., Hadfield, R. H. & Efetov, D. K. Two-dimensional cuprate nanodetector with single telecom photon sensitivity at T = 20 K. *2D Materials* **10,** 021001 (2023).

64. Polakovic, T., Armstrong, W., Karapetrov, G., Meziani, Z.-E. & Novosad, V. Unconventional Applications of Superconducting Nanowire Single Photon Detectors. *Nanomaterials* **10.** ISSN: 2079-4991 (2020).

65. Kurokawa, K., Isono, S., Kohama, Y., Kunisada, S., Sakai, S., Sekine, R., Okubo, M., Watson, M. D., Kim, T. K., Cacho, C., Shin, S., Tohyama, T., Tokiwa, K. & Kondo, T. Unveiling phase diagram of the lightly doped high-Tc cuprate superconductors with disorder removed. *Nature Communications* **14,** 4064 (2023).

66. Fradkin, E., Kivelson, S. A. & Tranquada, J. M. Colloquium: Theory of intertwined orders in high temperature superconductors. *Reviews of Modern Physics* **87,** 457–482. ISSN: 0034-6861 (2015).

67. Zhang, X., Catlow, C., Parker, S. C. & Wall, A. Simulation study of pressure-induced structural changes in La_2CuO_4 and in $La_{1.84}Sr_{0.16}CuO_4$. *Journal of Physics and Chemistry of Solids* **53,** 761–770. ISSN: 00223697 (1992).

68. Kamimura, H. *Theory of copper oxide superconductors* ISBN: 978-3-540-25189-7 (Springer, Berlin and New York, 2005).

69. Momma, K. & Izumi, F. VESTA 3 for three-dimensional visualization of crystal, volumetric and morphology data. *Journal of Applied Crystallography* **44,** 1272–1276. ISSN: 0021-8898 (2011).

70. Locquet, J., Jaccard, Y., Cretton, A., Williams, E. J., Arrouy, F., Mächler, E., Schneider, T., Fischer, O. & Martinoli, P. Variation of the in-plane penetration depth lambda ab as a function of doping in $La_{2-x}Sr_xCuO_{4\pm d}$ thin films on $SrTiO_3$: Implications for the overdoped state. *Physical Review. B* **54,** 7481–7488. ISSN: 0163-1829 (1996).

71. Suyolcu, Y. E., Wang, Y., Sigle, W., Baiutti, F., Cristiani, G., Logvenov, G., Maier, J. & van Aken, P. A. Octahedral Distortions at High-Temperature Superconducting La_2CuO_4 Interfaces: Visualizing Jahn-Teller Effects. *Advanced Materials Interfaces* **4,** 1700737. ISSN: 21967350 (2017).

72. Findlay, S. D., Shibata, N., Sawada, H., Okunishi, E., Kondo, Y., Yamamoto, T. & Ikuhara, Y. Robust atomic resolution imaging of light elements using scanning transmission electron microscopy. *Applied Physics Letters* **95.** ISSN: 0003-6951 (2009).

73. Okunishi, E., Ishikawa, I., Sawada, H., Hosokawa, F., Hori, M. & Kondo, Y. Visualization of Light Elements at Ultrahigh Resolution by STEM Annular Bright Field Microscopy. *Microscopy and Microanalysis* **15,** 164–165. ISSN: 1431-9276 (2009).

74. Zhang & Rice. Effective Hamiltonian for the superconducting Cu oxides. *Physical Review. B* **37,** 3759–3761. ISSN: 0163-1829 (1988).

75. Lane, C. & Zhu, J.-X. Landscape of coexisting excitonic states in the insulating single-layer cuprates and nickelates. *Physical Review B* **101.** ISSN: 2469-9950 (2020).

76. Li, N., Bediako, D. K., Hadt, R. G., Hayes, D., Kempa, T. J., von Cube, F., Bell, D. C., Chen, L. X. & Nocera, D. G. Influence of iron doping on tetravalent nickel content in catalytic oxygen evolving films. *Proceedings of the National Academy of Sciences of the United States of America* **114,** 1486–1491 (2017).

77. Chen, Sette, Ma, Hybertsen, Stechel, Foulkes, Schulter, Cheong, Cooper, Rupp, Batlogg, Soo, Ming, Krol & Kao. Electronic states in $La_{2-x}Sr_xCuO_{4+\delta}$ probed by soft-x-ray absorption. *Physical Review Letters* **66,** 104–107. ISSN: 0031-9007 (1991).

78. Baldini, M., Muramatsu, T., Sherafati, M., Mao, H.-k., Malavasi, L., Postorino, P., Satpathy, S. & Struzhkin, V. V. Origin of colossal magnetoresistance in $LaMnO_3$ manganite. *Proceedings of the National Academy of Sciences of the United States of America* **112,** 10869–10872 (2015).

79. Zurauskiene, N., Stankevic, V., Kersulis, S., Vagner, M., Plausinaitiene, V., Dobilas, J., Vasiliauskas, R., Skapas, M., Koliada, M., Pietosa, J. & Wisniewski, A. Enhancement of Room-Temperature Low-Field Magnetoresistance in Nanostructured Lanthanum Manganite Films for Magnetic Sensor Applications. *Sensors* **22** (2022).

80. Acevedo, W. R., Rubi, D., Lecourt, J., Lüders, U., Gomez-Marlasca, F., Granell, P., Golmar, F. & Levy, P. Manganite-based three level memristive devices with self-healing capability. *Physics Letters A* **380,** 2870–2875. ISSN: 03759601 (2016).

81. Orfila, G., Sanchez-Manzano, D., Arora, A., Cuellar, F., Ruiz-Gómez, S., Rodriguez-Corvillo, S., López, S., Peralta, A., Carreira, S. J., Gallego, F., Tornos, J., Rouco, V., Riquelme, J. J., Munuera, C., Mompean, F. J., Garcia-Hernandez, M., Sefrioui, Z., Villegas, J. E., Perez, L., Rivera-Calzada, A., Leon, C., Valencia, S. & Santamaria, J. Large Magnetoresistance of Isolated Domain Walls in $La_{2/3}Sr_{1/3}$ MnO_3 Nanowires. *Advanced Materials,* e2211176 (2023).

82. Goldschmidt, V. M. Die Gesetze der Krystallochemie. *Die Naturwissenschaften* **14,** 477–485. ISSN: 0028-1042 (1926).

83. Chmaissem, O., Dabrowski, B., Kolesnik, S., Mais, J., Jorgensen, J. D. & Short, S. Structural and magnetic phase diagrams of $La_{1-x}Sr_xMnO_3$ and $Pr_{1-y}Sr_yMnO_3$. *Physical Review. B* **67.** ISSN: 0163-1829 (2003).

84. Tezuka, K., Inamura, M., Hinatsu, Y., Shimojo, Y. & Morii, Y. Crystal Structures and Magnetic Properties of $Ca_{2-x}Sr_xMnO_4$. *Journal of Solid State Chemistry* **145,** 705–710. ISSN: 00224596 (1999).

85. Mitchell, J. F., Millburn, J. E., Medarde, M., Short, S., Jorgensen, J. D. & T., F. D. M. $Sr_3Mn_2O_7$: Mn^{4+} Parent Compound of the n=2 Layered CMR Manganites. *Journal of Solid State Chemistry* **141,** 599–603. ISSN: 00224596 (1998).

86. Hadermann, J., Abakumov, A. M., Tsirlin, A. A., Rozova, M. G., Sarakinou, E. & Antipov, E. V. Expanding the Ruddlesden-Popper manganite family: the N = 3 $La_{3.2}Ba_{0.8}Mn_3O_{10}$ member. *Inorganic Chemistry* **51,** 11487–11492 (2012).

87. Ferenc Segedin, D., Goodge, B. H., Pan, G. A., Song, Q., LaBollita, H., Jung, M.-C., El-Sherif, H., Doyle, S., Turkiewicz, A., Taylor, N. K., Mason, J. A., N'Diaye, A. T., Paik, H., El Baggari, I., Botana, A. S., Kourkoutis, L. F., Brooks, C. M. & Mundy, J. A. Limits to the strain engineering of layered square-planar nickelate thin films. *Nature Communications* **14,** 1468 (2023).

88. Fleck, E. E., Barone, M. R., Nair, H. P., Schreiber, N. J., Dawley, N. M., Schlom, D. G., Goodge, B. H. & Kourkoutis, L. F. Atomic-Scale Mapping and Quantification of Local Ruddlesden-Popper Phase Variations. *Nano Letters* **22,** 10095–10101 (2022).

89. Hemberger, J., Krimmel, A., Kurz, T., Krug von Nidda, H.-A., Ivanov, V. Y., Mukhin, A. A., Balbashov, A. M. & Loidl, A. Structural, magnetic, and electrical properties of single-crystalline $La_{1-x}Sr_xMnO_3$ ($0.4<x<0.85$). *Physical Review. B* **66.** ISSN: 0163-1829 (2002).

90. Ghosh, S., Shekhter, A., Jerzembeck, F., Kikugawa, N., Sokolov, D. A., Brando, M., Mackenzie, A. P., Hicks, C. W. & Ramshaw, B. J. Thermodynamic evidence for a two-component superconducting order parameter in Sr_2RuO_4. *Nature Physics* **17,** 199–204. ISSN: 1745-2473 (2021).

91. Bonmassar, N., Christiani, G., Heil, T., Logvenov, G., Suyolcu, Y. E. & van Aken, P. A. Superconductivity at Interfaces in Cuprate-Manganite Superlattices. *Advanced Science,* e2301495 (2023).

92. Liping, S., Lihua, H., Hui, Z., Qiang, L. & Pijolat, C. La substituted Sr_2MnO_4 as a possible cathode material in SOFC. *Journal of Power Sources* **179,** 96–100. ISSN: 03787753 (2008).

93. Senff, D., Reutler, P., Braden, M., Friedt, O., Bruns, D., Cousson, A., Bourée, F., Merz, M., Büchner, B. & Revcolevschi, A. Crystal and magnetic structure of $La_{1-x}Sr_{1+x}MnO_4$: Role of the orbital degree of freedom. *Physical Review B* **71.** ISSN: 1098-0121 (2005).

94. Larochelle, S., Mehta, A., Lu, L., Mang, P. K., Vajk, O. P., Kaneko, N., Lynn, J. W., Zhou, L. & Greven, M. Structural and magnetic properties of the single-layer manganese oxide $La_{1-x}Sr_{1+x}MnO_4$. *Physical Review B* **71.** ISSN: 1098-0121 (2005).

95. Choi, K.-Y., Lemmens, P., Heydhausen, D., Güntherodt, G., Baumann, C., Klingeler, R., Reutler, P. & Büchner, B. Anomalous orbital dynamics in $LaSrMnO_4$ observed by Raman spectroscopy. *Physical Review B* **77.** ISSN: 2469-9950 (2008).

96. Pei, S., Jorgensen, J. D., Hinks, D. G., Dabrowski, B., Lightfoot, P. & Richards, D. R. Pressure-induced structural changes in $La_{1.85}Sr_{0.15}CuO_4$. *Physica C: Superconductivity* **169,** 179–183. ISSN: 09214534 (1990).

97. De Luca, G. M., Ghiringhelli, G., Perroni, C. A., Cataudella, V., Chiarella, F., Cantoni, C., Lupini, A. R., Brookes, N. B., Huijben, M., Koster, G., Rijnders, G. & Salluzzo, M. Ubiquitous long-range antiferromagnetic coupling across the interface between superconducting and ferromagnetic oxides. *Nature communications* **5,** 5626 (2014).

98. Goswami, S., Mulazimoglu, E., Vandersypen, L. M. K. & Caviglia, A. D. Nanoscale electrostatic control of oxide interfaces. *Nano Letters* **15,** 2627–2632 (2015).

99. Chambers, S. A., Qiao, L., Droubay, T. C., Kaspar, T. C., Arey, B. W. & Sushko, P. V. Band alignment, built-in potential, and the absence of conductivity at the $LaCrO_3/SrTiO_3(001)$ heterojunction. *Physical Review Letters* **107,** 206802 (2011).

100. Park, D.-S., Rata, A. D., Maznichenko, I. V., Ostanin, S., Gan, Y. L., Agrestini, S., Rees, G. J., Walker, M., Li, J., Herrero-Martin, J., Singh, G., Luo, Z., Bhatnagar, A., Chen, Y. Z., Tileli, V., Muralt, P., Kalaboukhov, A., Mertig, I., Dörr, K., Ernst, A. & Pryds, N. The emergence of magnetic ordering at complex oxide interfaces tuned by defects. *Nature Communications* **11,** 3650 (2020).

101. Yoo, M., Yu, Y.-S., Ha, H., Lee, S., Choi, J.-S., Oh, S., Kang, E., Choi, H., An, H., Lee, K.-S., Park, J. Y., Celestre, R., Marcus, M. A., Nowrouzi, K., Taube, D., Shapiro, D. A., Jung, W., Kim, C. & Kim, H. Y. A tailored oxide interface creates dense Pt single-atom catalysts with high catalytic activity. *Energy & Environmental Science* **13,** 1231–1239. ISSN: 1754-5692 (2020).

102. Wang, H., Srot, V., Jiang, X., Yi, M., Wang, Y., Boschker, H., Merkle, R., Stark, R. W., Mannhart, J. & van Aken, P. A. Probing Charge Accumulation at $SrMnO_3/SrTiO_3$ Heterointerfaces via Advanced Electron Microscopy and Spectroscopy. *ACS Nano* **14,** 12697–12707 (2020).

103. Shah, A. B., Ramasse, Q. M., May, S. J., Kavich, J., Wen, J. G., Zhai, X., Eckstein, J. N., Freeland, J., Bhattacharya, A. & Zuo, J. M. Presence and spatial distribution of interfacial electronic states in $LaMnO_3$-$SrMnO_3$ superlattices. *Physical Review B* **82.** ISSN: 0163-1829 (2010).

104. Smallman, R. E. & Ngan, A. in *Modern Physical Metallurgy* 415–442 (Elsevier, 2014). ISBN: 9780080982045.

105. Dingreville, R., Hallil, A. & Berbenni, S. From coherent to incoherent mismatched interfaces: A generalized continuum formulation of surface stresses. *Journal of the Mechanics and Physics of Solids* **72,** 40–60. ISSN: 00225096 (2014).

106. Zhang, Z. & Lagally, M. G. Atomistic Processes in the Early Stages of Thin-Film Growth. *Science* **276,** 377–383 (1997).

107. Freund, L. B. & Suresh, S. *Thin Film Materials* ISBN: 9780521822817 (Cambridge University Press, 2010).

108. Gao, H. Some general properties of stress-driven surface evolution in a heteroepitaxial thin film structure. *Journal of the Mechanics and Physics of Solids* **42,** 741–772. ISSN: 00225096 (1994).

109. Guin, L., Jabbour, M. E. & Triantafyllidis, N. Revisiting step instabilities on crystal surfaces. Part I: The quasistatic approximation. *Journal of the Mechanics and Physics of Solids* **156,** 104574. ISSN: 00225096 (2021).

110. Yin, K., Yan, Z., Fang, N., Yu, W., Chu, Y., Shu, S. & Xu, M. The synergistic effect of surface vacancies and heterojunctions for efficient photocatalysis: A review. *Separation and Purification Technology* **325,** 124636. ISSN: 13835866 (2023).

111. Von Soosten, M., Christensen, D. V., Eom, C.-B., Jespersen, T. S., Chen, Y. & Pryds, N. On the emergence of conductivity at $SrTiO_3$-based oxide interfaces - an in-situ study. *Scientific Reports* **9,** 18005 (2019).

112. Lahmer, M. A. The effect of growth conditions and vacancies on the electronic, optical and photocatalytic properties of the ZnO (101-0) surface. *Materials Chemistry and Physics* **182,** 200–207. ISSN: 02540584 (2016).

113. Kaya, P., Gregori, G., Baiutti, F., Yordanov, P., Suyolcu, Y. E., Cristiani, G., Wrobel, F., Benckiser, E., Keimer, B., van Aken, P. A., Habermeier, H.-U., Logvenov, G. & Maier, J. High-Temperature Thermoelectricity in $LaNiO_3$-La_2CuO_4 Heterostructures. *ACS Applied Materials & Interfaces* **10,** 22786–22792 (2018).

114. Bonmassar, N., Christiani, G., Salzberger, U., Wang, Y., Logvenov, G., Suyolcu, Y. E. & van Aken, P. A. Design and Differentiation of Quantum States at Subnanometer Scale in La_2CuO_4-$Sr_2CuO_{4-\delta}$ Superlattices. *ACS Nano* (2023).

115. Schaaf, P. *Laser processing of materials: Fundamentals, applications and developments* ISBN: 978-3-642-13281-0 (Springer, 2010).

116. Comes, R., Gu, M., Khokhlov, M., Liu, H., Lu, J. & Wolf, S. A. Electron molecular beam epitaxy: Layer-by-layer growth of complex oxides via pulsed electron-beam deposition. *Journal of Applied Physics* **113.** ISSN: 0021-8979 (2013).

117. Goldman, A. *Modern ferrite technology* 2nd ed. ISBN: 9780387294131 (Springer, New York NY, 2005).

118. Culbertson, C. M., Flak, A. T., Yatskin, M., Cheong, P. H.-Y., Cann, D. P. & Dolgos, M. R. Neutron Total Scattering Studies of Group II Titanates ($ATiO_3$, A^{2+} = Mg, Ca, Sr, Ba). *Scientific Reports* **10,** 3729 (2020).

119. Hong, W., Lee, H. N., Yoon, M., Christen, H. M., Lowndes, D. H., Suo, Z. & Zhang, Z. Persistent step-flow growth of strained films on vicinal substrates. *Physical Review Letters* **95,** 095501 (2005).

120. Ruska, E. *The early development of electron lenses and electron microscopy* ISBN: 978-3-7776-0364-3 (Hirzel, Stuttgart, 1980).

121. Chen, Z., Jiang, Y., Shao, Y.-T., Holtz, M. E., Odstrčil, M., Guizar-Sicairos, M., Hanke, I., Ganschow, S., Schlom, D. G. & Muller, D. A. Electron ptychography achieves atomic-resolution limits set by lattice vibrations. *Science* **372,** 826–831 (2021).

122. Von Ardenne, M. Die Grenzen für das Auflösungsvermögen des Elektronenmikroskops. *Zeitschrift für Physik* **108,** 338–352. ISSN: 0044-3328 (1938).

123. Hawkes, P. W. Aberration correction past and present. *Philosophical Transactions. Series A, Mathematical, physical, and engineering sciences* **367,** 3637–3664. ISSN: 1364-503X (2009).

124. Haider, M., Müller, H., Uhlemann, S., Zach, J., Loebau, U. & Hoeschen, R. Prerequisites for a Cc/Cs-corrected ultrahigh-resolution TEM. *Ultramicroscopy* **108,** 167–178. ISSN: 0304-3991 (2008).

125. Haider, M., Uhlemann, S., Schwan, E., Rose, H., Kabius, B. & Urban, K. Electron microscopy image enhanced. *Nature* **392,** 768–769 (1998).

126. Harald Rose. Outline of a spherically corrected semiaplanatic medium-voltage transmission electron microscope. *Optik,* 19–24 (1990).

127. Haider, M., Rose, H., Uhlemann, S., Schwan, E., Kabius, B. & Urban, K. A spherical-aberration-corrected 200kV transmission electron microscope. *Ultramicroscopy* **75,** 53–60. ISSN: 0304-3991 (1998).

128. Krivanek, O. L., Dellby, N. & Lupini, A. R. Towards sub-Å electron beams. *Ultramicroscopy* **78,** 1–11. ISSN: 0304-3991 (1999).

129. Haider, M., Hartel, P., Müller, H., Uhlemann, S. & Zach, J. Current and future aberration correctors for the improvement of resolution in electron microscopy. *Philosophical Transactions. Series A, Mathematical, physical, and engineering sciences* **367,** 3665–3682. ISSN: 1364-503X (2009).

130. Urban, K. W. Studying atomic structures by aberration-corrected transmission electron microscopy. *Science* **321,** 506–510 (2008).

131. Brydson, R. *Aberration-corrected analytical transmission electron microscopy* ISBN: 978-0470-518519 (RMS-Wiley, Chichester, West Sussex, U.K., 2011).

132. PENNYCOOK, S. J. & McMullan, D. A new high-angle annular detector for stem. *Ultramicroscopy* **11,** 315–319. ISSN: 0304-3991 (1983).

133. PENNYCOOK, S. J. & Boatner, L. A. Chemically sensitive structure-imaging with a scanning transmission electron microscope. *Nature* **336,** 565–567 (1988).

134. Wang, Z. W., Li, Z. Y., Park, S. J., Abdela, A., Tang, D. & Palmer, R. E. Quantitative Z-contrast imaging in the scanning transmission electron microscope with size-selected clusters. *Physical Review B* **84.** ISSN: 2469-9950 (2011).

135. Findlay, S. D., Shibata, N., Sawada, H., Okunishi, E., Kondo, Y. & Ikuhara, Y. Dynamics of annular bright field imaging in scanning transmission electron microscopy. *Ultramicroscopy* **110,** 903–923. ISSN: 0304-3991 (2010).

136. Cowley, J. M. Surface energies and surface structure of small crystals studied by use of a stem instrument. *Surface Science* **114,** 587–606. ISSN: 00396028 (1982).

137. Hillier, J. & Baker, R. F. Microanalysis by Means of Electrons. *Journal of Applied Physics* **15,** 663–675. ISSN: 0021-8979 (1944).

138. Browning, N. D. & PENNYCOOK, S. J. Atomic-resolution electron energy-loss spectroscopy in the scanning transmission electron microscope. *Journal of Microscopy* **180,** 230–237. ISSN: 0022-2720 (1995).

139. Klie, R. F., Arslan, I. & Browning, N. D. Atomic resolution electron energy-loss spectroscopy. *Journal of Electron Spectroscopy and Related Phenomena* **143,** 105–115. ISSN: 03682048 (2005).

140. Muller, D. A., Tzou, Y., Raj, R. & Silcox, J. Mapping sp^2 and sp^3 states of carbon at sub-nanometre spatial resolution. *Nature* **366,** 725–727 (1993).

141. Batson, P. E. & Chisholm, M. F. Anisotropy in the near-edge absorption fine structure of YBa2Cu. *Physical review. B, Condensed matter* **37,** 635–637. ISSN: 0163-1829 (1988).

142. Silcox, J. Core-loss EELS. *Current Opinion in Solid State and Materials Science* **3,** 336–342. ISSN: 13590286 (1998).

143. van Aken, P. A. & Liebscher, B. Quantification of ferrous/ferric ratios in minerals: new evaluation schemes of Fe $L_{2,3}$ electron energy-loss near-edge spectra. *Physics and Chemistry of Minerals* **29,** 188–200. ISSN: 0342-1791 (2002).

144. Garvie, L. & Buseck, P. R. Determination of Ce^{4+}/Ce^{3+} in electron-beam-damaged CeO_2 by electron energy-loss spectroscopy. *Journal of Physics and Chemistry of Solids* **60,** 1943–1947. ISSN: 00223697 (1999).

145. Binasch, G., Grünberg, P., Saurenbach, F. & Zinn, W. Enhanced magnetoresistance in layered magnetic structures with antiferromagnetic interlayer exchange. *Physical Review. B* **39,** 4828–4830. ISSN: 0163-1829 (1989).

146. Baibich, M. N., Broto, J. M., Fert, A., van Nguyen, D. F., Petroff, F., Etienne, P., Creuzet, G., Friederich, A. & Chazelas, J. Giant magnetoresistance of (001)Fe/(001)Cr magnetic superlattices. *Physical Review Letters* **61,** 2472–2475. ISSN: 0031-9007 (1988).

147. Müller, K. A. & Bednorz, J. G. The discovery of a class of high-temperature superconductors. *Science* **237,** 1133–1139 (1987).

148. Abbamonte, P., Venema, L., Rusydi, A., Sawatzky, G. A., Logvenov, G. & Bozovic, I. A structural probe of the doped holes in cuprate superconductors. *Science* **297,** 581–584 (2002).

149. Attfield, J. P., Kharlanov, A. L. & McAllister, J. A. Cation effects in doped La_2CuO_4 superconductors. *Nature* **394,** 157–159 (1998).

150. Choi, E.-M., Di Bernardo, A., Zhu, B., Lu, P., Alpern, H., Zhang, K. H. L., Shapira, T., Feighan, J., Sun, X., Robinson, J., Paltiel, Y., Millo, O., Wang, H., Jia, Q. & MacManus-Driscoll, J. L. 3D strain-induced superconductivity in $La_2CuO_{4+\delta}$ using a simple vertically aligned nanocomposite approach. *Science Advances* **5,** eaav5532 (2019).

151. Choi, E.-M., Zhu, B., Lu, P., Feighan, J., Sun, X., Wang, H. & MacManus-Driscoll, J. L. Magnetic signatures of 120 K superconductivity at interfaces in La_2CuO_{4+d}. *Nanoscale* **12,** 3157–3165 (2020).

152. Tokura, Y., Takagi, H. & Uchida, S. A superconducting copper oxide compound with electrons as the charge carriers. *Nature* **337,** 345–347 (1989).

153. Baiutti, F., Christiani, G. & Logvenov, G. Towards precise defect control in layered oxide structures by using oxide molecular beam epitaxy. *Beilstein Journal of Nanotechnology* **5,** 596–602. ISSN: 2190-4286 (2014).

154. Baiutti, F., Logvenov, G., Gregori, G., Cristiani, G., Wang, Y., Sigle, W., van Aken, P. A. & Maier, J. High-temperature superconductivity in space-charge regions of lanthanum cuprate induced by two-dimensional doping. *Nature Communications* **6,** 8586 (2015).

155. Suyolcu, Y. E., Wang, Y., Baiutti, F., Al-Temimy, A., Gregori, G., Cristiani, G., Sigle, W., Maier, J., van Aken, P. A. & Logvenov, G. Dopant size effects on novel functionalities: High-temperature interfacial superconductivity. *Scientific Reports* **7,** 453 (2017).

156. Ruiz, A., Gunn, B., Lu, Y., Sasmal, K., Moir, C. M., Basak, R., Huang, H., Lee, J.-S., Rodolakis, F., Boyle, T. J., Walker, M., He, Y., Blanco-Canosa, S., Da Silva Neto, E. H., Maple, M. B. & Frano, A. Stabilization of three-dimensional charge order through interplanar orbital hybridization in $PrBa_2Cu_3O_{7-x}$. *Nature Communications* **13,** 6197 (2022).

157. Nag, A., Zhu, M., Bejas, M., Li, J., Robarts, H. C., Yamase, H., Petsch, A. N., Song, D., Eisaki, H., Walters, A. C., García-Fernández, M., Greco, A., Hayden, S. M. & Zhou, K.-J. Detection of Acoustic Plasmons in Hole-Doped Lanthanum and Bismuth Cuprate Superconductors Using Resonant Inelastic X-Ray Scattering. *Physical Review Letters* **125,** 257002. ISSN: 0031-9007 (2020).

158. Meyers, D., Mukherjee, S., Cheng, J.-G., Middey, S., Zhou, J.-S., Goodenough, J. B., Gray, B. A., Freeland, J. W., Saha-Dasgupta, T. & Chakhalian, J. Zhang-Rice physics and anomalous copper states in A-site ordered perovskites. *Scientific Reports* **3,** 1834 (2013).

159. Bugnet, M., Löffler, S., Hawthorn, D., Dabkowska, H. A., Luke, G. M., Schattschneider, P., Sawatzky, G. A., Radtke, G. & Botton, G. A. Real-space localization and quantification of hole distribution in chain-ladder $Sr_3Ca_{11}Cu_2 4O_{41}$ superconductor. *Science Advances* **2,** e1501652 (2016).

160. Gauquelin, N., Hawthorn, D. G., Sawatzky, G. A., Liang, R. X., Bonn, D. A., Hardy, W. N. & Botton, G. A. Atomic scale real-space mapping of holes in $YBa_2Cu_3O_{(6+d)}$. *Nature Communications* **5,** 4275 (2014).

161. Smadici, S., Lee, J. C. T., Rusydi, A., Logvenov, G., Bozovic, I. & Abbamonte, P. Distinct oxygen hole doping in different layers of Sr_2CuO_{4-d}/La_2CuO_4 superlattices. *Physical Review B* **85.** ISSN: 1098-0121 (2012).

162. Weber, C., Haule, K. & Kotliar, G. Apical oxygens and correlation strength in electron- and hole-doped copper oxides. *Physical Review B* **82.** ISSN: 1098-0121 (2010).

163. Chen, Tjeng, Kwo, Kao, Rudolf, Sette & Fleming. Out-of-plane orbital characters of intrinsic and doped holes in $La_{2-x}Sr_xCuO_4$. *Physical Review Letters* **68,** 2543–2546. ISSN: 0031-9007 (1992).

164. Conradson, S. D., Geballe, T. H., Jin, C., Cao, L., Baldinozzi, G., Jiang, J. M., Latimer, M. J. & Mueller, O. Local structure of $Sr_2CuO_{3.3}$, a 95 K cuprate superconductor without CuO_2 planes. *Proceedings of the National Academy of Sciences of the United States of America* **117,** 4565–4570 (2020).

165. Zeng, L., Tran, D. T., Tai, C.-W., Svensson, G. & Olsson, E. Atomic structure and oxygen deficiency of the ultrathin aluminium oxide barrier in Al/AlO_x /Al Josephson junctions. *Scientific Reports* **6,** 29679 (2016).

166. Bosman, M., Watanabe, M., Alexander, D. T. L. & Keast, V. J. Mapping chemical and bonding information using multivariate analysis of electron energy-loss spectrum images. *Ultramicroscopy* **106,** 1024–1032 (2006).

167. Paolo Longo. *The use of MLLS fitting approach to resolve overlapping edges in the EELS spectrum at the atomic level* (ed Gatan, Inc.) 2017.

168. Pennycook & Jesson. High-resolution incoherent imaging of crystals. *Physical Review Letters* **64,** 938–941. ISSN: 0031-9007 (1990).

169. Wu, Y.-M., Suyolcu, Y. E., Kim, G., Christiani, G., Wang, Y., Keimer, B., Logvenov, G. & van Aken, P. A. Atomic-Scale Tuning of the Charge Distribution by Strain Engineering in Oxide Heterostructures. *ACS Nano* **15,** 16228–16235 (2021).

170. Smadici, S., Lee, J. C. T., Wang, S., Abbamonte, P., Logvenov, G., Gozar, A., Cavellin, C. D. & Bozovic, I. Superconducting transition at 38 K in insulating-overdoped La_2CuO_4-$La_{1.64}Sr_{0.36}CuO_4$ superlattices: evidence for interface electronic redistribution from resonant soft X-ray scattering. *Physical Review Letters* **102,** 107004. ISSN: 0031-9007 (2009).

171. Wang, Z., Nayak, P. K., Caraveo-Frescas, J. A. & Alshareef, H. N. Recent Developments in p-Type Oxide Semiconductor Materials and Devices. *Advanced Materials* **28,** 3831–3892 (2016).

172. Kleiner & Müller. Intrinsic Josephson effects in high-Tc superconductors. *Physical Review. B* **49,** 1327–1341. ISSN: 0163-1829 (1994).

173. Suyolcu, Y. E., Sun, J., Goodge, B. H., Park, J., Schubert, J., Kourkoutis, L. F. & Schlom, D. G. a-axis $YBa_2Cu_3O_{7-x}$/$PrBa_2Cu_3O_{7-x}$/$YBa_2Cu_3O_{7-x}$ trilayers with subnanometer rms roughness. *APL Materials* **9,** 021117 (2021).

174. Hjelmeland, T. B., Bazioti, C., Gunnaes, A. E., Volkov, Y. & Mikheenko, P. Effect of colossal magnetoresistance material $La_{0.67}Ca_{0.33}MnO_3$ on superconducting properties of $YBa_2Cu_3O_{7-x}$ thin films. *Journal of Magnetism and Magnetic Materials* **487,** 165335. ISSN: 03048853 (2019).

175. Prajapat, C. L., Singh, S., Bhattacharya, D., Ravikumar, G., Basu, S., Mattauch, S., Zheng, J.-G., Aoki, T. & Paul, A. Proximity effects across oxide-interfaces of superconductor-insulator-ferromagnet hybrid heterostructure. *Scientific Reports* **8,** 3732 (2018).

176. Gingrich, E. C., Niedzielski, B. M., Glick, J. A., Wang, Y., Miller, D. L., Loloee, R., Pratt Jr, W. P. & Birge, N. O. Controllable 0-π Josephson junctions containing a ferromagnetic spin valve. *Nature Physics* **12,** 564–567. ISSN: 1745-2473 (2016).

177. Tripathi, V., Chen, H., Khezri, M., Yip, K.-W., Levenson-Falk, E. M. & Lidar, D. A. Suppression of Crosstalk in Superconducting Qubits Using Dynamical Decoupling. *Physical Review Applied* **18** (2022).

178. Groszkowski, P., Di Paolo, A., Grimsmo, A. L., Blais, A., Schuster, D. I., Houck, A. A. & Koch, J. Coherence properties of the 0-π qubit. *New Journal of Physics* **20,** 043053 (2018).

179. Ilichev, E., Grajcar, M., Hlubina, R., IJsselsteijn, R. P., Hoenig, H. E., Meyer, H. G., Golubov, A., Amin, M. H., Zagoskin, A. M., Omelyanchouk, A. N. & Kupriyanov, M. Y. Degenerate ground state in a mesoscopic $YBa_2Cu_3 O_{7-x}$ grain boundary Josephson junction. *Physical Review Letters* **86,** 5369–5372. ISSN: 0031-9007 (2001).

180. Dolcini, F., Houzet, M. & Meyer, J. S. Topological Josephson ϕ_0 junctions. *Physical Review B* **92.** ISSN: 1098-0121 (2015).

181. Nakagawa, N., Hwang, H. Y. & Muller, D. A. Why some interfaces cannot be sharp. *Nature Materials* **5,** 204–209. ISSN: 1476-1122 (2006).

182. Maier, J. & Pfundtner, G. Defect chemistry of the high-Tc superconductors. *Advanced Materials* **3,** 292–297. ISSN: 0935-9648 (1991).

183. Zhou, H., Yacoby, Y., Butko, V. Y., Logvenov, G., Bozovic, I. & Pindak, R. Anomalous expansion of the copper-apical-oxygen distance in superconducting cuprate bilayers. *Proceedings of the National Academy of Sciences of the United States of America* **107,** 8103–8107 (2010).

184. Huang, Z., Ariando, Renshaw Wang, X., Rusydi, A., Chen, J., Yang, H. & Venkatesan, T. Interface Engineering and Emergent Phenomena in Oxide Heterostructures. *Advanced Materials* **30,** e1802439. ISSN: 0935-9648 (2018).

185. Frano, A., Blanco-Canosa, S., Schierle, E., Lu, Y., Wu, M., Bluschke, M., Minola, M., Christiani, G., Habermeier, H. U., Logvenov, G., Wang, Y., van Aken, P. A., Benckiser, E., Weschke, E., Le Tacon, M. & Keimer, B. Long-range charge-density-wave proximity effect at cuprate/manganate interfaces. *Nature Materials* **15,** 831–834. ISSN: 1476-1122 (2016).

186. Jang, H.-B., Lim, J. S. & Yang, C.-H. Film-thickness-driven superconductor to insulator transition in cuprate superconductors. *Scientific Reports* **10,** 3236 (2020).

187. Büchner, B., Freimuth, A., Breuer, M., Lang, A., Micklitz, H. & Kampf, A. P. Buckling of the CuO_2 planes and the electronic properties of doped La_2CuO_4 superconductors. *Physica C: Superconductivity and its Applications* **235-240,** 1227–1228. ISSN: 09214534 (1994).

188. Naito, M. & Sato, H. Stoichiometry control of atomic beam fluxes by precipitated impurity phase detection in growth of $(Pr,Ce)_2CuO_4$ and $(La,Sr)_2CuO_4$ films. *Applied Physics Letters* **67,** 2557–2559. ISSN: 0003-6951 (1995).

189. Shannon, R. D., Oswald, R. A., Parise, J. B., Chai, B., Byszewski, P., Pajaczkowska, A. & Sobolewski, R. Dielectric constants and crystal structures of $CaYAlO_4$, $CaNdAlO_4$, and $SrLaAlO_4$, and deviations from the oxide additivity rule. *Journal of Solid State Chemistry* **98,** 90–98. ISSN: 00224596 (1992).

190. Tezuka, K., Inamura, M., Hinatsu, Y., Shimojo, Y. & Morii, Y. Crystal Structures and Magnetic Properties of $Ca_{2-x}Sr_xMnO_4$. *Journal of Solid State Chemistry* **145,** 705–710. ISSN: 00224596 (1999).

191. Rák, Z., Maria, J.-P. & Brenner, D. W. Evidence for Jahn-Teller compression in the (Mg, Co, Ni, Cu, Zn)O entropy-stabilized oxide: A DFT study. *Materials Letters* **217,** 300–303. ISSN: 0167577X (2018).

192. Ruf, J. P., Paik, H., Schreiber, N. J., Nair, H. P., Miao, L., Kawasaki, J. K., Nelson, J. N., Faeth, B. D., Lee, Y., Goodge, B. H., Pamuk, B., Fennie, C. J., Kourkoutis, L. F., Schlom, D. G. & Shen, K. M. Strain-stabilized superconductivity. *Nature Communications* **12,** 59 (2021).

193. Zhang, J., Ji, C., Shangguan, Y., Guo, B., Wang, J., Huang, F., Lu, X. & Zhu, J. Strain-driven magnetic phase transitions from an antiferromagnetic to a ferromagnetic state in perovskite $RMnO_3$ films. *Physical Review B* **98.** ISSN: 1098-0121 (2018).

194. Tan, H., Verbeeck, J., Abakumov, A. & van Tendeloo, G. Oxidation state and chemical shift investigation in transition metal oxides by EELS. *Ultramicroscopy* **116,** 24–33. ISSN: 03043991 (2012).

195. Bonmassar, N., Christiani, G., Brucker, M., Logvenov, G., Suyolcu, Y. E. & van Aken, P. A. Bi–Directional Growth of Thin Films: Unlocking Anisotropic Ferromagnetism and Superconductivity. *Advanced Functional Materials.* ISSN: 1616-301X (2024).

196. Paterson, A. F. & Anthopoulos, T. D. Enabling thin-film transistor technologies and the device metrics that matter. *Nature Communications* **9,** 5264 (2018).

197. Goetzberger, A., Hebling, C. & Schock, H.-W. Photovoltaic materials, history, status and outlook. *Materials Science and Engineering: R: Reports* **40,** 1–46. ISSN: 0927796X (2003).

198. Fu, X., Mehta, Y., Chen, Y.-A., Lei, L., Zhu, L., Barange, N., Dong, Q., Yin, S., Mendes, J., He, S., Gogusetti, R., Chang, C.-H. & So, F. Directional Polarized Light Emission from Thin-Film Light-Emitting Diodes. *Advanced Materials* **33,** e2006801 (2021).

199. Wang, Q., Shang, D. S., Wu, Z. H., Chen, L. D. & Li, X. M. "Positive" and "negative" electric-pulse-induced reversible resistance switching effect in $Pr_{0.7}Ca_{0.3}MnO_3$ films. *Applied Physics A* **86,** 357–360. ISSN: 0947-8396 (2007).

200. Novoselov, K. S., Geim, A. K., Morozov, S. V., Jiang, D., Zhang, Y., Dubonos, S. V., Grigorieva, I. V. & Firsov, A. A. Electric field effect in atomically thin carbon films. *Science* **306,** 666–669 (2004).

201. Fert, A. Nobel Lecture: Origin, development, and future of spintronics. *Reviews of Modern Physics* **80,** 1517–1530. ISSN: 0034-6861 (2008).

202. Miller, D. L., Chen, R. T., Elliott, K. & Kowalczyk, S. P. Molecular-beam-epitaxy GaAs regrowth with clean interfaces by arsenic passivation. *Journal of Applied Physics* **57,** 1922–1927. ISSN: 0021-8979 (1985).

203. Oka, T. & Nagaosa, N. Interfaces of correlated electron systems: proposed mechanism for colossal electroresistance. *Physical Review Letters* **95,** 266403. ISSN: 0031-9007 (2005).

204. Betts, R. A. & Pitt, C. W. Growth of thin-film lithium niobate by molecular beam epitaxy. *Electronics Letters* **21,** 960. ISSN: 00135194 (1985).

205. Fukui, T. & Saito, H. Step-flow growth and fractional-layer superlattices on GaAs vicinal surfaces by MOCVD. *Journal of Crystal Growth* **115,** 61–64. ISSN: 00220248 (1991).

206. Arpapay, B., Suyolcu, Y. E., Çorapçıoğlu, G., van Aken, P. A., Gülgün, M. A. & Serincan, U. A comparative study on GaSb epilayers grown on nominal and vicinal Si(100) substrates by molecular beam epitaxy. *Semiconductor Science and Technology* **36,** 025011. ISSN: 0268-1242 (2020).

207. Budai, J. D., Chisholm, M. F., Feenstra, R., Lowndes, D. H., Norton, D. P., Boatner, L. A. & Christen, D. K. Preferred alignment of twin boundaries in $YBa_2Cu_3O_{7-x}$ thin films and $YBa_2Cu_3O_{7-x}/PrBa_2Cu_3O_{7-x}$ superlattices on $SrTiO_3$. *Applied Physics Letters* **58,** 2174–2176. ISSN: 0003-6951 (1991).

208. Hensling, F. V. E., Du, H., Raab, N., Jia, C.-L., Mayer, J. & Dittmann, R. Engineering antiphase boundaries in epitaxial $SrTiO_3$ to achieve forming free memristive devices. *APL Materials* **7** (2019).

209. Wang, Z., Guo, H., Shao, S., Saghayezhian, M., Li, J., Fittipaldi, R., Vecchione, A., Siwakoti, P., Zhu, Y., Zhang, J. & Plummer, E. W. Designing antiphase boundaries by atomic control of heterointerfaces. *Proceedings of the National Academy of Sciences of the United States of America* **115,** 9485–9490 (2018).

210. Yordanov, P., Sigle, W., Kaya, P., Gruner, M. E., Pentcheva, R., Keimer, B. & Habermeier, H.-U. Large thermopower anisotropy in $PdCoO_2$ thin films. *Physical Review Materials* **3** (2019).

211. Pawlak, J., Żywczak, A., Kanak, J. & Przybylski, M. Surface-Step-Induced Magnetic Anisotropy in Epitaxial LSMO Deposited on Engineered STO Surfaces. *Materials* **13.** ISSN: 1996-1944 (2020).

212. Perna, P., Maccariello, D., Ajejas, F., Guerrero, R., Méchin, L., Flament, S., Santamaria, J., Miranda, R. & Camarero, J. Engineering Large Anisotropic Magnetoresistance in $La_{0.7}Sr_{0.3}MnO_3$ Films at Room Temperature. *Advanced Functional Materials* **27,** 1700664. ISSN: 1616-301X (2017).

213. Braun, W., Jäger, M., Laskin, G., Ngabonziza, P., Voesch, W., Wittlich, P. & Mannhart, J. In situ thermal preparation of oxide surfaces. *APL Materials* **8,** 071112 (2020).

214. Petroff, P. M., Gossard, A. C. & Wiegmann, W. Structure of AlAs-GaAs interfaces grown on (100) vicinal surfaces by molecular beam epitaxy. *Applied Physics Letters* **45,** 620–622. ISSN: 0003-6951 (1984).

215. Culbertson, C. M., Flak, A. T., Yatskin, M., Cheong, P. H.-Y., Cann, D. P. & Dolgos, M. R. Neutron Total Scattering Studies of Group II Titanates ($ATiO_3$, A^{2+} = Mg, Ca, Sr, Ba). *Scientific Reports* **10,** 3729 (2020).

216. Keunecke, M., Lyzwa, F., Schwarzbach, D., Roddatis, V., Gauquelin, N., Müller–Caspary, K., Verbeeck, J., Callori, S. J., Klose, F., Jungbauer, M. & Moshnyaga, V. High-Tc Interfacial Ferromagnetism in $SrMnO_3/LaMnO_3$ Superlattices. *Advanced Functional Materials* **30,** 1808270. ISSN: 1616-301X (2020).

217. Hona, R. K. & Ramezanipour, F. Effect of the Oxygen Vacancies and Structural Order on the Oxygen Evolution Activity: A Case Study of $SrMnO_{3-\delta}$ Featuring Four Different Structure Types. *Inorganic Chemistry* **59,** 4685–4692 (2020).

218. Cowley, R. A. Lattice Dynamics and Phase Transitions of Strontium Titanate. *Physical Review* **134,** A981–A997. ISSN: 0031-899X (1964).

219. Hong, S. S., Gu, M., Verma, M., Harbola, V., Wang, B. Y., Di Lu, Vailionis, A., Hikita, Y., Pentcheva, R., Rondinelli, J. M. & Hwang, H. Y. Extreme tensile strain states in $La_{0.7}Ca_{0.3}MnO_3$ membranes. *Science* **368,** 71–76 (2020).

220. Courtois, H., Meschke, M., Peltonen, J. T. & Pekola, J. P. Origin of hysteresis in a proximity Josephson junction. *Physical Review Letters* **101,** 067002. ISSN: 0031-9007 (2008).

221. Bonmassar, N., Christiani, G., Logvenov, G., Suyolcu, Y. E. & van Aken, P. A. Offcut Substrate-Induced Defect Trapping at Step Edges. *Nano Letters* **24,** 5556–5561 (2024).

222. Mao, Y., Li, Y., Xiong, Y. & Xiao, W. Point defect effects on the thermal conductivity of β-SiC by molecular dynamics simulations. *Computational Materials Science* **152,** 300–307. ISSN: 09270256 (2018).

223. Sabzevar, M., Solaimani, M., Ehsani, M. H. & Haji Taghi Tehrani, D. The effect of vacancy-defects on the magnetic properties of Ising fullerene-like nano-structures: A Monte Carlo study. *Journal of Magnetism and Magnetic Materials* **502,** 166573. ISSN: 03048853 (2020).

224. Mahajan, S. Defects in semiconductors and their effects on devices. *Acta Materialia* **48,** 137–149. ISSN: 13596454 (2000).

225. Kamšek, A. R., Meden, A., Arčon, I., Jovanovič, P., Šala, M., Ruiz-Zepeda, F., Dražić, G., Gaberšček, M., Bele, M. & Hodnik, N. Periodic anti-phase boundaries and crystal superstructures in $PtCu_3$ nanoparticles as fuel cell electrocatalysts. *Materials Today Nano* **23,** 100377. ISSN: 25888420 (2023).

226. Han, H., Xing, Y., Park, B., Bazhanov, D. I., Jin, Y., Irvine, J. T. S., Lee, J. & Oh, S. H. Anti-phase boundary accelerated exsolution of nanoparticles in non-stoichiometric perovskite thin films. *Nature Communications* **13,** 6682 (2022).

227. Xu, Z., Hou, D., Kautz, D. J., Liu, W., Xu, R., Xiao, X. & Lin, F. Charging Reactions Promoted by Geometrically Necessary Dislocations in Battery Materials Revealed by In Situ Single-Particle Synchrotron Measurements. *Advanced Materials* **32,** e2003417 (2020).

228. Jeong, J. S., Topsakal, M., Xu, P., Jalan, B., Wentzcovitch, R. M. & Mkhoyan, K. A. A New Line Defect in $NdTiO_3$ Perovskite. *Nano Letters* **16,** 6816–6822 (2016).

229. Kumar, V., Som, S., Sharma, V. & Swart, H. C. *Metal oxide defects: Fundamentals, design, development and applications / edited by Vijay Kumar, Sudipta Som, Vishal Sharma, Hendrik C. Swart* ISBN: 978-0-323-85588-4 (Elsevier, Amsterdam, 2022).

230. Yancey, J. A., Richards, H. L. & Einstein, T. L. Terrace width distributions for vicinal surfaces with steps of alternating stiffness. *Surface Science* **598,** 78–87. ISSN: 00396028 (2005).

231. Lei, Q., Golalikhani, M., Davidson, B. A., Liu, G., Schlom, D. G., Qiao, Q., Zhu, Y., Chandrasena, R. U., Yang, W., Gray, A. X., Arenholz, E., Farrar, A. K., Tenne, D. A., Hu, M., Guo, J., Singh, R. K. & Xi, X. Constructing oxide interfaces and heterostructures by atomic layer-by-layer laser molecular beam epitaxy. *npj Quantum Materials* **2** (2017).

232. Salvato, M., Salluzzo, M., Di Luccio, T., Attanasio, C., Prischepa, S. L. & Maritato, L. Properties of $Bi_{2+x}Sr_{2-x}CuO_{6+\delta}$ thin films obtained by MBE. *Thin Solid Films* **353,** 227–232. ISSN: 00406090 (1999).

233. Baldini, M., Muramatsu, T., Sherafati, M., Mao, H.-k., Malavasi, L., Postorino, P., Satpathy, S. & Struzhkin, V. V. Origin of colossal magnetoresistance in $LaMnO_3$ manganite. *Proceedings of the National Academy of Sciences of the United States of America* **112,** 10869–10872 (2015).

234. Rao, C. N. R., Sundaresan, A. & Saha, R. Multiferroic and Magnetoelectric Oxides: The Emerging Scenario. *The journal of Physical Chemistry Letters* **3,** 2237–2246. ISSN: 1948-7185 (2012).

235. Heisig, T., Kler, J., Du, H., Baeumer, C., Hensling, F., Glöß, M., Moors, M., Locatelli, A., Menteş, T. O., Genuzio, F., Mayer, J., de Souza, R. A. & Dittmann, R. Antiphase Boundaries Constitute Fast Cation Diffusion Paths in $SrTiO_3$ Memristive Devices. *Advanced Functional Materials* **30,** 2004118. ISSN: 1616-301X (2020).

236. Radaelli, P. G., Iannone, G., Marezio, M., Hwang, H. Y., Cheong, S.-W., Jorgensen, J. D. & Argyriou, D. N. Structural effects on the magnetic and transport properties of perovskite $A_{1-x}A\prime_{x}MnO_3$ (x=0.25, 0.30). *Physical Review B* **56,** 8265–8276. ISSN: 1098-0121 (1997).

237. François, M., Yvon, K., Fischer, P. & Decroux, M. Structural phase transition at 150 K in the high-temperature superconductor $La_{1.85}Sr_{0.15}CuO_4$. *Solid State Communications* **63,** 35–40. ISSN: 00381098 (1987).

238. Erdman, N., Poeppelmeier, K. R., Asta, M., Warschkow, O., Ellis, D. E. & Marks, L. D. The structure and chemistry of the TiO_2-rich surface of $SrTiO_3$ (001). *Nature* **419,** 55–58 (2002).

239. Braun, W. *Applied RHEED: Reflection high-energy electron diffraction during crystal growth* ISBN: 3-540-65199-3 (Springer, Berlin and New York, 1999).

240. Koster, G., Birkhölzer, Y., Huijben, M., Rijnders, G., Spreitzer, M., Kornblum, L. & Smink, S. in *Epitaxial Growth of Complex Metal Oxides* 3–36 (Elsevier, 2022). ISBN: 9780081029459.

241. Aschauer, U., Pfenninger, R., Selbach, S. M., Grande, T. & Spaldin, N. A. Strain-controlled oxygen vacancy formation and ordering in $CaMnO_3$. *Physical Review B* **88.** ISSN: 1098-0121 (2013).

242. Naito, M., Sato, H., Tsukada, A. & Yamamoto, H. Epitaxial effects in thin films of high-Tc cuprates with the K_2NiF_4 structure. *Physica C: Superconductivity and its Applications* **546,** 84–114. ISSN: 09214534 (2018).

243. Gilbert, B., Frazer, B. H., Belz, A., Conrad, P. G., Nealson, K. H., Haskel, D., Lang, J. C., Srajer, G. & de Stasio, G. Multiple Scattering Calculations of Bonding and X-ray Absorption Spectroscopy of Manganese Oxides. *The Journal of Physical Chemistry A* **107,** 2839–2847. ISSN: 1089-5639 (2003).

244. Heo, S., Oh, C., Son, J. & Jang, H. M. Influence of tensile-strain-induced oxygen deficiency on metal-insulator transitions in $NdNiO_{3-\delta}$ epitaxial thin films. *Scientific Reports* **7,** 4681 (2017).

245. Xu, R., Huang, J., Barnard, E. S., Hong, S. S., Singh, P., Wong, E. K., Jansen, T., Harbola, V., Xiao, J., Wang, B. Y., Crossley, S., Di Lu, Liu, S. & Hwang, H. Y. Strain-induced room-temperature ferroelectricity in $SrTiO_3$ membranes. *Nature communications* **11,** 3141 (2020).